A Theory for Polar Cyclones on Giant Planets

by

Morgan E O'Neill

B.S. Physics, University of New Hampshire (2009)

Submitted to the Department of Earth, Atmospheric and Planetary Sciences
in partial fulfillment of the requirements for the degree of

Doctor of Philosophy in Atmospheric Sciences

at the

MASSACHUSETTS INSTITUTE OF TECHNOLOGY

February 2015

Author .....
Department of Earth, Atmospheric and Planetary Sciences
January 30, 2015

Certified by .....
Kerry A. Emanuel
Cecil & Ida Green Professor of Atmospheric Science
Thesis Supervisor

Accepted by .....
Robert van der Hilst
Head of Dept. of Earth, Atmospheric and Planetary Sciences

A Theory for Polar Cyclones on Giant Planets

by

Morgan E O'Neill

Submitted to the Department of Earth, Atmospheric and Planetary Sciences
on January 30, 2015, in partial fulfillment of the
requirements for the degree of
Doctor of Philosophy in Atmospheric Sciences

Abstract

The giant planets each have distinct polar behavior. Saturn has the most striking features, with a deep, hot and rapid cyclone situated directly over each pole, and a rapid jet marking the cyclone boundary at 3° from the pole. Extant theories for the zonal jets preclude the possibility of a jet at such high latitudes. This thesis proposes and tests a moist convective hypothesis for polar cyclone formation. Using purely baroclinic forcing, with statistical characteristics motivated by moist convection observed on Jupiter and Saturn, a robust tendency to form a barotropic polar cyclone is identified.

A 2 $\frac{1}{2}$ layer shallow water model is built to test our hypothesis. An 11-dimensional parameter space is explored to determine the most importance controls on cyclone formation. Two sets of experiments are performed: 1) Barotropic and baroclinic 'storms' are briefly forced and then allowed to freely evolve on the polar beta plane, and 2) Forced-dissipative simulations are run, with periodic and randomly placed storms, until statistical equilibrium is reached.

Results confirm the well known tendency of positive vorticity anomalies to self-advect poleward if they are intense enough for nonlinear advection to be significant. Likewise, strong negative vorticity anomalies move equatorward. Simulations span several orders of magnitude of energy density, ranging from weak wave-dominated flows to strong cyclones that experience instabilities. We find that a range of behavior, including what is observed on all four giant planets as well as previous simulation studies, can be expressed by varying only 2 nondimensional control parameters: a second baroclinic deformation radius scaled by the planetary radius, L_{D2}/a; and a total energy parameter $\hat{E}_p$ that scales with the kinetic+potential energy density of the system at statistical equilibrium. In the context of an idealized model, the difference between Jupiter's and Saturn's polar flow regimes may be explained by their different planetary and deformation radii.

Thesis Supervisor: Kerry A. Emanuel
Title: Cecil & Ida Green Professor of Atmospheric Science

Acknowledgments

This thesis is dedicated to my parents. My interest in science has been cultivated with love and selfless support for my entire life, starting with weekly Star Trek episodes and most recently manifesting as hot food and coffee as I finished the thesis. I am certain that I could not have completed a PhD with anything less. I am so grateful to them, and my whole family, for everything.

I cannot adequately express my gratitude for the amazing support I have received on all fronts during both college and graduate school. My two homes-away-from-home, UNH and MIT, are embodied by my favorite academic quote, which I would like to share:

> "And such...is a University. It is a place to which a thousand schools make contributions; in which the intellect may safely range and speculate, sure to find its equal in some antagonist activity, and its judge in the tribunal of truth. It is a place where inquiry is pushed forward, and discoveries verified and perfected, and rashness rendered innocuous, and error exposed, by the collision of mind with mind, and knowledge with knowledge." - John Henry Newman, 1854

This is the intellectual environment that UNH and MIT foster and I have worked hard to take advantage of it. I have been allowed to range and speculate with the best minds in the world, and I am deeply humbled and moved by the opportunity.

Kerry Emanuel, my PhD advisor, has been a steady and wise presence throughout graduate school. I came to MIT not knowing I still had a space problem, and I set to work on terrestrial hurricanes. During discussions with Kerry about a thesis project, he mentioned a bizarre, recently-observed storm on Saturn's south pole, and I was hooked. Kerry graciously let me drift into planetary science while providing a deep understanding of fundamental dynamics. I have benefited as well from seeing a master science communicator work at close quarters. I hope someday to be able to communicate my own science as eloquently and effectively as Kerry does with ease.

Glenn Flierl has formally served as a thesis committee member, but he has essentially acted as a second advisor. He has been incredibly generous with his time and *infinitely* patient with my questions. His ability to immediately perceive the mathematical basis of a problem, and then clearly explain the pros and cons of how to find a solution, helped me make big strides in my work and is something I deeply admire.

I want to thank the other members of my committee as well: Sara Seager, Adam Showman, and Lorenzo Polvani. Sara let me join her group meetings where I was exposed to a vast universe of exoplanets and their possibilities. Adam Showman joined the committee late but caught up on my project alarmingly fast, and has provided very thoughtful and insightful feedback. Lorenzo helped shape the initial proposal. Conversations with other scientists have also contributed to the evolution of this thesis: Paul O'Gorman, James Cho, Peter Weichman, John Marshall, Andy Ingersoll and Raoul Morales-Juberias. The rest of the MIT professors, researchers, lecturers and staff have made being a student in EAPS a real pleasure.

My PAOC friends have provided not just emotional support but help with homework and advice on how to conduct research without going mad. They include but

are certainly not limited to Alli Wing, Tim Cronin, Dan Chavas, Marty Singh, Mike Byrne, Aditi Sheshadri, Malte Jansen and Neil Zimmerman. Many other PAOC and EAPS students, and dear extra-departmental friends, helped keep me happy, grounded and sane. I leave my Generals plant and my unused sled to my younger 54-1815 officemates, in hopes that they too will occasionally flower and never get taken for a ride.

My undergraduate years prepared me well for a PhD and I want to thank the people who made it possible. Eberhard Möbius was my advisor, and trusted bright-eyed 18-year old me and my friend George Clark with an important role on a NASA satellite mission. Beyond the work itself, Eberhard made every effort to help me develop as a scientist and reach for opportunity. This attitude toward undergraduates is less common that it should be, and I'm so grateful for the entire experience. Bob Henry, in his role as Dean while I was there, also provided guidance and support as I navigated classes and grad school decisions. My UNH science friends, George, Sam Meehan and Vasya Vorotnikov helped me get through classes and survive Physics. We all ended up in PhD programs. Bunch of nerds.

Funding: At MIT I have been supported by an MIT Presidential Fellowship and an NSF Graduate Research Fellowship. AT UNH I was funded by the UNH TYCO scholarship. I gratefully acknowledge these funding sources.

Contents

List of Figures

List of Tables

Chapter 1

Introduction

As of this writing, 1,810 confirmed planets have been observed orbiting stars other than our own[1], an increase from one thousand just 12 months ago. This number is expected to grow exponentially in the coming decades as observations and techniques rapidly improve. In our own galaxy, recent observations suggest that 22% of sun-like stars may harbor an Earth-like planet (Petigura et al., 2013). The field of planetary science is making progress by leaps and bounds: it is a good time to be a scientist.

Observations of planets in the neighborhood also continue to improve. A series of NASA flagship missions (e.g. Voyager I and II, Galileo, Cassini) have provided breathtaking views of our neighboring planets, and understanding slowly follows. Now is a particularly exciting time to study the giant planets Jupiter, Saturn, Uranus and Neptune. These massive planets are most similar to the planets that comprise the majority of the current exoplanet population: they are simply bigger and easier to observe. The giant planets provide a rich laboratory for fluid dynamics and challenge our understanding even as new and more exotic worlds are discovered.

The inspiration for the present work is the wealth of observations of Saturn's poles, from land-based telescopes but most notably the remarkable Cassini mission. There exist two very rapid and deep cyclones, one fixed exactly on each of Saturn's poles, that have yet to be explained. Such intense polar cyclones are not observed on the

[1]The NASA Exoplanet Archive is operated by the NASA Exoplanet Science Institute and keeps a running official tally at http://exoplanetarchive.ipac.caltech.edu

other giant planets; rather, each planet offers a different polar flow character, and this itself is a challenge.

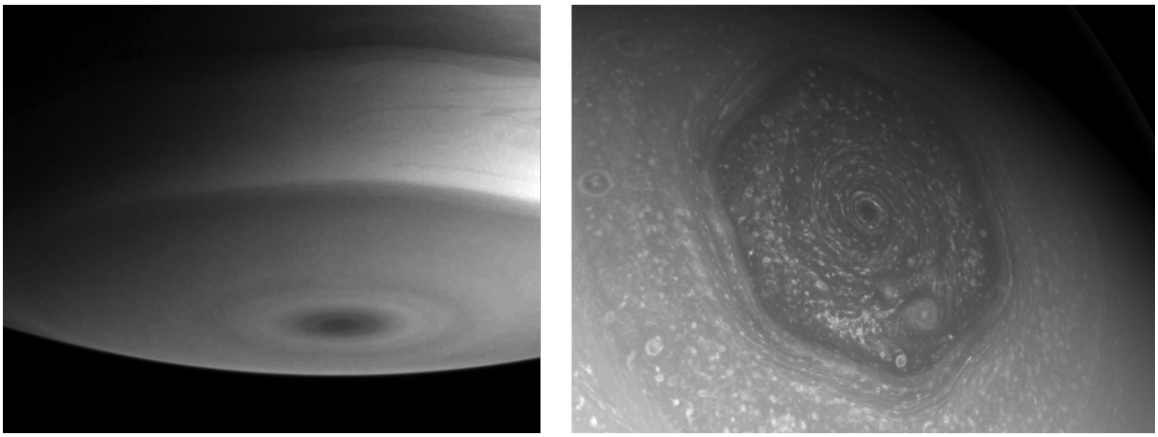

Figure 1-1: Left figure: Saturn's south pole, through upper-atmosphere hazes. Its gross features are strongly zonal. Right figure: Saturn's north pole has a hexagon at 74 degrees N, surrounding the small polar vortex. Notice the local dominance of vortices. These images are taken at different wavelengths; both polar regions have hundreds of vortices. Both figures courtesy NASA/JPL/Space Science Institute.

Planetary scientists benefit from the body of geophysical research developed for Earth phenomena. Earth scientists have put abundant observations and long records to good use, and many simple theoretical models developed in the last 75 years enjoy wide applicability to other planets. Of course, Earth's surface is punctuated by irregular continents and an influential biosphere. In turn then, planetary scientists can aid terrestrial understanding by detailing dynamics on planets without such complications (Dowling, 1993).

The giant cyclones on Saturn's poles present an opportunity to borrow selectively from terrestrial tropical cyclone literature, while imposing alien constraints like a lack of sea surface. The goal is to better understand a robust, dramatic phenomenon, and in doing so to learn more about the extreme limits of fluids on the Earth, on our planetary neighbors, and eventually the likely 8.8 billion planets throughout the galaxy (Petigura et al. 2013; future work).

Chapter 2 offers a partial review of giant planet circulation observations and theories, including a detailed look at the polar observations of Saturn. It describes the

polar cyclone formation hypothesis that drives this work. Chapter 3 is the analytical and numerical model description, including nondimensionalization and subsequent scaling for energy. Chapter 4 provides results from unforced simulations that allow one or several storms to freely evolve. Chapter 5 presents the results of the forced-dissipative experiments, including the usefulness of the energy parameter and the set of regimes it can describe. Chapter 6 discusses more detailed observations, and provides a brief comparison of relevant simulations to observations of Saturn and the other planets. Finally, Chapter 7 concludes.

Chapter 2

The giant planets: global dynamics and a polar hypothesis

2.1 Introduction

The giant planets are essentially spinning spheres of fluid. The circulation of this fluid is poorly observed and even less well understood, but missions such as the Voyagers, Galileo and Cassini have provided sufficient observations for lively debate. The horizontal dark and light bands of the giant planets are concurrent with stable, zonally symmetric, alternating jets (Ingersoll et al., 1979). The gas giants Jupiter and Saturn exhibit strong, prograde, equatorial jets; the ice giants Uranus and Neptune have strong retrograde equatorial jets. The atmospheric flows are visually striking – a roiling combination of vortex creation, merger and death, steered by rapid alternating winds and painted by heavy elements. Jupiter is visually the most interesting planet, but as observations improve the other planets betray their own unique, fascinating dynamics.

We can observe features move with the jets at the top of the weather layer, but do not know how deep these features and motions extend. The planets have a stratosphere and troposphere over a deep, possibly neutral layer (see Lindzen 1977 for a discussion of why a dry convecting fluid may still be stably stratified). Jupiter's and Saturn's compositions are relatively similar to solar composition; they are primarily

hydrogen and helium, with trace heavy elements. Jupiter, the largest planet in the Solar System, is the most similar, with heavy element abundances 3-5 times solar. Saturn is 5-10 times solar in composition, and the ice giants are 30-50 times solar. In the thin, outer weather layer on Jupiter and Saturn, three different constituents are condensible in the troposphere, with water comprising the lowest cloud deck, topped by clouds of ammonium hydrosulfide and then ammonia (Figure 2-1). Above the three clouds at pressures of 200-500 mb, an upper tropospheric haze persists. The ice giants are significantly denser, and are likely only 15-20% hydrogen and helium, and otherwise enriched in heavy elements.

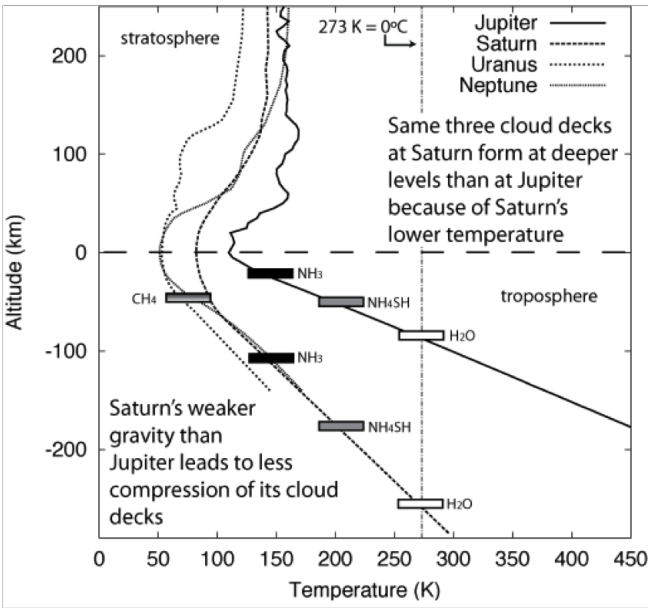

Figure 2-1: The heights of different cloud types on the giant planets, relative to the altitude of the tropopause. Figure courtesy Jere Justus, Marshall Space Flight Center.

The weather layer is statically stable and extends from about 100 mb down to 5-10 bar for Jupiter and Saturn, at the base of the water cloud (Weidenschilling and Lewis, 1973), and 300 bar for Neptune and Uranus (Lunine, 1993). Static stability of Jupiter was observed directly by the Galileo probe down to 22 bar, but this region is anomalously hot and dry (Niemann et al., 1998) and likely not representative of the moist weather layer as a whole (e.g. Showman and Ingersoll 1998, Vasavada et al.

1998).

The giant planets appear 'internally heated'; they are losing heat from the interior to space. This heat is left over from the planet formation process, and may also include a component due to frictional stratification of the well-mixed hydrogen-helium interior. Uranus is a notable exception. Jupiter emits 67% more radiation to space than it receives from the sun (Hanel et al., 1981); Saturn emits 78% more radiation (Hanel et al., 1983); and Neptune emits 161% more (Pearl and Conrath, 1991). Uranus, in contrast, emits no more than 6-10% more energy to space than it receives from the sun (Pearl et al., 1990). Among the internally heated planets, this energy imbalance implies a deep convecting interior, and somehow that heat is being transferred to the free surface. The global circulation responsible for the surface jets, and how they do or do not couple to the deep convecting interior, is a large and active area of research.

2.2 Theory and modeling

Jovian circulation theories can be split into two broad categories: deep circulations and shallow circulations. Each has its own hierarchy of models. There is active work in each category because virtually every spherical model produces jets. It is a ubiquitous feature of large-scale planetary atmosphere simulations, and its ubiquity has done little to constrain what is actually happening in nature.

In a famous paper, Busse (1976) proposed that the jets are surface expressions of deep, concentric, counter-rotating cylinders, tangent to the axis of rotation. Busse's theory addressed the likelihood of a solid core, which would provide the inner radial boundary for the cylinders. Jets would not appear poleward of this boundary, and in 1976 jets had not yet been observed at higher latitudes. Since then, multiple high-latitude jets have been observed that cannot be explained by tangent cylinders (given reasonable estimates of the radius of an inner core).

Nevertheless, Busse's original theory has survived in modified form. In particular, magnetohydrodynamics (MHD) is expected to control the flow on Jupiter at depths

greater than 0.85-0.95 R_{Jup}, where magnetic braking due to electromagnetic torque may become significant (Bagenal et al., 2005). Saturn's smaller mass implies that the corresponding upper limit for MHD may be 0.6-0.85 R_{Sat} (Heimpel and Aurnou, 2007). Even in the absence of electrical fluids, the rapid increase of density with depth likely causes a weakening of the jet speeds with depth (Kaspi et al., 2009). They showed this using an anelastic model, whereas most previous works had assumed a Boussinesq fluid (Christensen 2002, Heimpel and Aurnou 2007). One significant but unavoidable drawback of the deep models is the need to greatly increase the internal heating from observed values; by six orders of magnitude (e.g. Aurnou et al. 2007). Another is their inability to reproduce long-lived cyclone and anticyclones, robustly observed in real atmospheres.

A wide range of models has been employed to explore the origin and maintenance of jets on giant planets, as well smaller features like the Great Red Spot. A hierarchy can be observed in three dimensions: geometry, dynamics and thermodynamics, and generally models have tradeoffs among these dimensions for computational reasons. For example, it is reasonable to model a spherical shell as a Boussinesq fluid, but if one is interested in cloud formation due to latent heating of three different moist constituents with full microphysics Sugiyama et al. (2014), two dimensions (height and width) over a small area are much more tractable than three. Since the jets are the most pronounced and consistent feature of the giant planets, their origin and maintenance are of primary interest to modelers, and require at least a zonal channel (e.g. Showman 2007). Many simulations of jet formation are increasingly performed on full spherical shells (e.g. Cho and Polvani 1996, Scott and Polvani 2007, Lian and Showman 2008, Schneider and Liu 2009, Lian and Showman 2010). There are other, rather creative ways to simulate planetary atmospheric dynamics. Warneford and Dellar (2014) use a novel 'square planet' domain in order to exploit the strengths of graphical processing units for numerical accuracy. Marston et al. (2014) employ cumulant expansions for Direct Statistical Simulation (DSS) of the jets.

The shallow class of models simulates the thin, troposphere-like weather layer. Some authors speculate that an inverse cascade of energy through an inertial range

to the jet scale (Galperin et al. 2006, Choi and Showman 2011) is the cause of the jets. However they may not be the primary cause of the jets (e.g. Panetta 1993). In the Liu and Schneider simulations (e.g. Liu and Schneider 2010), equatorial superrotation is caused by convective Rossby wave generation. Away from the equator, they find that baroclinic eddies due to differential insolation are responsible for midlatitude jets. The solar insolation gradient between the equator and the poles is the primary source of baroclinic instability on Earth, and it drives the midlatitude jets. On the giant planets, the insolation gradient would also provide a source of baroclinic instability, but this may be overwhelmed by the dynamics caused by the high internal heat fluxes. Radiation of energy to space is zonally banded in concert with the jets (Fletcher et al., 2008), and has little resemblance to the solar heating profile.

Even within a particular (shallow or deep) circulation community, the exact mechanism for jet maintenance is still an open question, and may also have a mixed answer. A small but growing body of literature suggests mixed-depth origins for the jets (Vasavada and Showman, 2005). Shallow forcing may drive deep jets (Showman et al., 2006) and deep forcing may drive shallow jets (Kaspi et al., 2009). Another possible cause of baroclinic instability, shear within counter-signed Coriolis gradients with depth due to the Taylor-Proudman theorem, has also been able to drive jets (Kaspi and Flierl, 2007).

Vortices and convective features

Aside from the jets, Jupiter's Great Red Spot (GRS) is the most well known feature among the giant planets. It has been continually observed for over 300 years, and has varied little in that time. It is a massive anticyclone in the Southern Hemisphere tropics, sitting between the equatorial prograde jet to its north and a retrograde jet to its south. Less well observed is Neptune's Great Dark Spot, which lacks such stability and exhibits meridional motion. Jupiter and Saturn have thousands of distinct vortices, most of them anticyclonic (Low and Ingersoll, 1986), that can be seen in high resolution images (Figure 2-2 for example). Observational surveys of vortex abundances are discussed in Chapter 6. These vortices don't necessarily have the

same origin, and their lifetime varies from hours (Little et al., 1999) to centuries (the GRS). Many of the smallest and fastest vortices suggest a moist convective origin, and are reminiscent of thunderstorms on Earth (Gierasch et al., 2000).

Moist convection, specifically due to water clouds, has been hypothesized as the primary weather layer mixing mechanism on the gas giants for decades (Hunt et al., 1982) and may play the primary role in converting internal heat into jets (Gierasch et al. 2000, Ingersoll et al. 2000). A movie composed of Voyager images during the Jupiter flyby captured massive, deep convective events occurring in low latitudes, with a dominant period of approximately 10 days. Roughly calculating the power released by these storms, Banfield et al. (1998) suggest that these common convective storms may be responsible for the majority of the heat flux to space. Ammonia cumulus is unlikely, because the cloud's pressure level is too close to the stable layer to achieve sufficient vertical velocities for plume creation. Water on the other hand may be able to penetrate several scale heights from the base of the water cloud, which is well below the radiative convective boundary, and release significant latent heat (Stoker, 1986).

The upper troposphere is much less convectively active. Banfield et al. (1998) observed well mixed aerosol compositions in the upper troposphere. Given estimates of the radiative time constant on the giant planets, which is on the order of 10-20 years (Conrath et al., 1990), they estimate a lateral mixing times cale of a year or less to account for the chemical homogeneity. This is commonly disturbed by deep convective storms over very small areas, originating from the water cloud layer or below (Little et al. 1999, Li et al. 2004).

Moist convection is now also a leading theory for the maintenance of the jets. Ingersoll et al. (2000) first proposed, using a combination of observations and simple dynamical arguments, that small moist convective features observed on Jupiter and Saturn may provide sufficient forcing to power the jets. This is supported by growing observational evidence of eddy momentum fluxes due to convection (del Genio et al., 2007). Since then, though few GCMs are able to yet resolve such small and intense features, Lian and Showman (2010) successfully produce superrotating jets on the gas giants, and retrograde jets on the ice giants, with simple water phase changes and

attendant latent heating. In fact, they found that the planetary water abundance was the most important control parameter. The water abundances are still unobserved, but Jupiter is expected to have the least, at a few times solar abundance, and Saturn double that or more (e.g. Mousis et al. 2009). The ice giants are believed to have the greatest water abundances.

2.3 The poles of Jupiter, Uranus and Neptune

This work is concerned with polar regions, which exhibit the largest variation of dynamics among the planets. There are jets, and vortices, and convective clouds, to some degree across all of them, and an understanding of one planet's behavior should be consistent with the differences among the others. Saturn is best observed, but observations of various fidelity have been taken of each planet.

Before Cassini spotted the rapid polar cyclones on Saturn, it flew by Jupiter and sent back detailed observations of the atmosphere. Porco et al. (2003) discovered multiple counter-rotating polar jets poleward of 70°S, dominated by small, zonally confined, coherent vortices. These jets are not apparent in still images, but a time-lapse shows just how zonal the vortex motion is. It was previously believed that these abundant cyclones and anticyclones swim around the polar region more freely.

To date, no detailed observations have been taken of Jupiter's exact poles, but the polar region within 2° of the pole has been observed. The broad collar of low vorticity surrounding the SPV of Saturn does not appear to have a counterpart on Jupiter, and some authors refer to Jupiter as lacking similar polar storms. The observations will improve with the spacecraft Juno's arrival at Jupiter in 2016.

Thermal imaging of Neptune's south polar stratosphere in 2005 shows a very localized hot spot immediately on the south pole (within resolution error; Hammel et al. 2007), which remains unexplained. The broader polar stratospheric collar is perhaps as much as 4-5 K warmer than its surroundings, likely due to long seasonal heating. Limited observations of the feature and the inability to image the north pole at the same time make differentiating the cause very difficult. In 2007, the

same region was observed and shows a different phenomenon: one bright cloudy feature on the pole on July 26th appeared as two cloudy bright features on July 28th; adjacent at 89°S and 87° (Luszcz-Cook et al., 2010). Both Uranus and Neptune exhibit transient atmospheric features that cannot be explained by seasonal changes and are likely of convective origin (Hammel and Lockwood, 2007). Though Uranus appears uncommonly bland among the giant planets, a reanalysis of Voyager data shows rapid, narrow polar jets and likely moist convective activity (Karkoschka, 2014), and their atmospheric activity appears to be increasing in recent years.

2.4 Saturn's polar cyclones

In 2004, the Keck Observatory discovered a warm vortex situated on Saturn's south pole (Orton and Yanamandra-Fisher, 2005). This discovery was shortly followed by infrared imaging of both polar hemispheres by Cassini, with the surprising result that both poles exhibit very localized hot spots in the troposphere of each pole, regardless of season (Fletcher et al. 2008, Figure 2-2). These hot spots are 6-8 K warmer than fluid that is 10° from the pole. The warm anomalies extend downward at least as far as the lower limit of the observations, at 1 bar.

Polar vortices have been observed on Earth, Venus, Jupiter and Neptune, but they are all cold or only slightly warmer than their immediate surroundings. Saturn's south polar vortex (SPV), in contrast, is the warmest location on the planet's surface. The Cassini mission, currently in orbit around Saturn, subsequently took high resolution images of the SPV in multiple wavelengths in 2005 (Vasavada et al., 2006). Sánchez-Lavega et al. (2006) find a peak tangential velocity of 160±10 m/s at 87° (3000 km from the pole). They characterize this feature as an asymmetrical jet - winds go to zero at the pole, and reach null velocities equatorward at 80°S.

In 2006 a second south polar survey was taken and reported by Dyudina et al. (2009). They identify multiple 'hurricane-like' features, including an analogue of hurricane eyewalls: the vortex has concentric annuli of tall convective clouds, dropping shadows as the planet rotates over a deep and largely clear, anomalously warm eye.

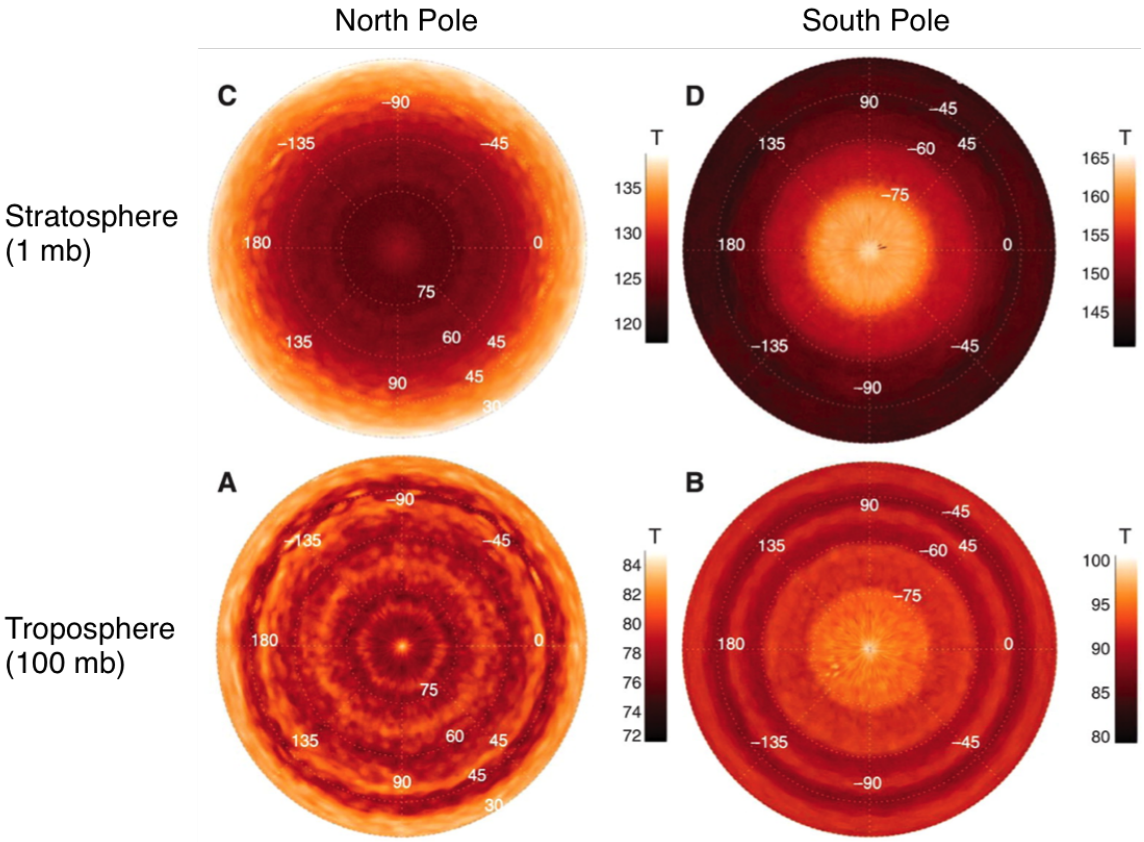

Figure 2-2: Figure 1 from Fletcher et al. (2008). Temperatures are in Kelvin. Reprinted with permission from AAAS.

The inner eyewall has a horizontal wavenumber-2 distortion, and an estimated height that varies with longitude - from 30-60 km to 70-120 km, as measured by shadow lengths (Dyudina et al., 2009). The outer wall is azimuthally symmetric with a lower estimated height of 30-40 km. The eye itself is consistently the warmest place imaged on the whole planet, and very high resolution photos show seemingly two-dimensional vortical mixing.

The north pole of Saturn also has a warm core cyclonic vortex (Baines et al., 2009) though it lacks annuli, has a slower jet and is slightly cooler than its southern counterpart. Its similar warm signature and polar jet suggest that it is dynamically like the SPV; no other planets exhibit such deep and rapid polar cyclones.

The SPV is in fact the longest-lived cyclone ever observed in the Solar System. Its eyewalls, rapid circular jet and deep clear eye are reminiscent of hurricanes; yet the thermodynamic mechanism must be fundamentally different. Tropical cyclones on Earth derive their energy from the thermal disequilibrium between the boundary-layer air and the much warmer ocean surface (Emanuel, 1986). Gas giants don't have such a sharp air-ocean phase transition in the weather layer. Nonetheless, there is a remarkable number of similarities between terrestrial hurricanes and the SPV, detailed very thoroughly in Dyudina et al. (2009) (their section 8).

2.5 A moist convective hypothesis

The polar cyclone hypothesis central to this thesis borrows from ongoing debate in the terrestrial hurricane literature. The hurricane community has not resolved the role of local, deep convective towers in hurricane formation and maintenance. Some authors argue that azimuthally symmetric fluxes over the sea surface are sufficient for hurricane growth (e.g. Emanuel 1986), and that strong eddies are deleterious for intensification (e.g. Nolan and Grasso 2003). Others maintain that deep convective towers pump vorticity into the mean flow (Montgomery et al., 2006). This last theory is appealing to a planetary scientist who wants to make a hurricane without an ocean. Deep convective towers on Earth converge high angular momentum air at their base,

creating a positive potential vorticity (PV) anomaly. Moist air rises rapidly through the cumulonimbus cloud, releases latent heat, and diverges just below the tropopause, leading to a negative PV anomaly. Montgomery et al. (2006) contend that these anomalies can react with the environment and strengthen a hurricane. The drift mechanism is explored in Chapter 3 - simply, small PV anomalies can 'feel' PV gradients, and positive anomalies tend to move upgradient, while negative anomalies move downgradient. This effect is well understood theoretically and helps explain the early, tropical motions of hurricanes on Earth, before midlatitude winds start to steer them into the jet stream.

The ingredients for precisely this behavior, which does not necessarily require a sea surface, exist on Saturn's poles. Dyudina et al. (2009) measure the mean winds of the surrounding flow as well as local feature characteristics. The flow surrounding the vortex is dominated by small anti-cyclonic vortices advected by the nearly-irrotational flow outside the outer eyewall. Aside from serving as tracers for the mean flow, a number of them also have a measurable individual relative velocity, and the figure is reproduced from their paper here as Figure 2-3. The warm marker colors indicate a positive relative vorticity, which is anticyclonic in the southern hemisphere.

We propose that the abundance of anticyclonic vortices in the SPV region are the tops of deep tropospheric convective towers, rooted in or below the water cloud. This would imply that their anticyclonicity is balanced by a cyclonic anomaly near the cloud base, which may react to the Coriolis gradient of the planet and move upgradient, or poleward. Over time, a large enough poleward flux of cyclonic vorticity may be sufficient to condense and maintain a polar cyclone.

Baines et al. (2009) speculate that the small cloud features may deliver energy to the north polar cyclone on Saturn, if they are indeed of moist convective origin, though he did not provide a mechanism. Other authors (e.g. Ingersoll et al. 2000) have envisioned exactly this mechanism for the jets but not for the polar cyclones.

A few idealized modeling studies and laboratory experiments have specifically studied the dynamics of giant planets' shallow polar atmospheres. They provide evidence that the drift of small positive anomalies is indeed sufficient to create a polar

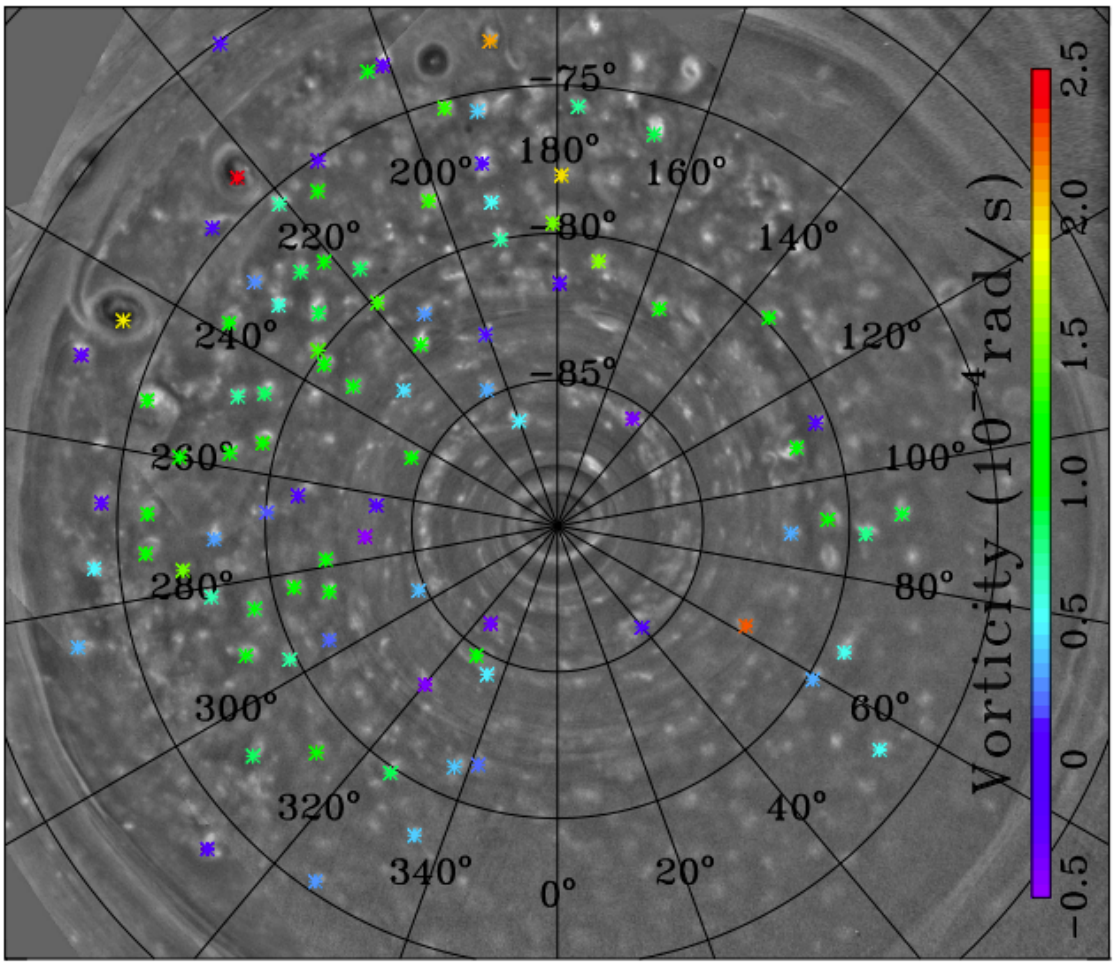

Figure 2-3: Figure from Dyudina et al. (2009). A plan view of the south polar vortex provides relative vorticity estimates overlain on Cassini images. Warmer colors indicate anticyclones. The deep, clear eye of the SPV is on the pole, in the center of the domain. The first cloudy eyewall lies 1000 km radially from the pole, and second lies 2000 km from the pole. Reprinted from Icarus, 202, Dyudina et al., Saturn's south polar vortex compared to other large vortices in the Solar System, Pages 240-248, Copyright 2009, with permission from Elsevier

cyclone. Scott (2011) employs a polar beta plane to study the motion of patches of cyclones and anticyclones on a pole. His quasi-geostrophic single layer simulations demonstrate the genesis of a polar cyclone due to beta drift. The cyclone tends to orbit the pole in equilibrium, strongly mixing the rest of the fluid in the polar cap. Scott and Polvani (2007) use a forced-dissipative model with full spherical geometry, and also find a polar cyclone that swims freely around the pole, constrained by the poleward most jet. A theme emerges, as Liu and Schneider (2010) also find a broad polar cyclone that precesses around the pole.

In this work we ask whether moist convection alone, parameterized as baroclinic forcing intermittent in time and space, is sufficient to create these equivalent barotropic polar cyclones that other authors have observed - and if so, under what conditions.

Chapter 3

Building the model

3.1 Choosing the shallow water system

In the 1970s, rapid theoretical progress was made in giant planet circulations, by Stone (1972), Rhines (1975), Williams (Williams and Robinson 1973, 1975,b, 1978) and others. The earliest spherical modeling study of shallow jovian flows used the nondivergent barotropic system, Dq/Dt = forcing + dissipation, for a total vorticity q that is a sum of the relative vorticity ξ and the latitudinally-varying planetary vorticity $f = 2\Omega sin\theta$ (Williams, 1978). The flow is completely rotational, so a streamfunction ψ can be defined: $u = -1/r\partial\psi/\partial\theta$ and $v = 1/[r\cos\theta]\partial\psi/\partial\lambda$ for latitude θ, longitude λ and planetary radius r. Euler's equation for an inviscid fluid is then

$$\frac{\partial q}{\partial t} + J(\psi, q) = \text{forcing} + \text{dissipation} \tag{3.1}$$

for a spherical Jacobian operator J used for advection. In this system, interactions between vortices are very long range, due to the logarithmic nature of the Green's function of the two-dimensional Poisson operator ∇^2 which acts on the streamfunction. This simple model is able to produce counterrotating jets, qualitatively similar to those of the giant planets, though lacking equatorial superrotation.

In pure 2D turbulence, energy undergoes an inverse cascade to smaller wave numbers (larger scales) until fluid motions are damped or reach the scale of the domain.

3D turbulence experiences a direct cascade of energy to the smallest scales, where it is lost to friction. On Earth, the thin envelope of atmosphere is virtually two-dimensional with respect to the planetary scale, but small scale events like moist convection and large scale events like nonlinear Rossby waves and associated pressure systems cause the atmosphere to stretch and contract. On the giant planets, a scale analysis suggests that the deep interior convection has little similarity to 2D turbulence. However, in the thin weather layer where moisture can release latent heat and cause fluid column stretching, geostrophic turbulence is probably an apt characterization of fluid motions (though too simple to account for actual moisture).

In a 2D fluid on a plane with a monotonic variation in background vorticity, a Rhines scale (Rhines, 1975) can be found that indicates the threshold of zonal-motion dominated flows. At small scales, $l < L_D$ ($k > k_D$), geostrophic turbulence is generally two-dimensionally isotropic. Motions at larger scales ($k < k_D$) are inhibited in the zonal direction. More precisely, a two dimensional fluid experiences an inverse energy cascade until motions reach the largest scales - unless a planetary vorticity gradient re-directs this cascade into more zonal motions at some horizontal scale proportional to the gradient. Rhines found this scale to be $\sqrt{(}\pi U/\beta)$ for a characteristic velocity U and a planetary Coriolis gradient β; and it corresponds closely to the observed widths of the jets on the giant planets (e.g. Williams 1975).

In a divergent fluid, such as the quasi-geostrophic system, the deformation radius L_D marks a transition between short-scale, strong logarithmic interactions between anomalies $l < L_D$ distance apart, and weaker interactions that fall off exponentially with distance for $l > L_D$. This is because the advection is now expressed by the Helmholtz operator, $\nabla^2 + (1/L_D)^2$, and some of the system energy is stored in height or pressure deviations as available potential energy, where it can be possibly released during baroclinic instability if there is more than one vertical mode. L_D is also approximately the smallest scale at which a fluid can store energy as potential energy, in vertical perturbations of the geopotential.

The impact of the Rhines scale changes in the presence of a positive definite L_D. A small deformation radius has been found to suppress Rossby wave radiation and there-

fore the Rhines effect, i.e. the creation of zonal jets, for the quantity $U/(L_D^2\beta) >> 1$ (Okuno and Masuda 2003, Smith 2004, Showman 2007, hereafter S07; Penny et al. 2010). Because both L_D^2 and $|\beta|$ decrease poleward, the tendency for jets to form decreases poleward and the fluid approaches isotropic geostrophic turbulence, dominated by small-scale vortices. Observations of Jupiter and Saturn demonstrate this qualitative behavior (e.g. Vasavada et al. 2006).

After the early barotropic simulations, a family of layered QG and shallow water models were used (see Achterberg and Ingersoll 1989 for an overview of studies at that time), but either omitted true baroclinic instabilities (e.g. Ingersoll and Cuong 1981, Marcus 1990) or had solid bottom boundaries (e.g. Read and Hide 1983). Achterberg and Ingersoll (1989, 1994) derived a normal-mode QG model with an abyssal bottom layer and 3 modes: a 1st and 2nd baroclinic mode, and a barotropic mode that can exist if the abyssal layer is allowed a horizontal flow.

Studies using a hierarchy of models for shallow flows have since proliferated, and the literature on the formation and maintenance of jovian jets is vast. Most of these works resolve the polar region to some extent, but very few focus on polar dynamics, due in part to a lack of comparable polar observations (until recently, thanks to Cassini).

We want to understand the dynamics that can lead to a Saturn-like polar cyclone, and perhaps explain its absence on the other planets. In this decade, divergent models are trivial to run, and provide a tunable deformation radius that can be compared with estimates for each giant planet. However, the 3D primitive equations may be too complex for this study, since a continuously stratified system has a large (can be numerically truncated from infinity) number of vertical baroclinic modes. It is likely unnecessary to include the dynamic effects of higher baroclinic modes on large scale dynamics, since moist convection is our driving motivation and it has a clear wavenumber 2 signal in the vertical.

On the other hand, the QG system might be too simple. Outside the equatorial region, the set of QG assumptions is appropriate for early explorations of shallow gas giant dynamics. However, there are several aspects of polar dynamics that may

render the QG system too restrictive:

1. The Rossby number of Saturn's SPV may be as high as 1 (Dyudina et al. 2009). The Rossby number suggests a cyclone in gradient wind balance, and the QG system is only valid for motions in approximate geostrophic balance.

2. Observations over decades show a significant cyclone/anticyclone population asymmetry, among small vortical features, on both Jupiter and Saturn (e.g. Low and Ingersoll 1986, Vasavada et al. 2006). The reason is unknown. The SW system also demonstrates a strong cyclone-anticyclone asymmetry: anticyclones are more stable and longer lived as the Froude number increases, even without a planetary vorticity gradient β (Polvani et al., 1994). Polvani et al. speculate that this is in part due to the fact that anticyclones have a larger effective deformation radius than cyclones, because anticyclones are relatively thicker than the surrounding fluid. The QG system cannot capture this behavior because it linearizes potential vorticity.

3. The SW system assumes that $H << L$; the QG system goes one step farther and assumes that $h' << H$. The QG system is not inappropriate for oceanic warm core rings (Flierl, 1984), and may also be a poor fit for the SPV, because its center is the deepest, hottest place observed on the entire planet, representing a significant deviation in geopotential.

We choose a $2\ \frac{1}{2}$ layer shallow water system centered on the pole for this study. The shallow water system uses the hydrostatic assumption and its mass continuity does not permit sound (compressional) waves. For the shallow atmospheres of the giant planets, this should not impact the dynamics, because it is very fast (around 10 km/s; Kanamori 1993). A $2\frac{1}{2}$ layer model does not permit a barotropic mode, due to its abyssal bottom layer (we don't add an 'active' abyssal layer option, wherein deep barotropic winds are permitted, as Achterberg and Ingersoll (1989) do), but it does permit two baroclinic modes. A two layer model, whether or not it has an abyssal bottom layer, is the simplest fluid model that allows baroclinic instability. The

advantage of the abyssal layer is that it represents the deep and neutrally stratified fluid underneath what can be considered a moist troposphere, and it may deform slightly due to tropospheric dynamics.

3.2 Model geometry

Since the feature of interest in this study is in the immediate polar region, it is unnecessary and inefficient to model a spherical shell. On Saturn, which provides the primary motivation for our model decisions, the polar caps are enclosed by a jet at 75° in the Southern Hemisphere (Vasavada et al., 2006) and 74° in the Northern Hemisphere, which likely act as strong barriers to mixing (Dritschel and Mcintyre, 2008).

One common concern about modeling a polar region is the singularity that occurs at the pole when using cylindrical or spectral coordinates, as the longitudinal grid spacing approaches zero. Some spectral models employ a polar filter to remove spurious gradients, or reduce the number of grid points poleward; others used cubed spheres or other polyhedrons. Since this work is motivated by behavior exactly on and exclusive to a pole, we want to avoid this issue entirely. We use a Cartesian grid with the origin $(x, y) = (0, 0)$ on the pole, so that the model discretization is agnostic to the pole's location (other than the Coriolis parameter function defined at each x, y). The domain is doubly periodic, which allows us to prevents corner effects, but it causes a discontinuity in the Coriolis gradient β at the open boundaries. To mitigate the possibility of features leaving and re-entering the domain at opposite longitudes, we impose an azimuthally symmetric sponge layer at each time step. This sponge layer is a simple Rayleigh damping term, and the damping time scale decreases linearly from infinity to 0.8 days with radius. For domain size L^2, the sponge layer generally begins at radius $L/2 - 0.5L_{D2}$, for a second baroclinic deformation radius L_{D2} described in Section 3.4. This sponge layer acts too slowly to absorb fast gravity waves. However, in the parameter space of interest, storms develop relatively slowly and so gravity waves are not strongly excited.

The pole is a unique place, where the planetary vorticity gradient reaches zero. A traditional beta plane is not appropriate here because of the quadratic nature of the gradient. We use the polar beta plane (Bridger and Stevens, 1980) to approximate the planetary vorticity gradient near the pole. The polar beta plane is a small-angle Taylor series around co-latitude ϕ:

$$f = f_0 \cos\phi \tag{3.2}$$
$$= f_0\left(1 - \frac{\phi^2}{2!} + \frac{\phi^4}{4!} - ...\right) \tag{3.3}$$
$$\approx f_0\left(1 - \frac{r^2}{2a^2}\right) \tag{3.4}$$

The Coriolis frequency $f = f_0 - \beta r^2$, where $r^2 = x^2 + y^2$, and $\beta = f_0/(2a^2)$ has units of $\mathrm{m}^{-2}\mathrm{s}^{-1}$. Throughout the paper, all sign conventions are consistent with Northern Hemisphere flows, to reduce potential confusion; however we avoid the term 'counterclockwise' and only refer to cyclonicity of flows.

3.3 Model equations

The model iteratively solves for layer velocities and heights at each time step. The dimensional model parameters are listed in Table 3.1. Subscripts 1 and 2 refer to the upper and lower layers, respectively.

$$\frac{\partial \vec{u}_1}{\partial t} = -(f_0 - \beta\vec{x}^2 + \zeta_1)\hat{k} \times \vec{u}_1 - \nabla(g_{31}h_1 + g_{32}h_2 + \frac{1}{2}|\vec{u_1}|^2)) - \nu\nabla^4\vec{u}_1 \tag{3.5}$$
$$\frac{\partial \vec{u}_2}{\partial t} = -(f_0 - \beta\vec{x}^2 + \zeta_2)\hat{k} \times \vec{u}_2 - \nabla(\frac{\rho_1}{\rho_2}g_{32}h_1 + g_{32}h_2 + \frac{1}{2}|\vec{u}_2|^2)) - \nu\nabla^4\vec{u}_2 \tag{3.6}$$
$$\frac{\partial h_1}{\partial t} = -\nabla \cdot (\vec{u}_1 h_1) + S_{st} - \frac{h_1 - H_1}{\tau_{rad}} + \kappa\nabla^2 h_1 \tag{3.7}$$
$$\frac{\partial h_2}{\partial t} = -\nabla \cdot (\vec{u}_2 h_2) - S_{st} - \frac{h_2 - H_2}{\tau_{rad}} + \kappa\nabla^2 h_2 \tag{3.8}$$

where $g_{ij} = g(\rho_i - \rho_j)/\rho_i$, ν is the hyperviscosity coefficient and κ is the regular

Parameter	Meaning
f_0	Coriolis parameter
a	planetary radius
H_1	upper layer average thickness
H_2	middle layer average thickness
ρ_1/ρ_2	density ratio
g_{31}	$g(\rho_3 - \rho_1)/\rho_3$
g_{32}	$g(\rho_3 - \rho_2)/\rho_3$
τ_{st}	storm lifetime
τ_{stper}	storm period
τ_{rad}	radiative relaxation timescale
R_{st}	storm radius
W_{st}	storm vertical velocity
ν	viscosity
κ	diffusivity
#	simultaneous storm number

Table 3.1: Dimensional parameters and their definitions.

(not hyper) diffusion coefficient. Upper and lower layer thicknesses are h_1 and h_2 respectively, and they along with upper and lower velocities $\vec{u}_1$ and $\vec{u}_2$ are the six variables that the model iterates in time.

3.3.1 Physical forcing and dissipation

In previous works using 1 or 1 $\frac{1}{2}$ layer models, such as Scott (2011), authors either use a barotropic wavenumber forcing, or seed the domain with coherent blobs of both cyclones and anticyclones. The former has no moist convective analogue, which would require a scale separation between rising and falling motions. The latter only conserves domain-wide potential vorticity if the ratio is one. Both options lack vertical structure, and therefore cannot permit interactive baroclinic instability.

This is the first model that uses a baroclinic forcing to drive a barotropic polar cyclone. The storm forcing function S_{st} simulates a moist convective environment with

localized deep convective towers, shaped as truncated Gaussians in space with constant amplitude in time. This is a 'boxcar' or step function in time, but gravity waves are not strongly triggered because the peak vertical forcing velocity is generally very low. Convection is simulated by locally depressing the middle interface, as if a storm is fluxing mass from the middle to top layer, and simultaneously raising the environmental interface slightly to conserve layer mass at each time step ("subsidence").[1] Of course, this forcing is actually dry, but the vertical velocities and areal extents of the convecting regions parameterize the behavior of a moist, statically stable atmosphere.

The storms are randomly placed in space and are either 'on' or 'off' in time, such that at any given moment, either all storms in the domain are occurring with constant amplitude, or the forcing function has been shut off. See S07 for a very similar forcing for 1 $\frac{1}{2}$ layer midlatitude simulations of Jupiter (other examples are Li et al. 2004, Smith 2004). In that work as in ours, forcing and dissipation in the momentum equations are expressly avoided, in order to more realistically simulate an essentially inviscid weather layer. An additional degree of freedom which we do not add to this model is the ability of storms to advect according to some appropriately weighted mean wind speed *while* they grow. One could argue that deeply rooted storms either move negligibly during their brief active lifespan, or move with the upper winds of the neutrally buoyant abyssal layer (which would have an independent stream function that we do not provide in this model). In any case, fixing the storm location has not impeded the potential for polar cyclogenesis in our simulations, and so that advance is left for future work.

Here, our storm forcing function S_{st} is:

[1]Downdrafts in the vicinity of deep convection may be similarly localized and nearly as intense as others have found in observations (Gierasch et al., 2000) and jovian simulations (Lian and Showman, 2010). We omit that complexity here, assuming instead a constant subsidence in the remainder of the domain. This may be a particularly poor assumption for the polar region, where the deformation radius reaches a minimum and may confine downdrafts.

$$S_{st} = \begin{cases} \sum_{j=1}^{\#} W_{st} \exp\left[-\frac{1}{R_{st}} \frac{(\vec{x}-\vec{x_j})^2}{0.36} \right] + \text{subsidence}, & \text{if } t_{clock} \leq \tau_{st} \\ 0, & \text{if } \tau_{st} < t_{clock} \leq \tau_{stper} \end{cases} \tag{3.9}$$

for a t_{clock} that resets to 0 every time it equals τ_{stper}, which is the storm period (storm lifetime τ_{st} plus some inactive period between storms). The factor of 0.36 in the denominator of the Gaussian exponent adjusts the vortex width such that R_{st} is approximately the radius at which the amplitude is $W_{st}/2$ (full-width half-max: FWHM).

Radiative relaxation is the only large scale energy removal in our model, and it acts on the thickness perturbations only (as in S07 and Scott and Polvani 2008). The estimated radiative timescale on Saturn is quite high; approximately 9 Earth years (Conrath et al., 1990). This is too high for our computational resources. Values used in this study range from 150-400 days, and still $\tau_{rad} >> \tau_{st}$. This is more physically motivated on giant planets than energy removal schemes used in some previous works. Hypoviscosity, with no clear physical interpretation, has been used by Scott and Polvani (2007); they also consider linear Rayleigh drag. The Liu and Schneider papers (2010, 2011, Schneider and Liu 2009) also use Rayleigh drag, but impose it everywhere except the equatorial region. In those papers the bottom boundary is only at a pressure of 3 bar, which may be above the water cloud, but the stated motivation for linear drag is the cumulative effect of MHD drag much deeper. Our radiative relaxation scheme removes APE without removing mass, by damping thickness perturbations.

On a sphere, a major drawback to energy removal through radiative relaxation is the energy balance at the equator, with its weak horizontal gradients. As the Rossby radius approaches infinity at the equator, thickness perturbations decrease and so radiative damping becomes much less efficient at removing energy on reasonable timescales. We do not suffer this difficulty, since we simulate only a polar cap near geostrophic balance, so radiative relaxation is the obvious choice for energy removal.

In this model, the radiative timescale is the same for each layer. This is more for simplicity than based on physical intuition and future work should explore more complicated layer radiative functions.

3.4 Nondimensionalizing the model

Our 2 $\frac{1}{2}$ layer model assumes an infinitely deep and quiescent bottom layer, which precludes a barotropic mode. We can speak of the first baroclinic mode, also known as the 'equivalent barotropic mode' in a reduced gravity model; and a second baroclinic mode. Because our system is nonlinear and divergent, these modes are coupled and cannot fully describe its behavior; yet they provide us with more physically relevant gravity wave speeds than those for each layer. The second baroclinic mode is associated with the smallest deformation radius of the system. We choose to normalize our model by this radius in order to ensure consistent resolution of small scale enstrophy and vortical filaments, such that a horizontal length of '1' is equal to the second baroclinic deformation radius L_{D2}. At the same time, the CFL condition prevents the first baroclinic gravity wave speed from being too high in what must be a computationally inexpensive model.

The baroclinic gravity wave speeds can be expressed as a linear combination of layer gravity wave speeds. Assume modal solutions to the linearized, non-rotating system such that $u_2' = \mu u_1'$ and $h_2' = (H_2/H_1)\mu h_1'$, and let c_1 and c_2 be the upper and lower gravity wave speeds respectively; then:

$$\mu^2 + \big(\frac{c_1^2}{c_2^2} - 1\big)\mu - \frac{\rho_1}{\rho_2}\frac{H_1}{H_2} = 0 \tag{3.10}$$

Our first and second baroclinic (squared) gravity wave speeds are, respectively:

$$c_{e1}^2 = c_1^2 + \mu^{(+)} c_2^2 \tag{3.11}$$

$$c_{e2}^2 = c_1^2 + \mu^{(-)} c_2^2 \tag{3.12}$$

We scale our dimensional parameters in the following way:

$$(x, y) = L_{D2}(x', y') \tag{3.13}$$

$$h_i = H_i h_i' \tag{3.14}$$

$$\vec{u}_i = c_{e2} \vec{u}_i' \tag{3.15}$$

$$t = 1/f_0 t' \tag{3.16}$$

where the primed variables are dimensionless.

The Buckingham Pi theorem states that for any system with m independent dimensional parameters in n dimensions, there exist $m - n$ nondimensional parameter groups that fully describe the system's behavior. In the shallow water system, there are only 2 independent dimensions: length and time. Thus we can reduce our 15-parameter system to 13 parameters by scaling each parameter by either a length and/or time scale, such that the scaled parameter is unit less. Nondimensionalization in textbooks and well-behaved physical models commonly involves scaling to arrive at a Rossby number, and occasionally a Froude number. In such cases it is appropriate to fix nondimensional parameters in this way, because the system behavior is further constrained by a forcing chosen in advance to result in particular behavior. However, we want to avoid scaling that assumes a 'typical' horizontal velocity, to arrive at nondimensional parameters such as the Rossby (e.g. Held and Hou 1980, Mitchell and Vallis 2010) and Froude numbers (Vallis, 2006). It is possible that this system will demonstrate different flow regimes in its very large parameter space, and we do not know *a priori* even the order of magnitude of typical velocities in the system. Therefore, we choose to scale our system by functions of the control parameters only,

Symbol	Parameter	Meaning
$\tilde{c}_1^2$	c_1^2/c_{e2}^2	scaled 1st layer GW speed
$\tilde{c}_2^2$	c_1^2/c_{e2}^2	scaled 2nd layer GW speed
H_1/H_2		aspect ratio
Br_2	L_{D2}^2/R_{st}^2	2nd baroclinic Burger number
$\tilde{\beta}$	$L_{D2}^2/(2a^2)$	scaled β
Ro_{conv}	$W_{st}/(H_1 f_0)$	convective Rossby number
ρ_1/ρ_2		layer stratification
$\tilde{\tau}_{st}$	$\tau_{st} f_0$	scaled storm duration
$\tilde{\tau}_{stper}$	$\tau_{stper} f_0$	scaled storm period
$\tilde{\tau}_{rad}$	$\tau_{rad} f_0$	scaled radiative timescale
#		simultaneous storm number
Re	$c_{e2} L_{D2}/\nu$	Reynolds number
Pe	$c_{e2} L_{D2}/\kappa$	Peclet number

Table 3.2: Nondimensional parameters and their definitions. L_{D2} is the second baroclinic deformation radius, equal to the second baroclinic gravity wave speed c_{e2} divided by f_0.

and consider the Rossby and Froude numbers to be nondimensional descriptors of the behavior at statistical equilibrium. We still can define a convective Rossby number, $Ro_{conv} = W_{st}/(f_0 H_1)$, since its components are all control parameters (as in Kaspi et al. 2009), but this should not be confused with the global Rossby number that results from horizontal velocity and length scales. The 13 nondimensional parameters are listed in Table 3.2.

The Burger number appears in the forcing term because the specified storm radius is an additional length scale. The parameters ρ_1/ρ_2 and # remain the same since they were nondimensional to begin with. We normalize horizontal lengths by L_{D2}, thicknesses by H_1 and time by f_0^{-1}. Our nondimensional shallow water system is (primes are dropped):

$$\frac{\partial \vec{u}_1}{\partial t} = -(1 - \tilde{\beta}\vec{x}^2 + \zeta_1)\hat{k} \times \vec{u}_1 - \nabla\left(\tilde{c}_1^2 h_1 + \tilde{c}_2^2 h_2 + \frac{1}{2}|\vec{u}_1|^2\right) - \mathrm{Re}^{-1}\nabla^4 \vec{u}_1 \tag{3.17}$$

$$\frac{\partial \vec{u}_2}{\partial t} = -(1 - \tilde{\beta}\vec{x}^2 + \zeta_2)\hat{k} \times \vec{u}_2 - \nabla\left(\gamma\tilde{c}_1^2 h_1 + \tilde{c}_2^2 h_2 + \frac{1}{2}|\vec{u}_2|^2\right) - \mathrm{Re}^{-1}\nabla^4 \vec{u}_2 \tag{3.18}$$

$$\frac{\partial h_1}{\partial t} = -\nabla \cdot (\vec{u}_1 h_1) + S_{st} - \frac{h_1 - 1}{\tilde{t}_{rad}} + \mathrm{Pe}^{-1}\nabla^2 h_1 \tag{3.19}$$

$$\frac{\partial h_2}{\partial t} = -\nabla \cdot (\vec{u}_2 h_2) - \frac{H_1}{H_2} S_{st} - \frac{h_2 - 1}{\tilde{t}_{rad}} + \mathrm{Pe}^{-1}\nabla^2 h_2 \tag{3.20}$$

$$S_{st} = \begin{cases} \sum_{j=1}^{\tilde{\#}} Ro_{conv} \exp\left[- B_{r2} \frac{(\vec{x} - \vec{x_j})^2}{0.36} \right] + \text{subsidence}, & \text{if } \tilde{t}_{clock} \leq \tilde{\tau}_{st} \\ 0, & \text{if } \tilde{\tau}_{st} < \tilde{t}_{clock} \leq \tilde{\tau}_{stper} \end{cases} \tag{3.21}$$

for a $\tilde{t}_{clock}$ that resets to 0 every time it equals $\tilde{\tau}_{stper}$. The γ term is equal to $(\rho_1/\rho_2)(\tilde{c}_2^2/\tilde{c}_1^2)(H_1/H_2)$, and is equivalent to the γ used in the 2 $\frac{1}{2}$ layer model of Simonnet et al. (2003).

The nondimensional Coriolis gradient parameter, $\tilde{\beta}$, provides a measure of the Coriolis gradient with respect to the second baroclinic deformation radius L_{D2} in the nondimensional model. For constant f_0, a planet with large $\tilde{\beta} = L_{D2}^2/(2a^2)$ will have small values of a/L_{D2}: around 20 or 30. A planet with small $\tilde{\beta}$ has $a/L_{D2} = 40+$. These are both used throughout the paper.

3.4.1 Numerical considerations

The Cartesian grid is a staggered Arakawa C-grid. The time-stepping scheme is a 2nd order Adams-Bashforth algorithm. Early tests showed that this provided dynamics nearly identical to the 3rd order Adams-Bashforth scheme. Horizontal hyperviscosity ∇^4 is used instead of viscosity to reduce its impact on the dynamics, which at upper levels on giant planets is virtually inviscid.

The Reynolds and Peclet numbers are fixed at the highest value that empirically permits consistent numerical stability (5e4 and 1e5 respectively), so we explore an

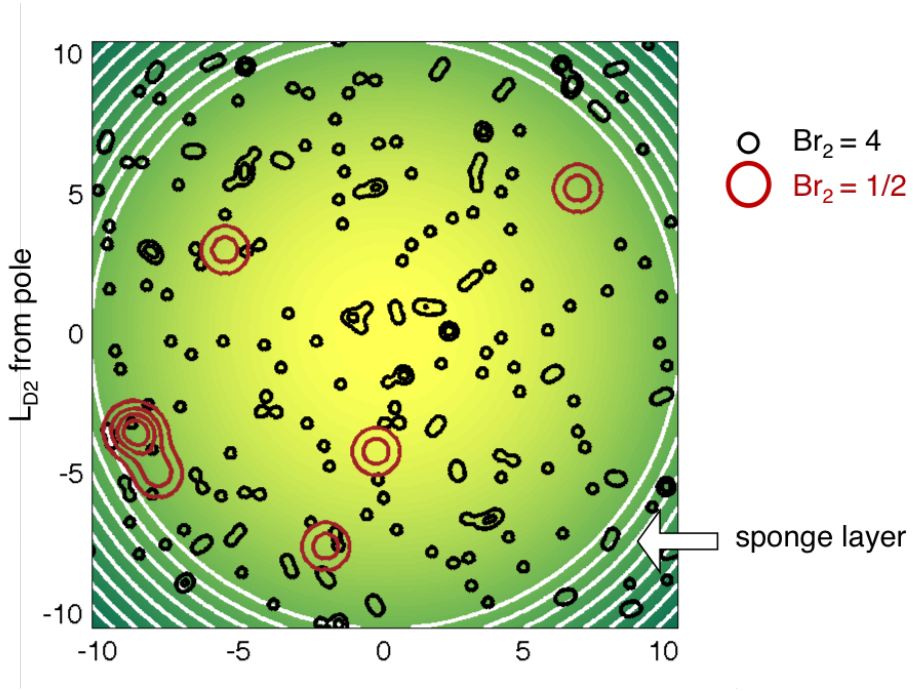

Figure 3-1: This is an example of the simulation geometry and forcing. The white contours show the sponge layer time scale decreasing infinity to a minimum value of 0.8 days at the corners of the domain. The black contours are storms for $\mathrm{Br}_2 = 4$ ($R_{st}/L_{D2} = 1/2$). The red contours are storms for $\mathrm{Br}_2 = 1/2$ ($R_{st}/L_{D2} = \sqrt{2}$). The storms are randomly placed, and sometimes occur within the sponge layer or in overlapping clusters.

11-dimension parameter space.

For most simulations we impose a resolution constraint on the second baroclinic deformation radius of $L_{D2} = 5dx$, in order to consistently resolve filamentation and enstrophy for a wavelength smaller than $1/L_{D2}$. As we discuss in chapter 5, the equilibrium behavior is found to be very insensitive to resolution - but the total system energy is not, and this is an important diagnostic quantity.

The model is highly dissipative, which is unfortunate but a necessary tradeoff for computational speed, given the enormous parameter space to explore. This may not strongly impact the dynamics however, because the radiative timescale is very short. Conrath et al. (1990) use a simple a model of the giant planet atmospheres and consider the frictional time constant as the independent parameter. They find that a frictional time constant is on the same order as the radiative time constant for the giant planets. Here it is one or two orders higher, which suggests that dissipation will not affect the outcome at equilibrium - provided the storm timescale remains much shorter than the radiative timescale.

The model does not inject spurious energy. All freely evolving runs, described in the next chapter, lose energy monotonically. Mass-weighted PV in each layer is conserved. Angular momentum is not conserved because the domain lacks azimuthal symmetry (the sponge layer is very different from a no-slip boundary); linear momentum is not conserved due to the sponge layer.

Domain size

Two difficulties arise when one compares a normalized nondimensional shallow water model to a real fluid:

- the shallow water approximations preclude unique determination of the layer heights upon re-dimensionalization, because they are coupled with the reduced gravities; and
- the second deformation radius, which normalizes horizontal length scales in the model, is not actually constant but radially dependent.

The shallow water approximation is $H << L$, so the system uncouples height variables from length variables. In the nondimensionalization, there is no parameter group that relates strictly a vertical scale to a horizontal scale, and the nondimensional parameters can be considered two uncoupled groups. The length scale L_{D2} is a ratio between the second baroclinic gravity wave speed c_{e2}, which is a function of the second baroclinic effective depth h_{e2}, and the rotation rate. However, h_{e2} can co-vary with the reduced gravity for a given L_{D2}. Therefore the shallow water approximation cannot provide a unique set of dimensional layer thicknesses upon choosing values for the scales, and a value for gravitational acceleration g must be chosen in addition. One can avoid thinking about the layer thicknesses independently of gravity, if the mass continuity equations are multiplied by g, yielding a geopotential gh (S07 does this for his 1 $\frac{1}{2}$ shallow water model). Alternatively, Saturn's surface gravitational acceleration is known, so it can be used to solve for the corresponding layer thickness in the dimensional case. This latter option is appealing when trying to evaluate whether control parameters are relevant to Saturn and other giant planets. Gravitational acceleration and atmospheric scale heights are assessed independently and with different techniques, and the gravitational acceleration measurement is highly accurate.

The second difficulty concerns the accuracy of L_{D2} for different angular extents of the domain. The actual deformation radius is a function of latitude (in our case, radius from the pole); it is minimized at the poles and approaches infinity at the equator (undefined). The implications of setting $L_{D2} =$ const. and then normalizing model lengths by L_{D2} are discussed in detail in the appendix of this chapter.

We are tightly constrained in the parameter space we can physically simulate by two decisions: using a polar beta plane instead of a spherical variation of the Coriolis parameter, which limits the validity of large domains; and setting the resolution of L_{D2} to a constant value across (most of) the simulations, such that they can be directly compared. Fortunately, we are not limited to simulating a particular type of planet. The limitations only apply to how far we can deviate once we choose a set of dimensional parameters to emulate. Because the highest quantity and quality of polar

observations come from Cassini's imaging of Saturn, we choose to benchmark scales such that we can simulate a range of planets in the neighborhood of Saturn-specific parameters. This is a good choice for comparison to Jupiter, because the gas giants' global $\beta = \Omega/a$ is nearly the same.

An observational estimate for Saturn's first deformation radius in the polar region is 1000-1500 km (Read et al., 2009), or around one-tenth the distance to the first proper jet. If we consider a wider possible range, 500-2000 km, we can choose a domain size such that each of these possibilities can be modeled in a sufficiently large domain. If Saturn's L_{D2} is $\approx$ 500 km, Saturn has a low $\tilde{\beta}$, and thus a large $a/L_{D2} = 110$. If L_{D2} is $\approx$ 2000 km, $\tilde{\beta}$ is high and $a/L_{D2} = 28$. A potentially important drawback of comparing results to observed deformation radii is that the observations likely measure a first baroclinic deformation radius, though without *in situ* measurements it is hard to know for sure; we choose the second baroclinic radius for our normalized length scale (it is the mode of dipolar moist convection, and intentionally resolved consistently). The implication of this is discussed in Chapter 6.

Accordingly, we set a benchmark domain size $L_{dom}^2 = a^2$, and the radial extent for most simulations is $a/2$, or about 30° from the pole. The polar beta plane is a very good approximation over this entire domain. On a large-$\tilde{\beta}$ Saturn, the distance from the pole to 30° colatitude is only spanned by seven deformation radii. On a small-$\tilde{\beta}$ Saturn this jumps to 26 deformation radii. Both possibilities can be modeled in tractable domains for a constant resolution of L_{D2}.

The difficulty arises when considering the ice giants Uranus and Neptune, because their deformation radius is estimated to be up to 1/3 of their planetary radius (Polvani et al., 1990). Most simulations in this work resolve L_{D2} by 5 grid points. If we tried to simulate a planet with $a/L_{D2} = 3$, the limit of polar beta plane validity would be reached within those 5 grid points - certainly an absurd proposition. Yet given the results in the following chapters, which demonstrate the importance of total energy in a given simulation, the choice to vary resolution as L_{D2}/a changes begins to sound nearly as terrible, because high but numerically necessary viscosity and diffusion act

most strongly at the model grid scale. This work focuses on Saturn-like planets but is able to infer ice giant-type behavior in certain parameter spaces.

3.5 Energy equations

To derive nondimensional energy equations for this system, we multiply the upper layer momentum equation by $(\rho_1/\rho_2)(H_1/H_2)h_1\vec{u}_1$, and the lower layer momentum equation by $h_2\vec{u_2}$. Likewise, the upper mass conservation equation is multiplied by $1/2(\rho_1/\rho_2)(H_1/H_2)|\vec{u}_1|^2$; and the lower, by $1/2|\vec{u}_2|^2$.

Expressions for layer kinetic and potential energy conservation are, respectively:

$$\frac{\partial K_1}{\partial t} = -\nabla\cdot\left(h_1\vec{u}_1\frac{1}{2}\frac{\rho_1}{\rho_2}\frac{H_1}{H_2}|\vec{u}_1|^2\right) + \vec{u}_1h_1\cdot\nabla\left(\frac{1}{2}\frac{\rho_1}{\rho_2}\frac{H_1}{H_2}|\vec{u}_1|^2\right) - \frac{\rho_1}{\rho_2}\frac{H_1}{H_2}h_1\vec{u}_1\mathrm{Re}^{-1}\nabla^4\vec{u}_1 \tag{3.22}$$

$$\frac{\partial K_2}{\partial t} = -\nabla\cdot\left(h_2\vec{u}_2\frac{1}{2}|\vec{u}_2|^2\right) + \vec{u}_2h_2\cdot\nabla\left(\frac{1}{2}|\vec{u}_2|^2\right) - h_2\vec{u}_2\mathrm{Re}^{-1}\nabla^4\vec{u}_2 \tag{3.23}$$

$$\begin{aligned}\frac{\partial P_1}{\partial t} =& -\nabla\cdot\left(h_1\vec{u}_1\frac{\rho_1}{\rho_2}\frac{H_1}{H_2}(\tilde{c}_1^2h_1+\tilde{c}_2^2h_2)\right) - \vec{u}_1h_1\cdot\nabla\left(\frac{1}{2}\frac{\rho_1}{\rho_2}\frac{H_1}{H_2}|\vec{u}_1|^2\right)\\ &+\frac{1}{2}\frac{\rho_1}{\rho_2}\frac{H_1}{H_2}|\vec{u}_1|^2\left(S_{st}-\frac{h_1-1}{\tilde{\tau}_{rad}}+\mathrm{Pe}^{-1}\nabla^2h_1\right)\end{aligned} \tag{3.24}$$

$$\begin{aligned}\frac{\partial P_2}{\partial t} =& -\nabla\cdot\left(h_2\vec{u}_2(\gamma\tilde{c}_1^2h_1+\tilde{c}_2^2h_2)\right) - \vec{u}_2h_2\cdot\nabla\left(\frac{1}{2}|\vec{u}_2|^2\right)\\ &+\frac{1}{2}|\vec{u}_2|^2\left(\frac{H_1}{H_2}S_{st}-\frac{h_2-1}{\tilde{\tau}_{rad}}+\mathrm{Pe}^{-1}\nabla^2h_2\right)\end{aligned} \tag{3.25}$$

$$\tag{3.26}$$

where total kinetic energy K, total potential energy P (to some constant), and total available potential energy A equal, respectively:

$$K = \frac{1}{2}\left(\frac{\rho_1}{\rho_2}\frac{H_1}{H_2}h_1|\vec{u}_1|^2 + h_2|\vec{u}_2|^2\right) \tag{3.27}$$

$$P = \frac{1}{2}\frac{\rho_1}{\rho_2}\frac{H_1}{H_2}\tilde{c}_1^2 h_1^2 + \frac{1}{2}\tilde{c}_2^2 h_2^2 + \gamma\tilde{c}_1^2 h_1 h_2 \tag{3.28}$$

$$A = \frac{1}{2}\frac{\rho_1}{\rho_2}\frac{H_1}{H_2}\tilde{c}_1^2 h_1'^2 + \frac{1}{2}\tilde{c}_2^2 h_2'^2 + \gamma\tilde{c}_1^2 h_1' h_2' \tag{3.29}$$

It can be shown that while the final term on the r.h.s. of the expression for A is often negative, total A is always positive, as we expect.

3.6 Deriving an energy parameter

S07 derives an 'energy parameter', which scales as the equilibrated APE value. The expression for this parameter E_p, using this work's nondimensional numbers, is $\tilde{\tau}_{st}^2 \mathrm{Br}_2^{-1} \mathrm{Ro}_{conv}^2 \tilde{\tau}_{rad}/\tilde{\tau}_{stper}$. This is good scale for his 1 $\frac{1}{2}$ layer model. We generalize this parameter to our 2 $\frac{1}{2}$ layer model with variable stratification and layer thicknesses, for our particular constraint of instantaneous mass conservation in each layer. The importance of this parameter will be discussed in the following chapters.

The available potential energy induced by one storm, A_{st}, affects the entire domain due to mass-conserving subsidence outside of the storm environment. To find a scaling for A_{st}, we first look at the modified height fields in each layer. The top layer experiences an increase in thickness, Δh_{1st}, within the boundaries of the storm; and the rest of the domain experiences constant subsidence, Δh_{1sub}. The thickness perturbation due to one storm, over the area of the storm, scales as:

$$\Delta h_{1st} = \mathrm{Ro}_{conv}\tilde{\tau}_{st} \tag{3.30}$$

$$\Delta h_{2st} = -\frac{H_1}{H_2}\Delta h_{1st} \tag{3.31}$$

The areal fraction covered by 1 or N storms, A_r, is a function of # and the Burger number:

$$A_r = \frac{\#\pi}{\mathrm{Br}_2 L_{dom}^2} \tag{3.32}$$

This expression neglects the Gaussian shape of the storms and instead assumes cylinders or 'top hats' with a radius equal to the location of FWHM of the vortex (the radius of vortex corresponding to its Full-Width at Half-Max amplitude of the vortex). This approximation should introduce a negligible error in the energy scale. An additional source or sink of APE comes from the subsiding regions in the rest of the domain: $(1 - A_r)$. The domain-wide storm forcing and subsidence are not necessarily a source of APE at any given instant. APE is only increased where Δh_i is the same sign as h_i'. It is necessary to include the APE contribution of the subsiding regions to find a parameter for the entire APE of the domain.

Due to layer mass conservation, imposed at every time step, the total volume of the storm forcing is always equal to the total volume of the subsidence elsewhere in the domain. We can relate a perturbation thickness due to subsidence to the perturbation thickness due to storms:

$$\Delta h_{i,sub} = -\frac{A_r}{1 - A_r} \Delta h_{i,st}. \tag{3.33}$$

To find a scale A_{sc} for the APE of the entire domain, we consider the contributions from both the storm and subsidence regions, using the above substitutions to express each height in terms of $\Delta h_{1,st}$:

$$\int_{storm} A_{sc} \mathrm{d}A_r = A_r \left(\frac{1}{2} \frac{\rho_1}{\rho_2} \frac{H_1}{H_2} \tilde{c}_1^2 \Delta h_{1,st}^2 + \frac{1}{2} \tilde{c}_2^2 \left(\frac{H_1}{H_2} \right)^2 \Delta h_{1,st}^2 - \gamma \tilde{c}_1^2 \frac{H_1}{H_2} \Delta h_{1,st}^2 \right) \tag{3.34}$$

$$\int_{sub} A_{sc} \mathrm{d}(1 - A_r) = (1 - A_r) \left(\frac{1}{2} \frac{\rho_1}{\rho_2} \frac{H_1}{H_2} \tilde{c}_1^2 \left(\frac{A_r}{A_r - 1} \right)^2 \Delta h_{1,st}^2 + \right. \tag{3.35}$$

$$\left. \frac{1}{2} \tilde{c}_2^2 \left(\frac{H_1}{H_2} \right)^2 \left(\frac{A_r}{A_r - 1} \right)^2 \Delta h_{1,st}^2 - \left(\frac{A_r}{A_r - 1} \right)^2 \gamma \tilde{c}_1^2 \frac{H_1}{H_2} \Delta h_{1,st}^2 \right) \tag{3.36}$$

Summing these contributions yields A_{sc} as a function of our scaled Δh_{1st} and other nondimensional parameters:

$$A_{sc} = \left(\frac{1}{2}\frac{\rho_1}{\rho_2}\tilde{c}_1^2 + \frac{1}{2}\frac{H_1}{H_2}\tilde{c}_2^2 + \gamma\tilde{c}_1^2\right)\frac{H_1}{H_2}\left(\mathrm{Ro}_{conv}\tilde{\tau}_{st}\right)^2\left(\frac{A_r}{1-A_r}\right) \tag{3.37}$$

The first factor on the right hand side of equation 3.37 *should* have a negative $\gamma\tilde{c}_1^2$, even though this term is positive in equation 3.27, because storm forcing always induces opposite perturbations in the top and bottom layers, while in general (equivalent) barotropic structures can experience same-signed perturbations. However, one of the consequences of a beta plane, whether quadratic or linear, is to promote barotropization (Venaille et al., 2012). In the long time average of the following simulations, some polar flows can become primarily barotropic, and so $h_1'h_2'$ is often positive. Since we are interested in equilibrium behavior, we choose to retain the positive sign in front of the $\gamma\tilde{c}_1^2$ term, and show in the following chapters that this is empirically a much better scale for total energy.

Following the derivation of a total 'energy parameter' E_p in S07, A_{sc} is modified by two time scales. A longer radiative timescale will remove energy more slowly; and a longer period between storms will add energy more slowly. Thus our energy scale $E_p = A_{sc}\tilde{\tau}_{rad}/\tilde{\tau}_{tsp}$. It is entirely composed of control parameters. This parameter should scale with the total equilibrated potential energy per deformation radius area L_{D2}^2 of each simulation.

The energy parameter derived here is not a function of the hyperviscosity or diffusion parameters, though in reality the model's high dissipation means they must impact the dynamics to some extent. However, our choice of fixing viscosity across the models, and consistently resolving L_{D2} allows us to largely ignore this issue, since the impact should then be uniform among the simulations.

3.7 Conclusion

This model is unique and provides a number of advantages over previous models for the challenge of understanding polar flows. Motivated by abundant observations of intense moist convection on the gas giants, we have constructed a model that is much less restricted in its assumptions and geometry than previous works examining polar behavior, which allows us to examine a broader parameter space.

3.8 Appendix

Understanding the radial dependence of E_p

While E_p should not contain any function of the planetary vorticity gradient $\tilde{\beta}$, it does, and we must account for this when seeking an E_p that accurately scales as the total energy. We scaled our model equations by L_{D2}, which we fixed as constant. However, on a planet or polar beta-plane, this is not the case, as $f = f_0 \sin(\theta)$ in the spherical case and $f = f_0 - \tilde{\beta} r^2$ in our polar beta plane configuration. This variation is studied carefully by Theiss (2004). The deformation radius L_{D2} is actually a function of $\tilde{\beta}$ and distance from the pole r:

$$L_{D2}(r) = \frac{c_{e2}}{f_0 - \tilde{\beta} r^2}. \tag{3.38}$$

To understand what this means physically, recall that E_p is a scale for APE only. The radial considerations only take into account the scaling for potential energy. If we inject a storm with $\mathrm{Br}_2 = 1$ near the edge of the domain on a small planet, its actual, radially dependent Br_2 will be larger, because the real L_{D2} will be larger than 1. The storm motions then will be more 2D-like than the E_p scale suggests, causing more energy to be in kinetic rather than potential form. E_p will underestimate the total energy in such cases.

The radially-dependent L_{D2}, which is a scale in the Burger number Br_2 and

therefore areal storm fraction A_r, leads to the following radial dependence of E_p (recall that we have set $L_{D2} = c_{e2} = f_0 = 1$):

$$E_p \propto \frac{A_r(\tilde{\beta}r^2)}{1 - A_r(\tilde{\beta}r^2)} \tag{3.39}$$

$$= \frac{\frac{\#\pi R_{st}^2}{L_{dom}^2}(1 - \tilde{\beta}r^2)^2}{1 - \frac{\#\pi R_{st}^2}{L_{dom}^2}(1 - \tilde{\beta}r^2)^2} \tag{3.40}$$

The denominator $1 - Ar$ is entirely due to our choice of compensating subsidence during storms. The parameter $\tilde{\beta}$ is always much less than 1 (though this isn't true for the much smaller ice giants!). We can see that we have a candidate for a Taylor expansion in small x, which would make life easier. Is it appropriate? As explained in section 3.4.1, the outer radial limit of the domain is usually $a/2$. Equation 3.39 can be solved at $r_{max} = a/2$ to demonstrate the impact of variable L_{D2}.

$$E_p(r_{max}) \propto \frac{\frac{\#\pi R_{st}^2}{a^2}\left(1 - \frac{1}{2a^2}\left(\frac{a}{2}\right)^2\right)^2}{1 - \frac{\#\pi R_{st}^2}{a^2}\left(1 - \frac{1}{2a^2}\left(\frac{a}{2}\right)^2\right)^2} \tag{3.41}$$

The planetary radius cancels in the wide brackets, leaving a factor of $(1 - 1/8)^2 = 0.76$. We are left with

$$E_p(r_{max}) \propto \frac{0.76\#\pi\frac{R_{st}^2}{a^2}}{1 - 0.76\#\pi\frac{R_{st}^2}{a^2}} \tag{3.42}$$

The factor of 0.76 is due to our choice of $L_{dom} = a$, and reflects the squared fractional change of A_r due to the dependence of L_{D2} on r at the edge of the domain. A domain that simulates further equatorward would have a larger factor. The factor 0.76 would actually be 0.78 if we had been a little more precise. The area on a sphere encompassed by one steradian, or solid angle, is a^2. However here we cut corners by

adding corners to our domain, and so the no-sponge area of the domain is slightly smaller than L_{dom}^2.

Finally we reach the key point of this tedium: Adding the impact of subsidence on APE is increasingly important for smaller planets and/or larger areal storm coverage. This is because we fix the angular size of the domain as a function of a, but $\tilde{\beta} \propto a^{-2}$. For a very large planet and small storm coverage, a^2 dwarfs the numerator in equation 3.42. In this case, the complete energy parameter is essentially the same as it would be having only integrated over the storm forcing area. However, as that area grows, OR as the planet shrinks, the contribution from the subsiding areas becomes increasingly important. For these reasons, the constant value E_p is more rapidly wrong with radius for larger $\tilde{\beta}$ or larger areal forcing, even after controlling for angular size of the domain.

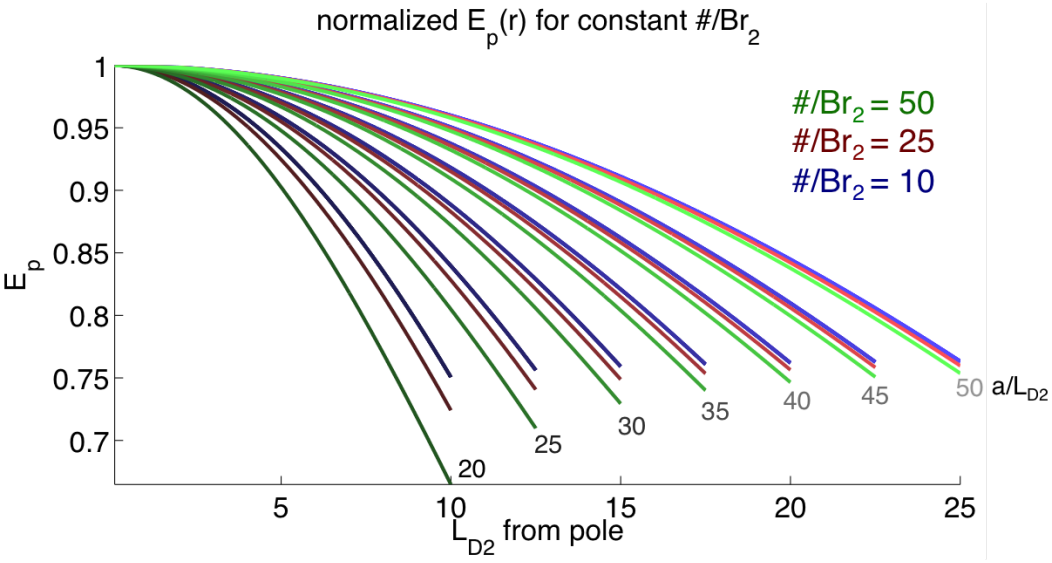

Figure 3-2: Planets with larger $\tilde{\beta}$ are represented by darker shades, and the colors represent the magnitude of the storm forcing. Recall that $\#/\mathrm{Br}_2$ is proportional to $\#R_{st}^2$.

Figure 3.8 illustrates how different forcing areas $\#/\mathrm{Br}_2$ affect different planets' $E_p(r)$. Large $\tilde{\beta}$ planets always have a larger discrepancy in E_p at the domain limit, and this error is greater for larger storm coverage. In Figure 3-3, this is corrected by simply fixing the *fractional* storm coverage A_r such that each $\tilde{\beta}$ equally suffers

from the discrepancy in constant E_p. Of course, we're interested in how A_r changes the equilibrium flow. In S07, the areal coverage of storms is considered small and the corresponding term is tossed. We keep it here in order to allow a wider range of storm forcing areal fractions, with the understanding that moist convective towers should take up only a very small fraction of the weather layer area.

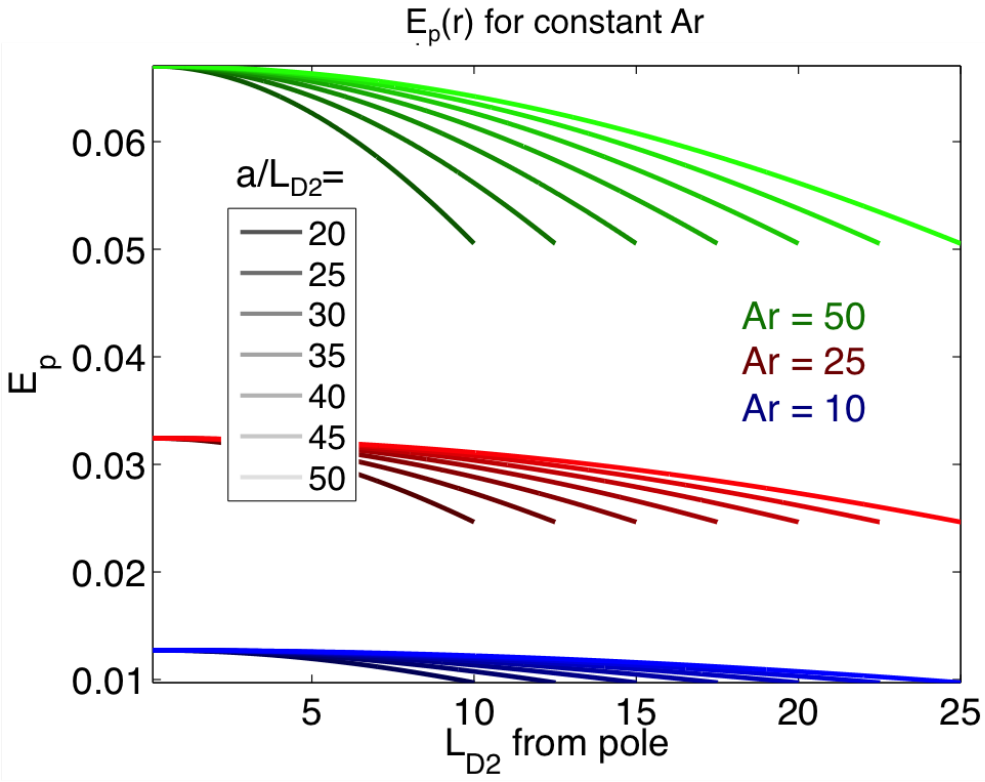

Figure 3-3: Planets with larger $\tilde{\beta}$ are represented by darker shades, and the colors represent the magnitude of the storm forcing.

Chapter 4

Unforced experiments

4.1 Introduction

Planetary Rossby waves play a significant role in shallow atmospheric dynamics. Rossby waves require a gradient in potential vorticity to act as a restoring force, and their behavior is decidedly anisotropic: they always propagate to the left of a positive potential vorticity gradient. On the planets this gradient is permanently provided by the Coriolis gradient on the rotating sphere. Other sources of such a gradient are ocean bathymetry and land topography, which induce fluid column stretching and shrinking and can also excite Rossby waves, and temperature gradients on boundaries.

A small positive vorticity anomaly on a beta plane ($\beta > 0$) will induce a westward-propagating Rossby wave, by advecting low-vorticity air to its east northward, and high vorticity air to its west southward. These disturbed air parcels must conserve potential vorticity, so they each compensate by spinning down relative vorticity (in the case of the air that has moved northward) or by spinning up (for air that has moved southward). The planetary vorticity, acting as a restoring force, propagates the anomaly westward (and meridionally if the meridional wavenumber is nonzero). This is a linear Rossby wave. Flierl (1977) proposes and Chan and Williams (1987) finds that a vortex on a beta plane in the linear nondivergent barotropic system is dispersed, or stretched westward, because the outer regions of the vortex have a smaller associated wavenumber and therefore a faster phase speed.

Meridional propagation is essential to our proposed polar cyclone mechanism. Closer to home, tropical cyclones are an extremely nonlinear phenomenon, with a well known tendency to propagate westward and poleward. To understand this meridional motion, we turn to nonlinear dynamics.

Beta drift

The terrestrial meteorology community has spent a great deal of effort to understand the motion of tropical cyclones, since Farrar (1819) first hypothesized that a tropical cyclone was a "moving vortex". Since then scientists have converged on an explanation for the familiar southeast-to-northwest motion of tropical cyclones (in the northern hemisphere). It is called the 'beta effect', or 'beta drift', because $\beta \neq 0$, which is most generally any gradient of potential vorticity, is necessary (Chan, 1982). The explanation of the dynamics of a Rossby wave is modified for strong vortices and nonlinear terms. The magnitude of the vorticity anomaly must be so great that the counterrotating eddies it creates are rather substantial themselves. Then, the secondary eddies will induce matching meridional components of flow through the center of the original vortex (e.g. Adem 1956, Chan and Williams 1987). These secondary eddies are called 'beta gyres', and they impel the original vortex poleward if it is cyclonic and equatorward if it is anticyclonic. There is a zonal component too. Both positive and negative primary vortices will tend to move westward, and then meridionally as appropriate.

Meridional drift speeds are different in systems allowing cyclone/anticyclone asymmetry. This is due to the larger deformation radius experienced by the relatively thicker anticyclone (Polvani et al., 1994). Practically, McDonald (1998) speculates that the abundance of anticyclones observed in the ocean is due to their zonal drift speed, which is larger than the Rossby wave speeds - whereas cyclones' slow drift speed allows Rossby wave radiation to interfere and eventually disperse the vortex. Vortices can expect to lose energy to wave radiation if their drift speed u is within the Rossby phase speed range. In our case this implies $-2\tilde{\beta}rL_{D1}^2 < u < 0$ for the gravest waves.

Coherent vortices don't necessarily drift meridionally, even if they are strong. One class of vortex pairs, the modon, does not move meridionally. A barotropic modon (Stern 1975, Larichev and Reznik 1976) is a horizontal, strongly nonlinear cyclone/anticyclone pair on a beta plane, with zero net angular momentum. Modons are stationary on a beta plane because the beta drift effect is exactly cancelled by the local beta effect of one vortex on the other[1]. A modon can maintain a circular shape and zonal motion in the presence of waves (though they too eventually lose energy to Rossby wave radiation - see Flierl and Haines 1994), and propagate east or west. The original barotropic solution has been extended to baroclinic fluids (Flierl et al., 1980) and spheres (Verkley, 1984). Westward-propagating modons may be the dominant vortex feature responsible for atmospheric blocking on Earth (McWilliams, 1980), and are also observed in our forced-dissipative runs in the next chapter.

4.2 Experiments

The experiments in this chapter pertain to unforced flows, wherein one or several storms are initially forced and then allowed to decay (there is no radiative relaxation). The background state has zero mean flow, for both these experiments and the forced dissipative set in the following chapter. For these decaying experiments in particular, a zero background flow allows us to isolate the nonlinear dynamics due to the vortex only, as in Chan and Williams (1987).

These features decay more quickly than they would in any nearly-inviscid atmosphere, but slowly enough to observe the nonlinear interaction with the planetary vorticity gradient.

We label the unforced experiments in the following way:

- `Xbtrop`: single barotropic vortices (1-layer configuration), placed off the pole.
- `Xbclin`: single baroclinic vortices, placed off the pole.

[1]This is not the case on a polar beta plane, as demonstrated by Nof (1990). On a polar beta plane, the relative strengths of the vortices comprising the dipole must be different in order to keep the pair stationary. The same follows for a sphere.

Parameter	Values	Parameter	Values
$\tilde{c}_1^2$	7	Re	5e6
$\tilde{c}_2^2$	7	Pe	1e6
$\frac{H_1}{H_2}$	1	$t_{\max}$	2000
a/L_{D2}	30	dx	1/8
$\frac{\rho_1}{\rho_2}$	1	dt	2^{-8}
$\tilde{\tau}_{st}$	6		
Br_2	0.1; 0.25; 0.5; 0.75; 1; 1.25; 1.5; 2; 4		
Ro_{conv}	$\pm 0.02\mathrm{Br}_2$; $\sqrt{0.0016\mathrm{Br}_2}$		

Table 4.1: Values for experiments `Xbtrop`. The ($\pm$) in front of the first Ro_{conv} range indicates that those experiments were run as both barotropic cyclones and anticyclones.

- `Xmult`: multiple baroclinic vortices, placed in pairs surrounding the pole.

4.2.1 `Xbtrop`

We first run a series of experiments in the 1-layer version of the model ($\rho_1/\rho_2 = \tilde{c}_2^2/\tilde{c}_1^2 = 1$). Aside from demonstrating expected behavior, which builds confidence in the model, these simulations also explore the meridional drift of barotropic vortices. Simulations vary Br_2 while holding one of either two quantities fixed: storm volume, $\propto \mathrm{Ro}_{conv}/\mathrm{Br}_2$, or the energy parameter $E_p \propto \mathrm{Ro}_{conv}^2/\mathrm{Br}_2$. Each simulation only fires one storm initially, $7.9L_{D2}$ from the pole, and allows it to evolve. The planet in all cases is has a medium value of $\tilde{\beta}$, where $a/L_{D2} = 30$. Model parameters are listed in Table 4.1.

We will refer to the first set of barotropic experiments as $\texttt{Xbtrop}_{RB}$. The forcing function conserves storm volume across the range of Burger numbers explored. Figure 4-1 illustrates the evolution of a weak barotropic cyclone (top row) and anticyclone (bottom).

The contours mark the quantity $q' = q - f(r)/H$. This quantity is not materially conserved, but it allows us to see PV perturbations due to Rossby waves clearly. Gravity wave interaction is evident in early time steps, because the vortices are ini-

tially unbalanced and the sponge layer is slow to absorb gravity waves. However, the forcing is slow so the waves are very low magnitude, and the domain is dominated by vortical behavior.

The vortices are symmetric at Day 0, immediately after the forcing. By Day 2, Rossby wave radiation can already be seen in the smearing and stretching of the vortex westward. If the vortices were strong enough, the beta gyres would advect the vortex meridionally. In this case, the vortices are too weak to create significant gyres, and so they evanesce into low-amplitude Rossby waves, which propagate away while dissipating due to viscosity and diffusion. More intense cyclones (higher Ro_{conv} and lower Br_2 in this set of experiments) experience less radiation, maintain a coherent circular shape for longer, and exhibit significant meridional drift.

The other barotropic experiments $\texttt{Xbtrop}_{E_p}$ are initialized with more intense vortices. The Burger number is varied widely, and varies inversely with the square of Ro_{conv}, such that the energy parameter E_p is constant. The two extreme cases, $\mathrm{Br}_2 = 0.1$ and $\mathrm{Br}_2 = 4$, are illustrated in Figure 4-2.

Both cyclones are very intense, and nonlinear advection wraps each vortex with PV of the opposite sign, slowing its meridional motion. However, the cyclones still move appreciably poleward, with PV greater than the local background PV for the duration of the integration. A Rossby wave train can also be seen in each simulation.

The $\mathrm{Br}_2 = 0.1$ simulation fully occupies the pole by the end of the short integration. Both cyclones are much stronger than the planetary vorticity, so their size is the distinguishing trait that governs their drift. The larger vortex feels a significantly larger Δf within its boundaries, and it is able to perturb fluid from a wider latitudinal range. These beta gyres begin advecting the vortex poleward. In both cases, the vortex is wrapped by fluid with lower perturbation PV, but in the case of the larger storm, this is insufficient to arrest its drift.

Using the same perturbation PV, $q' = q - f(r)/H$, as a tool to follow each vortex, we examine the zonal and meridional drift of experiments $\texttt{Xbtrop}_{RB}$ and $\texttt{Xbtrop}_{E_p}$. Figure 4-3 is a parametric plot with the origin of the initialized vortex in the upper right corner, and shows the vortex path while it remains the strongest PV anomaly in

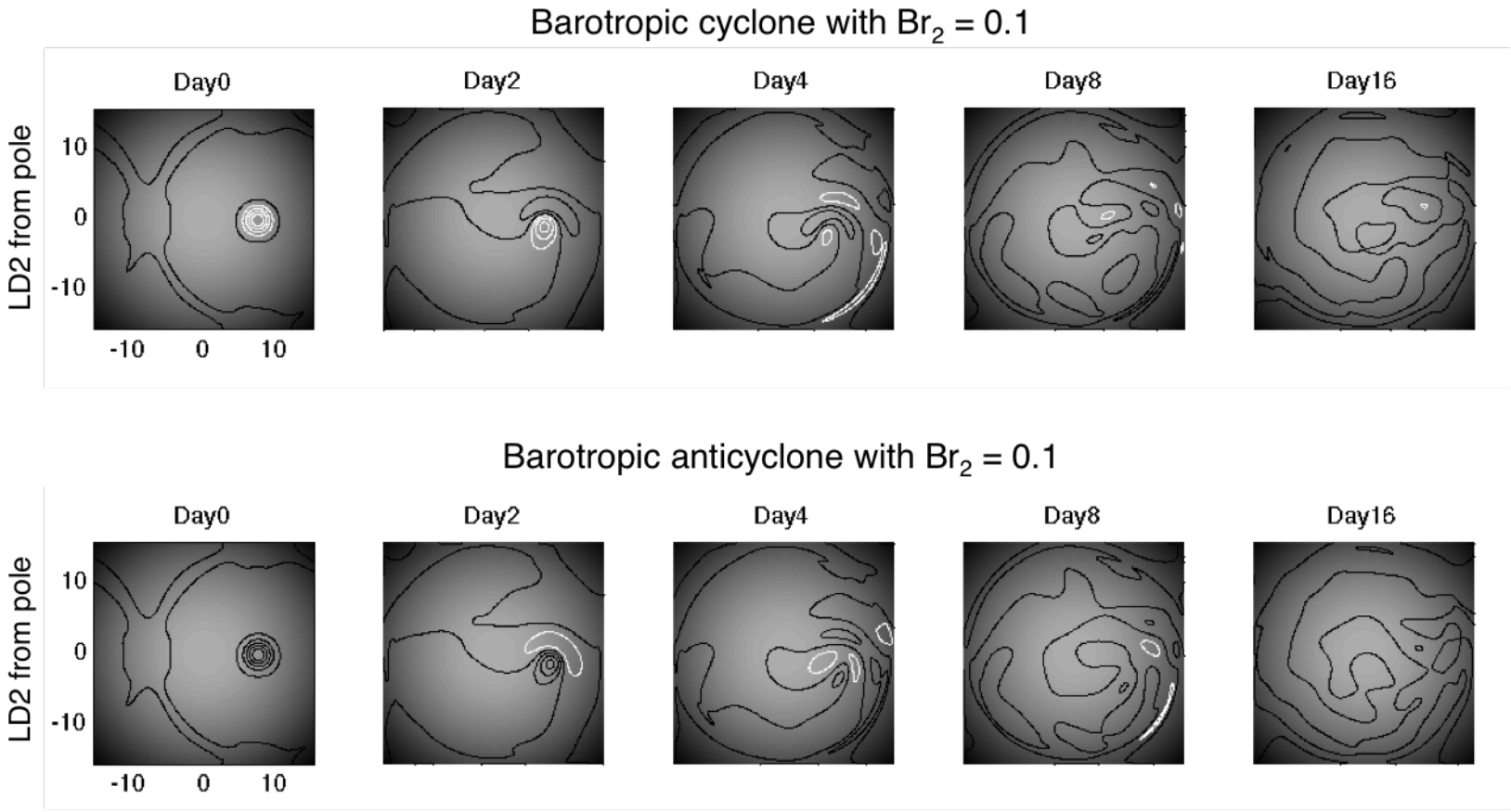

Figure 4-1: Barotropic cyclone (top row) and anticyclone (bottom row) evolution for $\mathrm{Br}_2 = 0.1$ in $\texttt{Xbtrop}_{RB}$.White contours are positive q', negative contours are negative q'; contour interval is 2e-3. Background greyscale is initial planetary PV, $f(r)/H$.

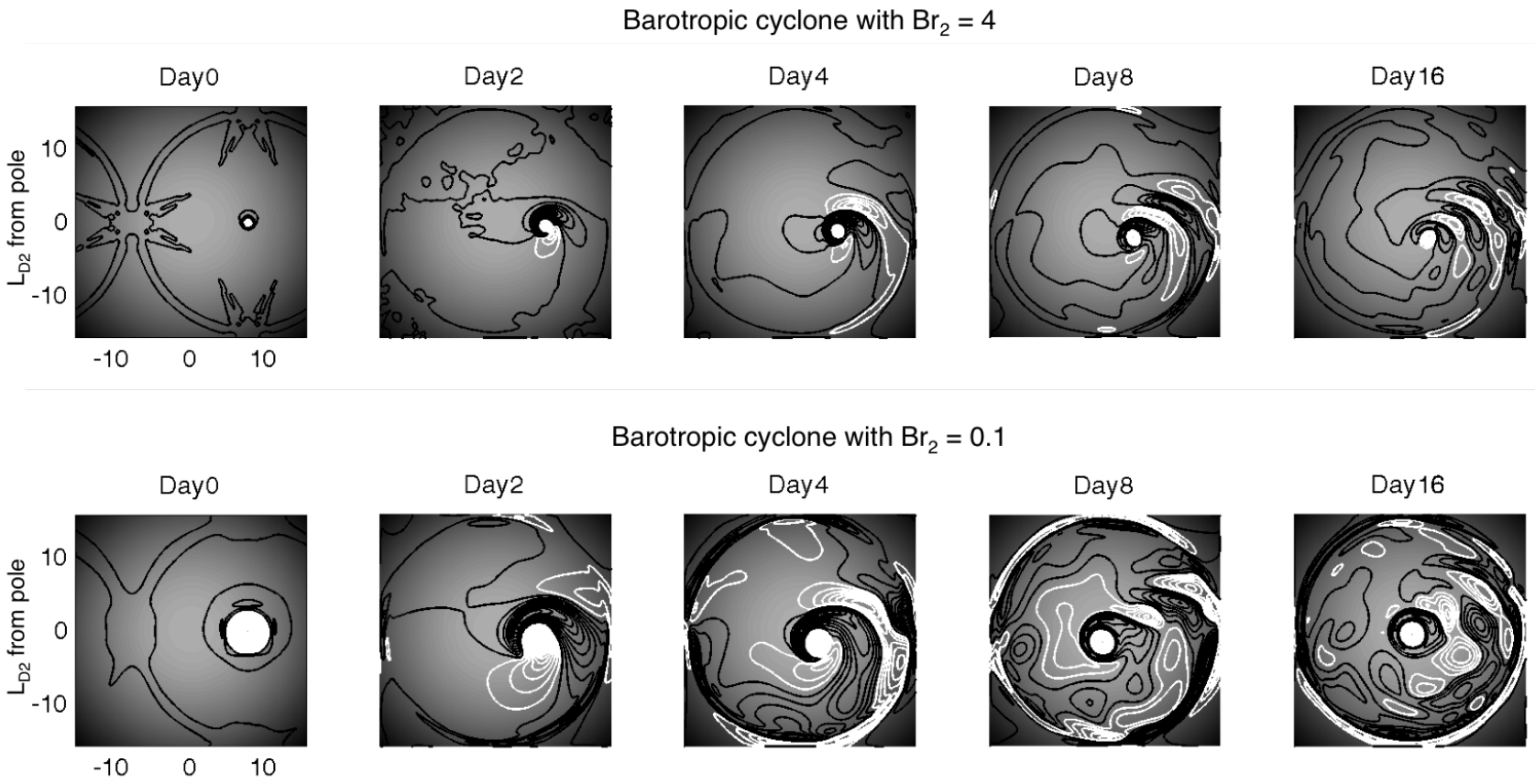

Figure 4-2: Example of beta drift with time for different Br_2 in $\texttt{Xbtrop}_{E_p}$. Contours are the same as Figure 4-1.

the domain, for $\texttt{Xbtrop}_{RB}$ cyclones. The strongest vortex with $\mathrm{Br}_2 = 4$ is able to travel nearly 4.5 L_{D2} poleward, and would likely reach the pole but for the short integration time. The weakest vortex moves only 1 L_{D2} poleward before it loses coherence and becomes primarily wavelike. All of the simulations exhibit a combination of beta drift poleward and westward propagation. The abrupt slowing of the meridional motion around $\theta = 345°$ is due to the nonlinear wrapping of the vortex in lower-PV fluid.

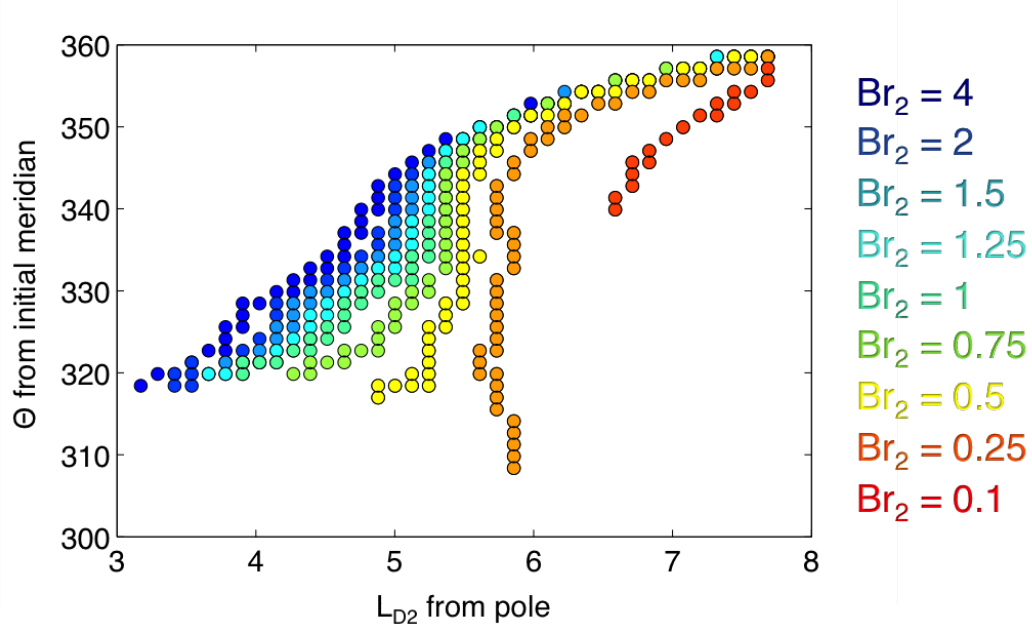

Figure 4-3: A parametric plot for the location of the maximum q' for $\texttt{Xbtrop}_{RB}$. The y-axis shows the angle that the cyclone has propagated longitudinally (westward) from its original position. The weakest, largest storm projects the most upon Rossby wave speeds, and moves the least poleward before losing its coherence and propagating westward. The strongest, smallest storm moves poleward for the length of the simulation.

Figure 4-4 shows the radial motion of the initial cyclone with time for a wide range of Br_2, and the corresponding maximum perturbation PV of the cyclone, for the $\texttt{Xbtrop}_{E_p}$ experiments. Now that E_p is fixed, the end result is nearly the opposite of $\texttt{Xbtrop}_{RB}$, in that the experiment with the largest Burger number makes it farthest to the pole, even though its intensity is the weakest. This large cyclone is able to maintain the largest fraction of its peak intensity. The $\mathrm{Br}_2 = 0.1$ experiment also exhibits the largest meridional drift arrest, after it has traveled to 2.5 L_{D2} from the

pole. This is due to the significant anticyclonic partner that accumulates to cyclone's northeast during propagation. As the cyclone continues to move poleward, it fully advects this anticyclonic fluid around itself. The area of closed isolines also shrinks as the vortex propagates, as first noticed by Flierl and Haines (1994).

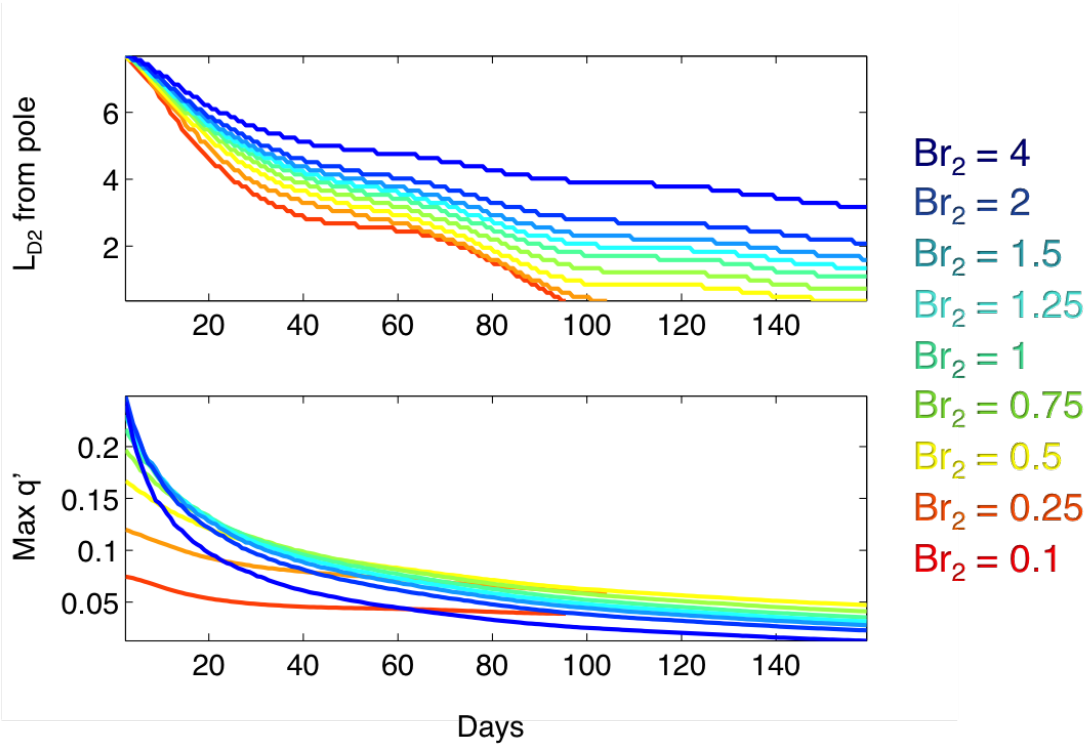

Figure 4-4: $\texttt{Xbtrop}_{E_p}$ for a range of Br_2. Each cyclone initially starts nearly $8L_{D2}$ from the pole, and propagates northwestward. The most intense cyclone is the smallest and moves the least poleward, as it rapidly loses its intensity.

This behavior is observed on a beta plane by Sutyrin et al. (1994) (see their Figure 1). They find that the advection and wrap-around of an annulus of opposite-signed PV is a common feature among strong monopolar cyclones. The cyclones may then deform into an ellipse due to instability, which causes the anticyclonic annulus to condense into two smaller vortices, creating an overall triple structure. It is possible that we don't observe this behavior because the distance to the pole is simply too short, and once the vortex reaches the pole the now-axisymmetric PV restoring force inhibits radial asymmetries. On the other hand, Sutyrin et al. (1994) find that vortices of intermediate strength become largely dipolar, due to a wrap-up of low-PV fluid on

one side of the vortex - more similar to the $\mathrm{Br}_2 = 4$ simulation.

The behavior of $\texttt{Xbtrop}_{E_p}$ experiments gives us confidence in the importance of the E_p parameter. These simulations are run with an L_{D2} resolution of $8dx$. The largest storm ($\mathrm{Br}_2 = 0.1$) is resolved by 50 grid points across its diameter. The smallest storm's diameter ($\mathrm{Br}_2 = 4$) is resolved by only 8 grid points. The model uses hyperviscosity to remove small scale *gradients* of velocity, and when E_p is held constant the smallest storms have the strongest velocity gradients, at the smallest scales. This explains the steep decrease in q' of the most intense cyclones in Figure 4-4.

4.2.2 `Xbclin`

The remainder of the experiments are run in the 2 layer configuration of the model, and all energy injection is purely baroclinic, which is more relevant to moist, statically stable atmospheres. For the present set of experiments, `Xbclin`, one single storm is initialized, with a local mass flux from the lower layer to the upper layer resulting in a lower cyclonic anomaly and an upper anticyclonic anomaly. It is forced for a short time and then allowed to freely evolve.

The need to predict tropical cyclone motion prompted numerous studies of baroclinic vortices on a beta plane. Tropical cyclones have intense cyclones in the lower atmosphere due to convergence in the boundary layer, and weaker, much broader anticyclones aloft. This structure is yet unobserved but a possibility for the SPV as well.

Wang and Holland (1996a,b) study adiabatic and diabatic baroclinic vortices on a beta plane using 3D primitive equations. Adiabatic baroclinic vortices are not maintained by low-level convergence, and so the upper level anticyclone quickly dissociates from the lower level cyclone and moves equatorward, as the cyclone moves poleward. Diabatic baroclinic vortices remain coupled because the forcing produces positive and negative PV anomalies at the same rate. Wang and Holland find that a lower level cyclone self-advects northwestward with the anticyclone above largely intact. Our vortices are briefly diabatic, and then are free to dissociate as adiabatic anomalies

when the forcing function stops transferring mass.

Independent of the tropical cyclone literature, Hogg and Stommel (1985a) identify and explore an idealized class of baroclinic point vortices they dub 'hetons', because they can uniquely advect heat. A heton is composed of either an upper layer anticyclone and a lower layer cyclone (a hot heton); or an upper layer cyclone and a lower layer anticyclone (a cold heton). The original formulation concerns only vortices on an f-plane. If the vortices are vertically aligned, they do not induce flow through the center of each other. However, if there is any horizontal displacement, or 'tilting', the pair now projects like-signed flow through each point vortex, and the pair becomes a 'shooter' - it moves forward in a straight line. Such motion is familiar for two opposite-signed vortices side by side in a single layer. The heton has one vortex in each layer, and in geostrophic balance each vortex deflects the interface of the two layers downward (in the case of the hot heton; upward for cold hetons), this pair can permanently displace the corresponding geopotential anomaly. Hetons have subsequently been used in two-layer models of ocean cooling (e.g. Hogg and Stommel 1985b, Legg and Marshall 1993, DiBattista and Majda 2000), often in the form of heton clouds that form clumps and transport heat. A thorough review of nonlinear heton dynamics is covered in Sokolovskiy and Verron (2013).

The evolution of a single baroclinic storm in our model can be seen in Figure 4-5, where the field shown is now the total layer PV. The lower layer (color) has a strong cyclone, and the upper layer (white contours) has a strong anticyclone. The baroclinic pair quickly splits. This pair had the potential to be heton-like, but the intra-layer advection was stronger than the vertical coupling. The upper anticyclone reaches the sponge layer and is reduced to waves, while the lower cyclone propagates northwestward.

As we saw in the barotropic experiments, strong nonlinear advection pulls low-PV fluid to the east and then north of the vortex, which inhibits direct poleward motion. The beta drift effect can apply equally to any gradient in vorticity or potential vorticity when nonlinear advection is permitted. This is dependent on the character of the perturbation. The vertical stretching parameter Ro_{conv} strongly affects the

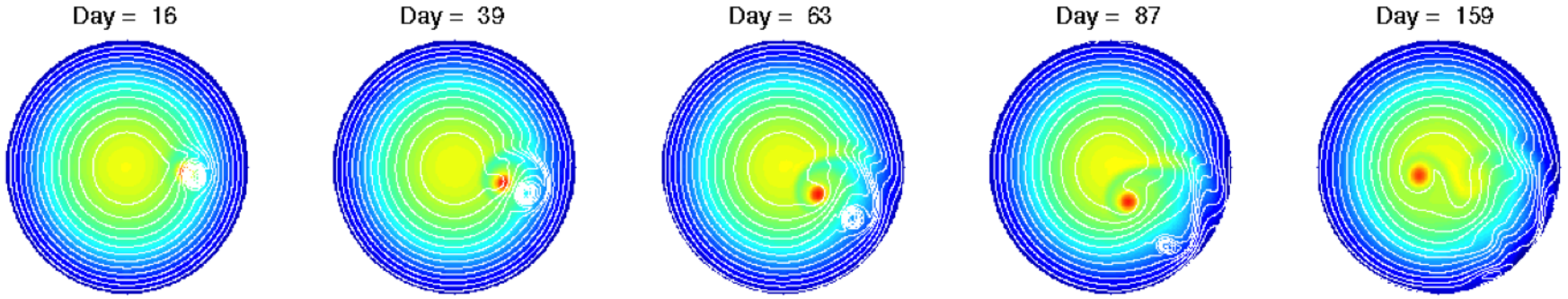

Figure 4-5: Example of beta drift with time for simulation `ix2`. The color gradient is the lower level total PV. The white contours are the upper level total PV. An initial baroclinic dipole separates vertically, and the anticyclone self-advects equatorward while the cyclone self-advects poleward.

strength of beta gyres as the fluid approaches geostrophic balance.

Figure 4-6 shows the impact of Ro_{conv} on three otherwise identical simulations. The field shown is azimuthally averaged q' of the lower layer, as a function of distance from the pole and time. The smallest vertical stretching $\mathrm{Ro}_{conv} = 0.01$ results in the weakest storm, which is only able to drift 1 L_{D2} poleward before it dissipates and evanesces as Rossby waves.

A stretching term four times as large (E_p is 16 times larger) induces sufficient nonlinear advection to propel the cyclone poleward for the duration of the simulation. This is a very nice example of the impact of the anticyclonic fluid advected ahead of the cyclone. The last image on the right of Figure 4-6, with a large Ro_{conv}, shows a cyclone that makes it all the way to the pole at the very last moment of integration. The azimuthal averaging makes the negative companion seem very strong, but it gets so intense only because when it reaches the pole it is no longer averaged with positive PV elsewhere in the domain.

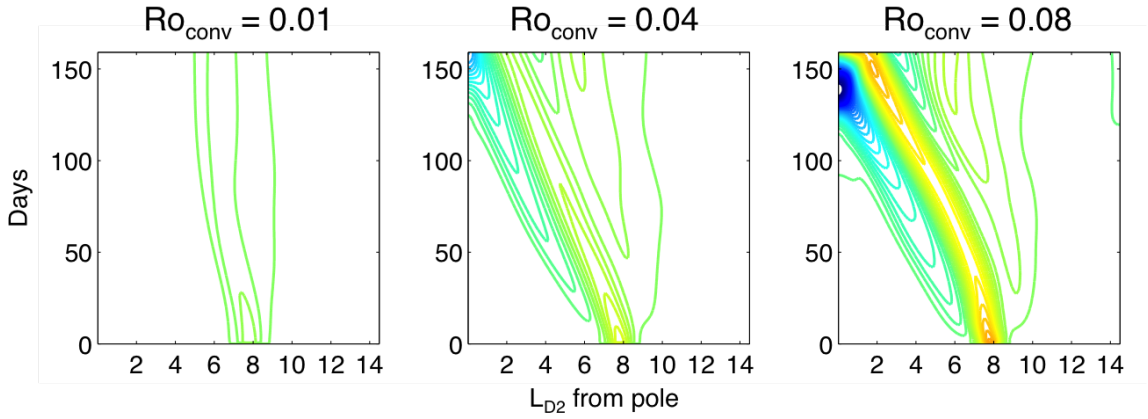

Figure 4-6: Beta drift of cyclone as a function of storm intensity Ro_{conv}. The perturbation PV $q' = q - f(r)/H$ of the lower layer is azimuthally averaged to omit the contribution of Rossby waves. The weak cyclone on the left has a contour interval of 5e-4 to show the very slight meridional drift; otherwise the interval is 1e-3, and across plots the extrema of q' are [-3e-2,3e-2].

We have so far observed the motion of barotropic vortices and lower layer cyclones. Close inspection of Figure 4-5 reveals that the upper layer is responding to the lower layer cyclone as well as the upper layer anticyclone. This is increasingly the case over

time, and is due to a process unique to geostrophic turbulence: barotropization.

Barotropization

Our 2 $\frac{1}{2}$ layer model permits both horizontal and vertical inverse cascades. The direction of the horizontal energy cascade of a fluid is a function of the vertical mode. An inviscid 2D fluid, with only a barotropic mode, experiences an inverse cascade to the largest scales (unless of course it is arrested by a Rhines scale first). A fluid with multiple modes will experience an inverse cascade through all scales only in the barotropic mode, and for each higher mode more of the horizontal energy will cascade to smaller scales, until it reaches an increasingly smaller deformation scale.

In the present model, two baroclinic modes support two deformation radii: an internal L_{D2} which we commonly consider the storm scale; and a larger external (equivalent-barotropic) L_{D1}. In each mode, these competing cascades lead to accumulation of energy at approximately the deformation radius.

The energy of the 'storms' is injected only in the second mode. For small storms, $\mathrm{Br}_2 > 1$, the fluid is quasi-2D and the height anomaly relaxes until it reaches the deformation radius L_{D2}, where it can be balanced geostrophically. Large storms ($\mathrm{Br}_2 < 1$) experience a direct cascade until motions reach the deformation radius. Either storm size causes energy to accumulate near the scale L_{D2}, at which point it undergoes a *vertical* cascade to the next gravest mode Charney (1971). As fluid motions align vertically, they behave more like a one layer fluid with a larger deformation radius, L_{D1}. This vertical cascade and subsequent source of energy to the gravest motions is called barotropization. The lowest mode in this model is the first baroclinic mode, so we expect and observe equivalent barotropic motions to maintain height perturbations in geostrophic balance.

Barotropization is faster and more efficient in the presence of higher β because enstrophy is conserved layer-wise, and a larger Coriolis gradient β increases depth-independent enstrophy (Smith and Vallis 2001, Venaille et al. 2012). An example of the beta's effect on barotropization can be seen in Figure 4-7. Identical baroclinic vortices are forced away from the pole, on a large-$\tilde{\beta}$ planet and a small-$\tilde{\beta}$ planet. The

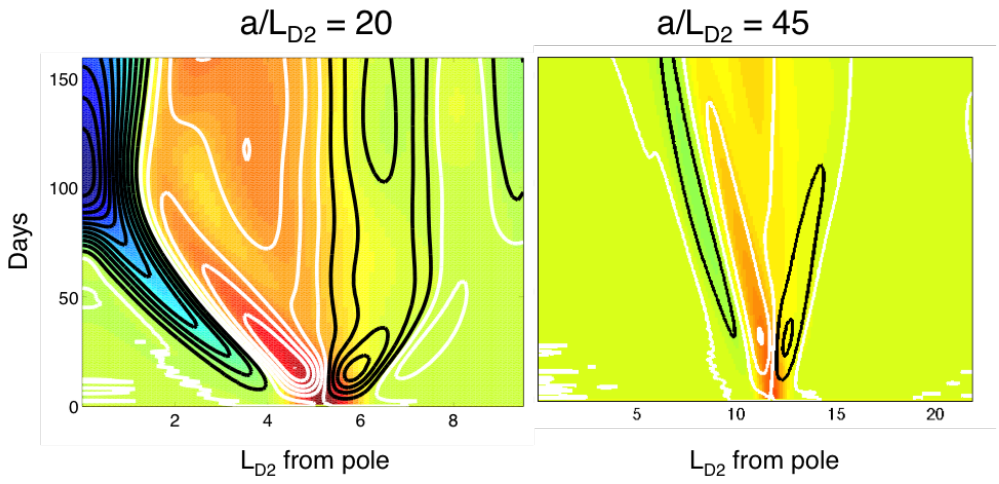

Figure 4-7: The colors are the azimuthally averaged perturbation PV, $< q_2' >$, of the lower layer (green marks $< q_2' >= 0$). White contours indicate positive, and black contours indicate negative depth-integrated perturbation PV. The contour intervals are the same for each graph, denoting an increase or decrease of $5e-4$.

color in the image is the azimuthally averaged lower layer perturbation PV, $< q_2' >$, and the contours are the azimuthally averaged depth-integrated PV $< q_1 h_1 + q_2 h_2 - 2f(r) >$. The two storms are initialized at the same angular distance from the pole.

The contours are a measure of the barotropization of the fluid, and would not appear for purely baroclinic motions (here the small density difference has been ignored). We can see that the lower level cyclone is able to spin up more upper layer fluid, more quickly, than its counterpart on the large planet. We can also see that while the cyclone moves poleward on the large-$\tilde{\beta}$ planet, it temporarily advects negative $< q_i' >$ over the pole in both layers before it reaches the pole. The cyclone on the small-$\tilde{\beta}$ planet has the same size and intensity, but is unable to self-advect a meaningful distance poleward. Nonlinear effects can still be seen in the advection of low-PV air poleward of the original cyclone. Strong storms on large-$\tilde{\beta}$ planets appear the most promising candidates for polar cyclone forcing when isolated, and the next experiment suggests that strong vortex-vortex interaction does not change this observation.

4.2.3 `Xmult`

The `Xmult` group of experiments is also unforced but allows multiple baroclinic storms to interact with each other. The pole, as always, is placed in the center of the domain. Seven storms are placed across the four quadrants, and six of the storms are closely paired with another (Figure 4-8). Two of the pairs are placed a constant distance apart, regardless of storm size. The third pair's separation is twice the storm radius with respect to L_{D2}, equivalent to $2\sqrt{\mathrm{Br}_2}$. These simulations have the potential for strong same-layer vortex interaction, and at early times we can examine the impact of the separation distance on vortex interaction. The parameters of each simulation are in this chapter's Appendix, Table 4.3.

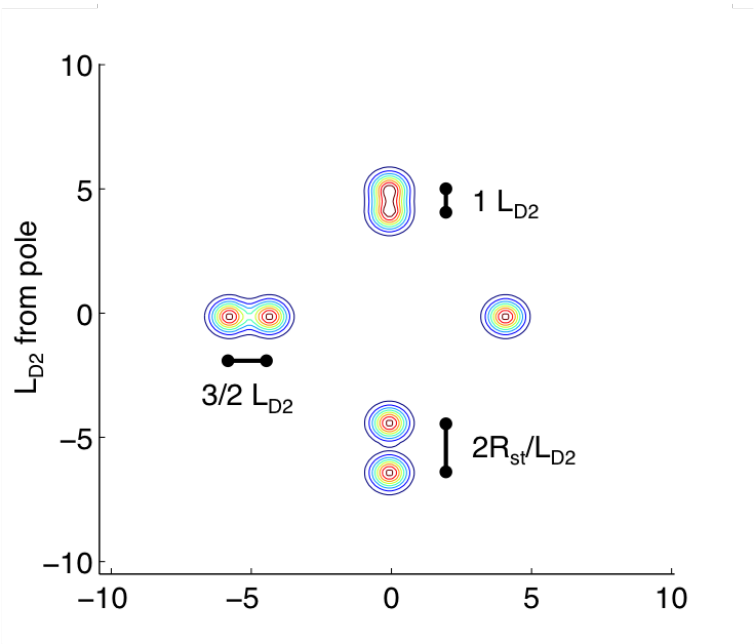

Figure 4-8: This is the forcing configuration. Seven storms are initially forced by a mass flux and then allowed to evolve. The x and y axes are the same and the figure shows a plan view of the domain centered on the pole.

The end states vary depending on the total energy forcing of the initial system. The cyclones in the strongly forced simulations are able to reach the pole after merger with their local partner, and then form a larger, stable polar cyclone in the lower layer (forced-dissipative models, discussed in the next chapter, suggest that with more time

or more energetic forcing, the upper layer would also exhibit a polar cyclone). Weaker forcing is wave-dominated, with virtually no nonlinear PV mixing. A profile of the decaying end state is shown in the left panel of Figure 4-9 for a series of simulations run with increasing Ro_{conv}. Recall that Ro_{conv} is $\propto \sqrt{(E_p)}$, and also increases the PV of a particular storm upon reaching balance, for all other parameters held equal. This is a well known phenomenon on a beta plane - the PV anomaly can result in either waves or nonlinear beta drift, depending on its intensity (e.g. Flierl 1984).

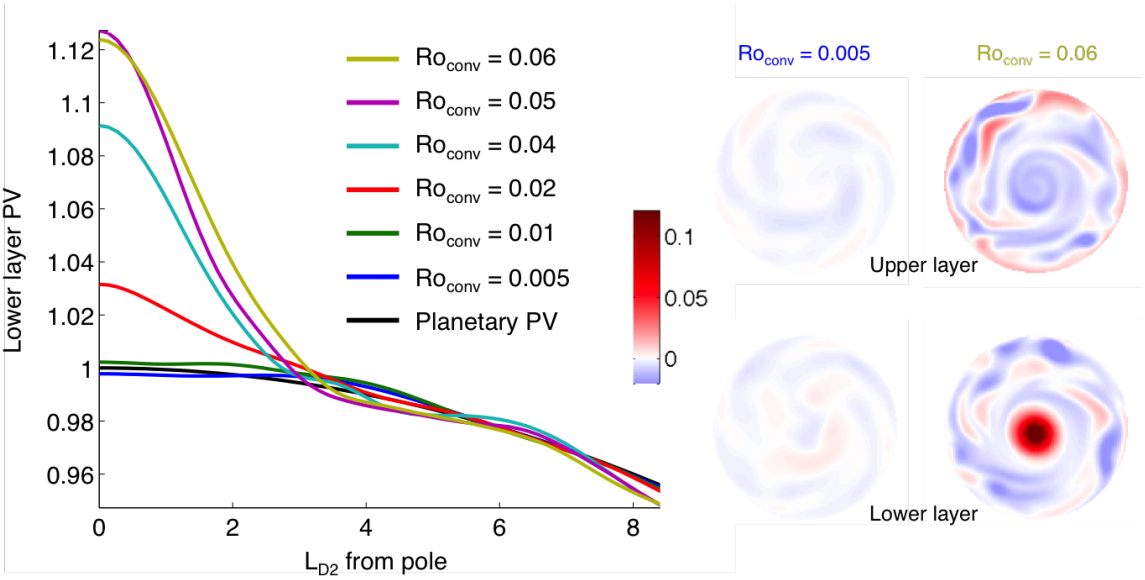

Figure 4-9: Left panel: the radial profile of PV in the lower layer for experiments `ix69-ix74`, in which only Ro_{conv} is varied. Right panel: the plan view of the upper and lower layers for the extremal cases, `ix69` with weak forcing and `ix74` with strong forcing. The field shown is the perturbation PV, $q' = PV - f(r)/H$. The strongly forced simulation on the right side is saturated at about 85% its maximum value to allow the perturbations in weaker wave-like simulation to be visible.

4.2.4 Comparing energy with E_p

A modified energy parameter E_p can be found for these unforced models. It is similar to E_p but the radiative relaxation timescale and the storm period timescale have been omitted, since they are both essentially infinite. Figure 4-10 shows the relationship between the modified E_p and the total storm energy for experiments `Xbclin` and

`Xmult`.

All of the experiments lose energy quickly because of the high dissipation. Total E in Figure 4-10 was calculated at day 1.6 (`Xbclin`) or 3.2 (`Xmult`). The fit to E_p worsens differentially among the simulations as time increases. In particular, the large-$\tilde{\beta}$ planets lose energy more rapidly than small-$\tilde{\beta}$ planets, because strong anticyclonic features drift equatorward more quickly, where they are damped by the sponge layer.

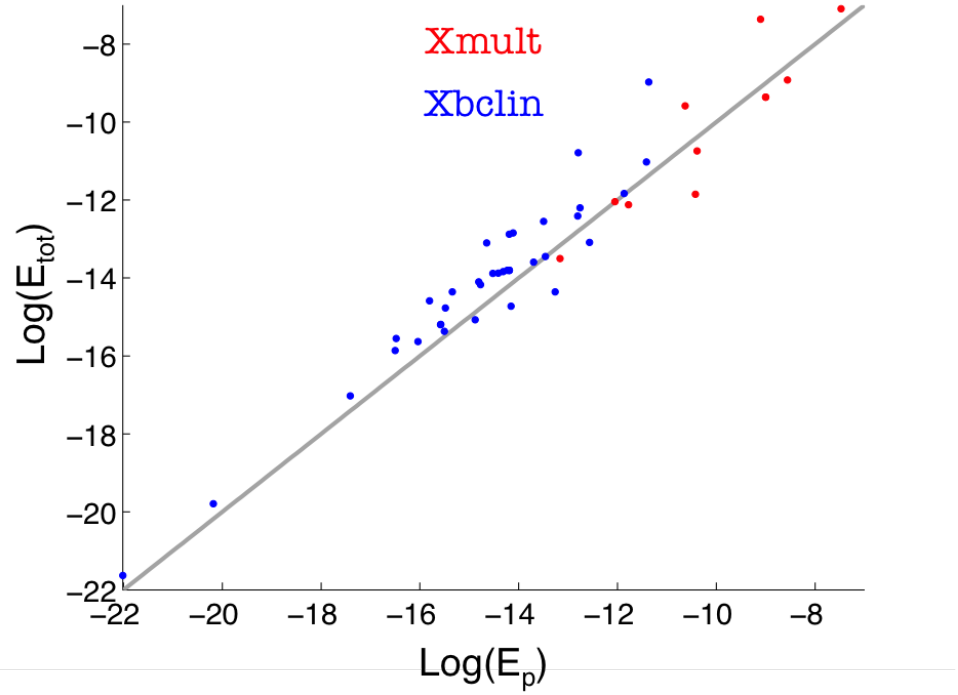

Figure 4-10: The model energy as a function of E_p. The potential energy is a large fraction of the total energy, so they are each a good fit to E_p. The `Xmult` experiments are more energetic than the single-storm `Xbclin` experiments. E_{tot} was additionally multiplied by dx^2 to account for different resolutions.

The energy parameter is a decent predictor of both potential energy and total energy (they scale together), which is what we hoped. The most and least energetic simulations are each represented well by E_p.

4.3 Conclusion

A planet's pole is a special environment. A large body of work has examined the motion of coherent vortices on the beta plane, and the polar environment is relatively less well understood. If a vortex is strong enough to reach the pole before it is dispersed, and if it is small enough not be torn apart by barotropic instability, the mechanisms for its dissipation are greatly reduced. The simulations described in this chapter exhibit behavior very similar to that described in other works, except the vortices reach the pole within the integration time. Scott (2011) focuses specifically on the pole problem and allows 1-layer QG patch vortices to freely advect and reach the pole. He finds that small patches of cyclonic vorticity do aggregate near the pole to form a larger cyclone, which efficiently mixes the PV of the polar cap. To our knowledge, a study of differential barotropization of a baroclinic model on the pole has not been conducted, and would be a natural extension of the simple simulations produced here. For the current study, we have learned that this model preferentially promotes polar cyclogenesis for a) larger or more intense storms (higher E_p) and b) larger-$\tilde{\beta}$ planets.

We have shown that the energy parameter E_p qualitatively captures the effect of individual parameters on fluid behavior - as the energy increases, vortices are more coherent for longer. E_p does more poorly in cases where very strong gradients at the grid scale contain most of the initial energy, because of unfortunately high viscosity. However in a strongly forced model this may not matter, as intense storms may strongly interact with nearby features before hyperviscosity can remove an appreciable fraction of energy. In the forced-dissipative cases we will examine the dependence of equilibria on several parameters, including E_p, and demonstrate that E_p works well as a scale for energy at equilibrium.

4.4 Appendix

name	$\mathbf{Ro}_{conv}$	$\mathbf{Br}_2$	a/L_{D2}	ρ_1/ρ_2	H_1/H_2	L_{dom}
Benchmark	0.02	1	30	0.95	1	31.5
ix1	0.065					
ix2	0.25					
ix3	1					
ix4	4					
ix51		1/2	20			21
ix52		1/2	25			26.25
ix53		1/2				
ix54		1/2	35			36.75
ix55		1/2	40			42
ix56		1/2	45			47.125
ix5			20			21
ix6			25			26.25
ix7						
ix8			35			36.75
ix9			40			42
ix10			45			47.125
ix45		2	20			21
ix46		2	25			26.25
ix47		2				
ix48		2	35			36.75
ix49		2	40			42
ix50		2	45			47.125
ix11					0.25	
ix12					0.5	
ix13					0.75	
ix14					1.25	
ix15						
ix16	4e-4					
ix17	1e-3					
ix18	4e-3					
ix19	1e-2					
ix20	4e-2					
ix21	8e-2					
ix22				0.6		
ix23				0.7		
ix24				0.8		
ix25				0.9		
ix26						

Table 4.2: `Xbclin` experiments. The **bold** experiments have identical setups and identical integrations to within machine error.

name	$\mathbf{Ro}_{conv}$	$\mathbf{Br}_2$	$\tilde{\tau}_{st}$	ρ_1/ρ_2	$\tilde{c}_1^2$	$\tilde{c}_2^2$	$\tilde{\tau}_{rad}$
Benchmark	0.04	1	6.3	0.9	11	10	
ix57		1/4	6				1e4
ix58			6				1e4
ix59		4	6				1e4
ix60		1/4					
ix61							
ix62		4					
ix63		1/4		0.68	3	2	
ix64				0.68	3	2	
ix65		4		0.68	3	2	
ix69	5e-3						
ix70	1e-2						
ix71	2e-2						
ix72	4e-2						
ix73	5e-2						
ix74	6e-2						

Table 4.3: `Xmult` experiments.

Chapter 5

Forced-dissipative experiments

5.1 Introduction

While the previous chapter deals with simple decaying experiments that can isolate the importance of a single parameter, we have no such luxury either in constantly forced models or in observations. Planets are messy, and the time evolution of the following experiments demonstrates that even if major events, like large vortex merger, occur instantaneously, a statical equilibrium can be very steady.

The first finding of this thesis is that forced-dissipative simulations can create and sustain a coherent equivalent-barotropic polar cyclone with only baroclinic forcing. The second finding is that the presence or absence of a polar cyclone, and its behavior within the domain, can be understood primarily with only two nondimensional parameters: a modified E_p ($\hat{E}_p$, defined in Section 5.2.1) and $\tilde{\beta}$. We find that:

- The energy parameter $\hat{E}_p$ has predictive skill across more than two orders of magnitude, and $\hat{E}_p$ and $\tilde{\beta}$ can describe all statistical equilibria of the model. The different equilibria are, roughly:

- **Large-$\tilde{\beta}$ planets:** Low $\hat{E}_p$ simulations are wavelike, with multiple very weak jets. As $\hat{E}_p$ is increased, cyclonic eddies move poleward and a broad, transient region of positive perturbation PV collects on the pole. As $\hat{E}_p$ is further increased, the transient region becomes much stronger and more symmetric. Fi-

nally, more energy causes the polar cyclone to orbit/precess at greater distances from the pole.

- **Small-$\tilde{\beta}$ planets:** A much weaker effective Coriolis gradient allows initially wavelike behavior to create and then merge multiple coherent vortices away from the pole, as $\hat{E}_p$ is increased. Beyond the short deformation radius, a limited range of interaction and weakly nonlinear beta drift keeps low-energy behavior local. Stronger forcing can cause one or more strong circumpolar cyclones, but they will not be stable near the pole, instead directly transitioning to a polar orbit or nearly random motion.

- $\hat{E}_p$ can provide an accurate predictive velocity scale, which allows one to solve for a Rossby number R_o, a (nondimensional) Rhines length scale L_{Rh}, and an anisotropy parameter α, which compare favorably with model output. The nonlinearity parameter α successfully predicts jet formation in the model.

- Strong polar cyclones may be self-sustaining, by creating a collar of low positive PV around them that can provide an increase in effective beta in the immediate polar region.

- The radiative relaxation scheme induces a meridional circulation in both layers in medium-high $\hat{E}_p$ simulations, as it adds mass to the pole where layer thicknesses are anomalously thin, and removes it from the relatively thicker outer regions at each time step.

- Shortcomings in this type of model and geometry limit the applicability of our results to polar cyclones with Rossby number less than 1; namely, the shallow water system does not permit an overturning circulation, which is a natural outcome of strong vortices in stratified fluids.

Section 5.2 discusses the relevance of E_p as a predictor of model behavior. Section 5.2.1 modifies E_p to better predict total energy of the model. Section 5.3 demonstrates that this new $\hat{E}_p$ can predict a peak model velocity, and introduces an anisotropy

parameter, used in previous works. Velocity fields for both high and low $\hat{E}_p$ are also provided, showing that very weak forcing leads to multiple weak jets.

A table is provided in this chapter's Appendix, with the parameters of the simulations relevant to this study. Most simulations were run from 600 to 1100 days, and typical storms lasted 0.5 days with frequency of a day. The typical radiative timescale was never more than half the simulation duration.

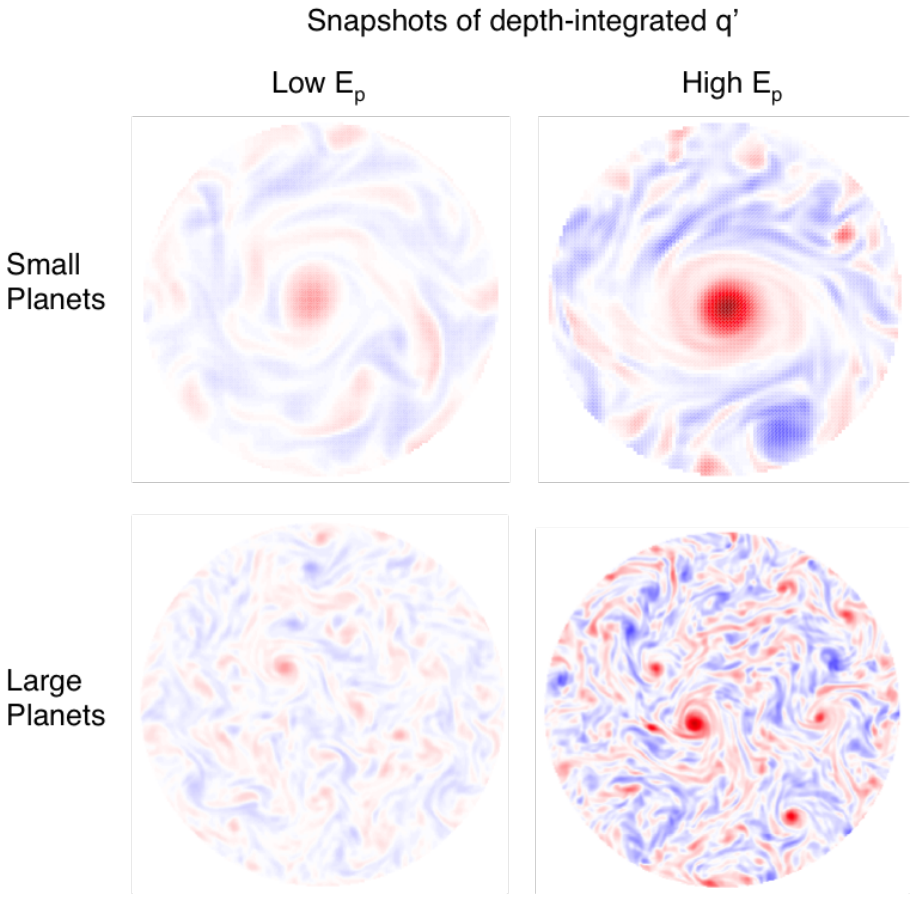

Figure 5-1: Snapshots of depth-integrated PV. The top row, left to right, is simulation `id483` and `id499`; the bottom row is `id515` and `id517`.

Figure 5-1 shows snapshots of model behavior for four different parameter spaces. The field is a depth-integrated perturbation PV:

$$q_1 h_1 + q_2 h_2 - 2f(r) = \xi_1 + \xi_2 \tag{5.1}$$

The relative vorticity of layer i is ξ_i and the final term on the left side is twice the radially dependent background planetary vorticity.

The domain beyond the outer circular limit, where motions are strongly damped by the sponge layer, is omitted[1]. These snapshots of q' effectively show the barotropic component of the perturbation PV. Because the planetary component of PV has been removed, red colors indicate depth-integrated PV greater than the local background PV $(1 - \tilde{\beta}r^2)/H$. The small baroclinic storms themselves don't appear in this field because they integrate to zero, until they are vertically tilted. The figure illustrates a portion of the regime space observed in $\hat{E}_p$ and $\tilde{\beta}$.

5.2 E_p as a predictor

The unmodified energy parameter E_p appeared important early on in this project. Increasing the storm size, or number, or strength, or duration, consistently results in a higher likelihood of a strong cyclone in the domain. An increase in the storm frequency or the radiative timescale is also conducive to a polar cyclone. The only single parameter that seems to play a *unique* role in polar flow behavior is the Coriolis parameter $\tilde{\beta}$.

The original 11 nondimensional parameters are straightforward to find from a scaling of the shallow water equations, but one can imagine any number of combinations of the parameters that would also be dimensionless. We find that the original nondimensional set of the system has only one dimension along the largest gradient of fluid behavior - the scaled Coriolis gradient $\tilde{\beta}$. E_p or $\hat{E}_p$ can be considered a nondimensional parameter from another set of combinations, and $\tilde{\beta}$ and $\hat{E}_p$ appear to describe the greatest variance in behavior. It would be incorrect to assume that the regime space is completely flattened to two dimensions. This is apparent, for example, when

[1]The sponge layer is not responsible for containing a medium energy cyclone near the pole. If it were, this would be a significant deficiency of the model, because we argue that only the polar beta plane is necessary for a polar cyclone. A simulation run in the current version of the model, without a sponge layer, also created a polar cyclone. The major difference was that the total energy increased linearly for the duration of the integration, while the corresponding model with a sponge layer was able to reach statistical energy equilibrium well before. Scores of simulations run in a previous version of the model, before the sponge layer implementation, confirm the same result.

we reduce ρ_1/ρ_2 by 50%, or change H_1/H_2 more than marginally. However, it seems likely that $\tilde{\beta}$ and $\hat{E}_p$ serve as the largest two eigenvectors in a principal component analysis, though the present set of simulations is insufficient for statistics, given the 11 independent dimensions[2].

Empirically, the energy density in a given simulation appears to strongly affect its equilibrium behavior, and it is desirable to predict the energy density based on control parameters - this is the role of E_p. Single-parameter (varying E_p) and fixed E_p (co-varying parameters such that E_p is constant) correlations are shown in Figures 5-2 and 5-3. The first figure shows the relationship between the measured output energy $log(E_{tot})$ and the log of one nondimensional parameter (first six plots); or groups of parameters within E_p such that E_p remains constant (final four plots). The second of the two figures shows the same set of experiments, except that the y axis is $\log(E_p)$ instead of $\log(E_{tot})$.

The storm parameters Ro_{conv}, $1/\mathrm{Br}_2$ and #, when varied independently, are strongly correlated with an overall increase in the total energy of the storm (Figure 5-2). A caveat about the simulations shown here is that the Burger number is set to 1, so the concerns about radial dependence in the appendix of Chapter 3 are limited. Another observation is that varying the gravity wave speed ratio a lot barely impacts the total energy. This is fortunate because both the modal and layer gravity wave speeds on the planets are poorly measured. Looking to the final four subplots, it is evident that covarying factors of E_p does not have an impact at all similar to changing storm parameters individually. The exception is in the bottom right corner and will be discussed shortly. Figure 5-3 is similar to Figure 5-2, and a comparison of the two demonstrate that E_p changes similarly to the total energy E_{tot} when varying one or several other control parameters.

One can ask two questions to determine whether E_p is important. The first is: does E_p vary similarly to another parameter, such that the model outcome is the same when either is varied? The second is: if two or more parameters that comprise E_p

[2]It should be noted that the 11-dimensional space is NOT uniformly sampled, due to the time constraint of finite hours in a PhD program. The results presented here suggest that it would be unnecessary, but this of course cannot be guaranteed.

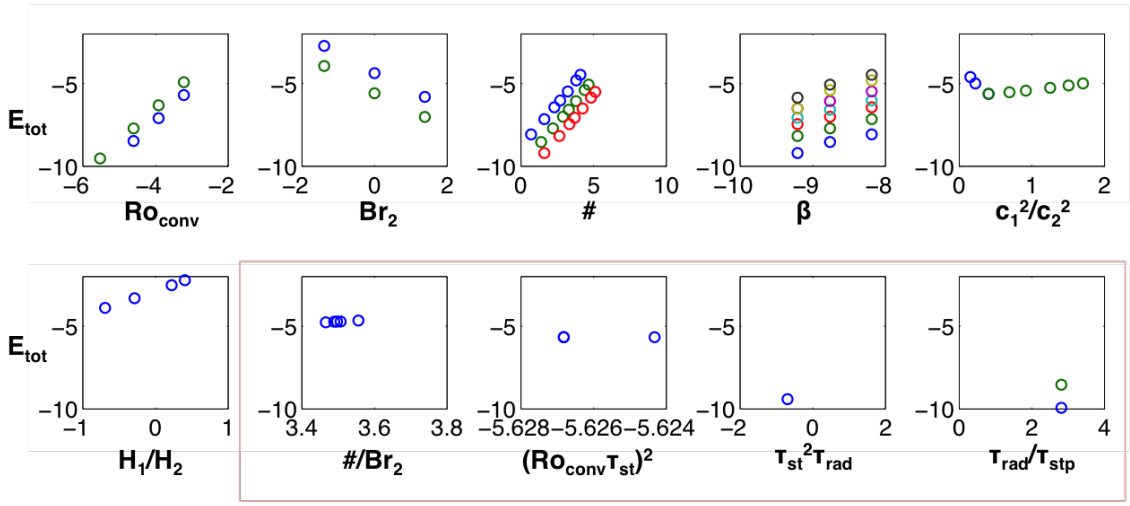

Figure 5-2: Single parameter variations; and holding E_p fixed (pink box). The log of total energy APE + K1 + K2 is shown on the y axis. Each group of a single color is a set of simulations where the given variable is varied, while others are held fixed. For example: in the top left hand plot, the vertical stretching term Ro_{conv} was varied, holding all other parameters fixed (the number of storms also varied between the green and blue set of simulations). The correlation with E_{tot} demonstrates that they are directly proportional. Note: x and y axes are logs of the labeled parameter.

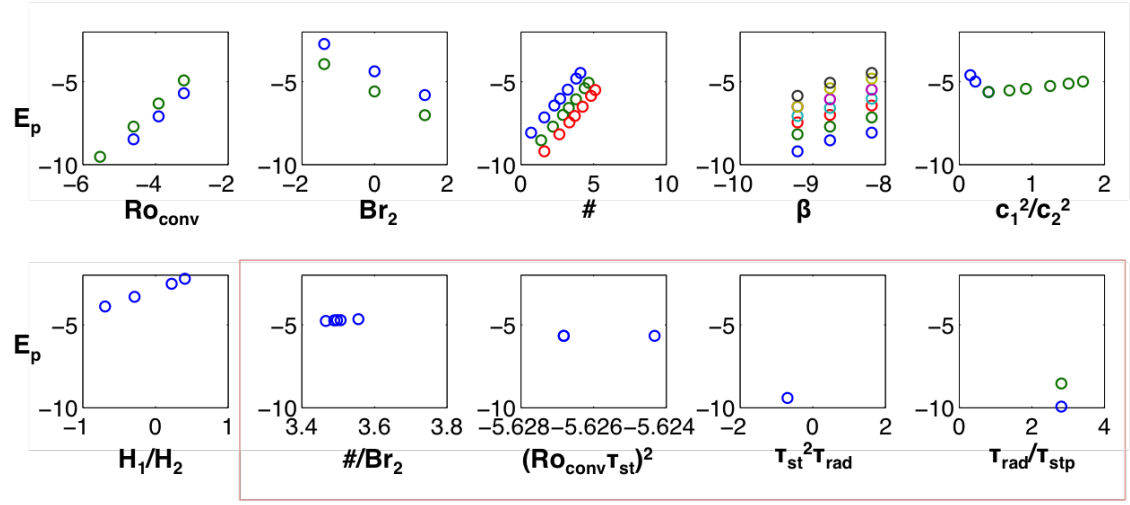

Figure 5-3: Same as Figure 5-2 but for $log(E_p)$ on the y axis.

are inversely varied, such that E_p remains constant, does the model outcome remain the same? The answer to both of these questions appears to be a qualified yes.

Figure 5-4 is an example of holding a factor in E_p constant, while co-varying the parameters within it. The product of the stretching term Ro_{conv} and the storm lifetime $\tilde{\tau}_{st}$ is an approximate storm perturbation height. The plan views in the left of the figure are instantaneous snapshots of layer-averaged q'. The strength of the polar cyclone is clearly a function of E_p, holding all else fixed, rather than the particular value of Ro_{conv} or $\tilde{\tau}_{st}$. The right panel shows surfaces of constant $\mathrm{Ro}_{conv}\tilde{\tau}_{st}$, with circles overlain that scale as the maximum q'.

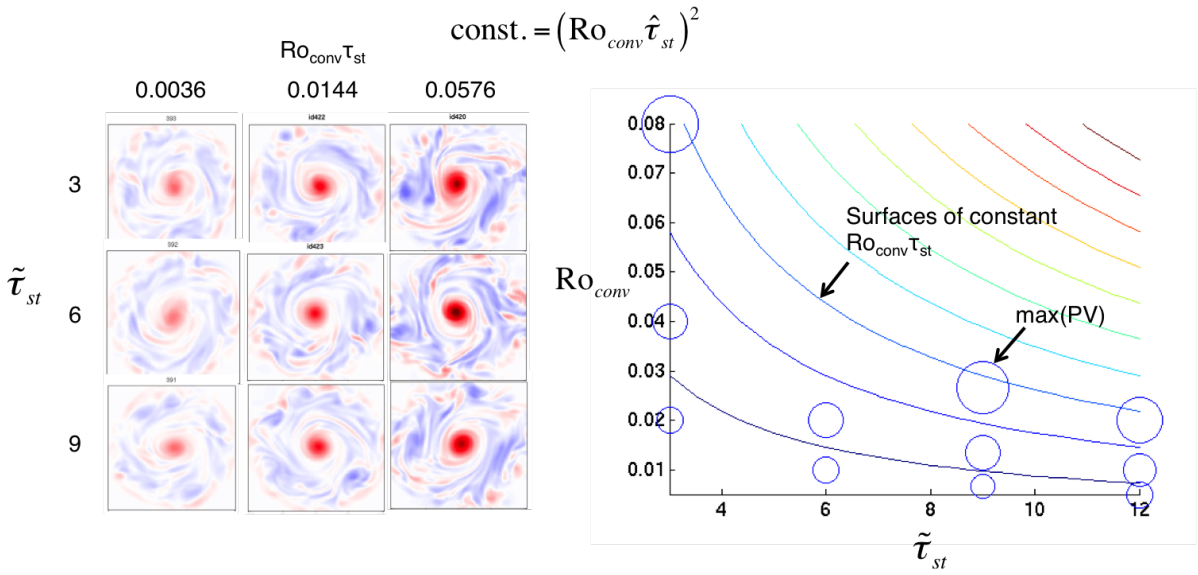

Figure 5-4: Two sets of experiments; holding $E_p \propto (\mathrm{Ro}_{conv}\tilde{\tau}_{st})^2$ constant among each set. The subplots on the left side show layer-averaged perturbation PV. The circle sizes on the right side scale with the maximum layer-averaged perturbation PV and approximately follow surfaces of constant $\mathrm{Ro}_{conv}\tilde{\tau}_{st}$.

In this instance, E_p works well as a scale of great interest. A less successful example is shown in Figure 5-5. Two sets of experiments are run, holding E_p fixed in each, and one set has twice the intensity (Ro_{conv}) of the other. Within each set, the ratio of the radiative timescale $\tilde{\tau}_{rad}$ to the storm return period $\tilde{\tau}_{tsp}$ is held constant (so E_p is constant, while they covary by a factor of 20. The total energy for either set of simulations varies by nearly a factor of four.

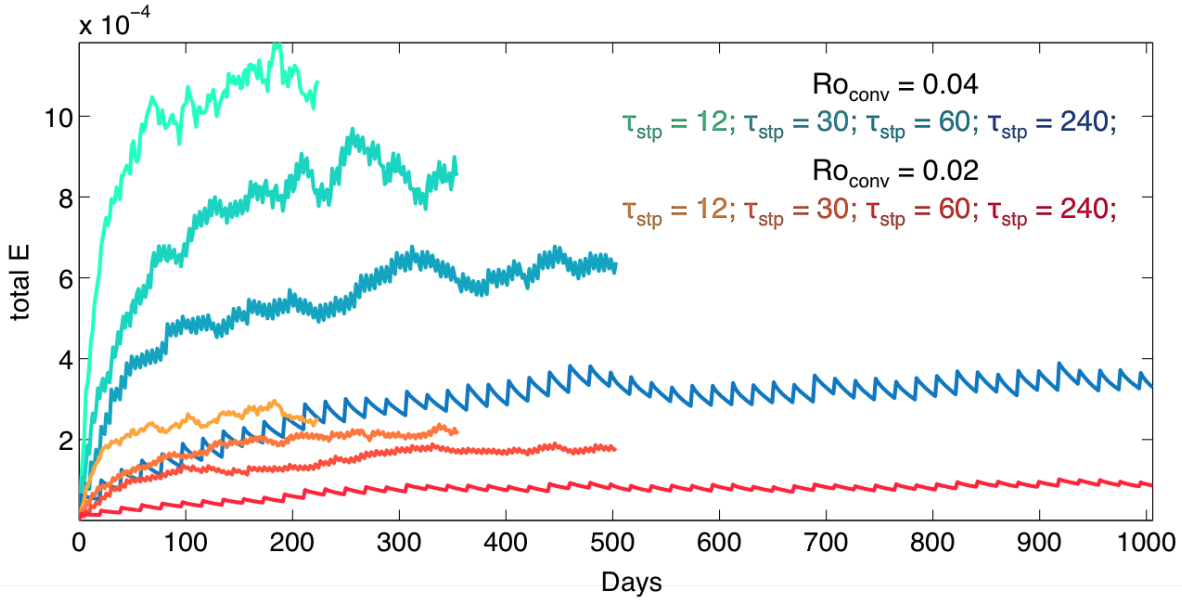

Figure 5-5: A time series of total energy for two sets of experiments, red (low forcing) and blue (high forcing). The simulations for small $\tilde{\tau}_{rad}$ are not integrated for as long because they reach a steady state more quickly. The sawtooth nature of the longest simulations is due to the storm return period, which is long enough to be resolved by the sampling frequency of the output.

That's unusually large for fixed E_p, but a factor of 20 is a very wide range compared to some other limits. There are two types of bounds on the parameters that control the model. Most parameters, if too high (Ro_{conv}, Re) or too low (ρ_1/ρ_2, H_1/H_2), will cause the model to become either numerically unstable (by violating the CFL condition) or physically unstable (wherein one of the layer thicknesses approaches zero). In contrast, the radiative relaxation timescale is limited only by patience and computing power, and so it can be varied dramatically. Also, note that the parameter set of the blue simulations and the red simulations varies by only $2\mathrm{Ro}_{conv}$, and this small difference is still enough to properly stratify them (though barely). Optimistically, this demonstrates a versatility in E_p for a wide range of time scales - or at least demonstrates a limiting applicable range of parameters that won't cause numerical instability.

5.2.1 A modified E_p

Whether E_p is a good scale for behavior is rather independent of whether it is actually a good scale for energy. Derived by scaling the storm parameters in the APE equation in chapter 3, it is evidently a scaling only for potential energy. This worked well in the unforced cases, where most of the energy was still stored in potential energy at early time steps. Depending on the modal nature of the flow at equilibrium, it is possible that much or most of the energy could be in kinetic form.

This leads us to consider the impact of the Burger number Br_2, which can serve as a ratio of potential to kinetic energy. When the Burger number > 1, storms are smaller than L_{D2} and cannot reach geostrophic balance, such that energy is stored in interface deviations. Much of the energy is instead converted to kinetic energy, as horizontal winds. A Burger number < 1 allows a large storm forcing to maintain interface deviations and store potential energy. Our energy parameter does not include a term for kinetic energy, because Br_2 only appears in E_p as a scaled storm area, without any connection to balanced flow. We can expect that the E_p of simulations with large Br_2 overestimates APE, because much of the energy becomes kinetic. This is indeed the case, as shown in Figure 5-6 (panel a). The size of the markers scales

linearly with the Burger number, and the for the largest Burger number simulations the energy parameter does overestimate APE. To correct the bias, one can divide E_p by the Burger number (panel b). Now all of the simulations suffer a too-high E_p with respect to APE, because we have ignored the portion of the energy that has been converted to kinetic energy. Panel (d) shows four different correlations, including the one we settle on: an E_p scaled by Br_2 does in fact scale well (in log-log space) with the total energy KE + APE. Throughout this chapter, multiple regressions could be performed on many different distributions, but instead a 1:1 line will be provided. This sampling of the large dimensional space was done selectively, to answer specific subquestions. Any fitting procedure would consequently be skewed toward large groups of experiments, and assign less weight to large changes in less well explored variables.

For the remainder of the chapter, we consider $\hat{E}_p = E_p/\mathrm{Br}_2$ to be analogous to E_{tot}, and use $\hat{E}_p$ as our primary energy scaling.

5.3 Regimes at steady state and $\hat{E}_p$

Statistically steady states of the forced-dissipative models exhibit a broad spectrum of behavior, from very low energy wave- and jet-dominated domains to very intense polar cyclones (Figures 5-7 and 5-8). The regimes are not a 1D spectrum but rather a 2D space; in $\hat{E}_p$ and $\tilde{\beta}$ (for ease of interpretation, figures use a/L_{D2} as a scale, for quick comparison to observed planetary radii).

Varying $\hat{E}_p$ over four orders of magnitude for three different values of a/L_{D2} (Figure 5-7) demonstrates the dependence of (circum)polar cyclone strength on $\hat{E}_p$. The lowest $\hat{E}_p$ simulations in this set do not exhibit a polar cyclone at all, but are instead dominated by weak jets. Snapshots do a poor job of revealing the unsteadiness of polar cyclones (In Chapter 7, Figure 5-7 is reproduced as Figure 7-1, except with time-averaged PV that better illustrates steadiness). Larger values of a/L_{D2} do not provide enough Coriolis gradient to keep a cyclone consistently near the pole, so the cyclones in those cases move around the domain more and are frequently asymmetric.

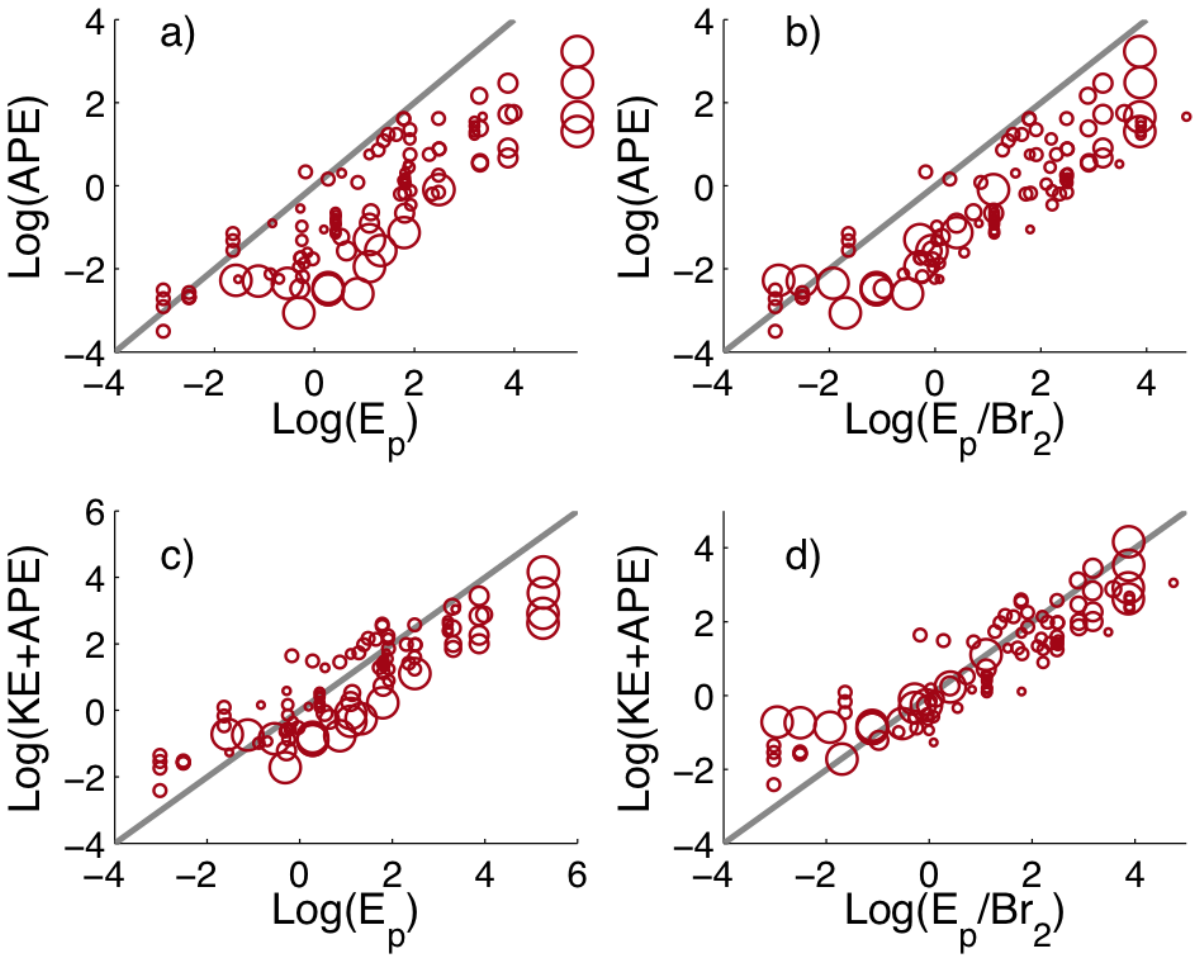

Figure 5-6: Simulations shown for $\rho_1/\rho_2 > 0.85$. The grey line in each plot is not a fit but rather the 1:1 line. The size of the markers scales linearly with the Burger number. The scaling most similar to the total energy (panel d) is E_p scaled by the Burger number. A larger plot of Figure 5-17 (d) is provided in the appendix, with labeled data points to allow cross-referencing with individual parameters.

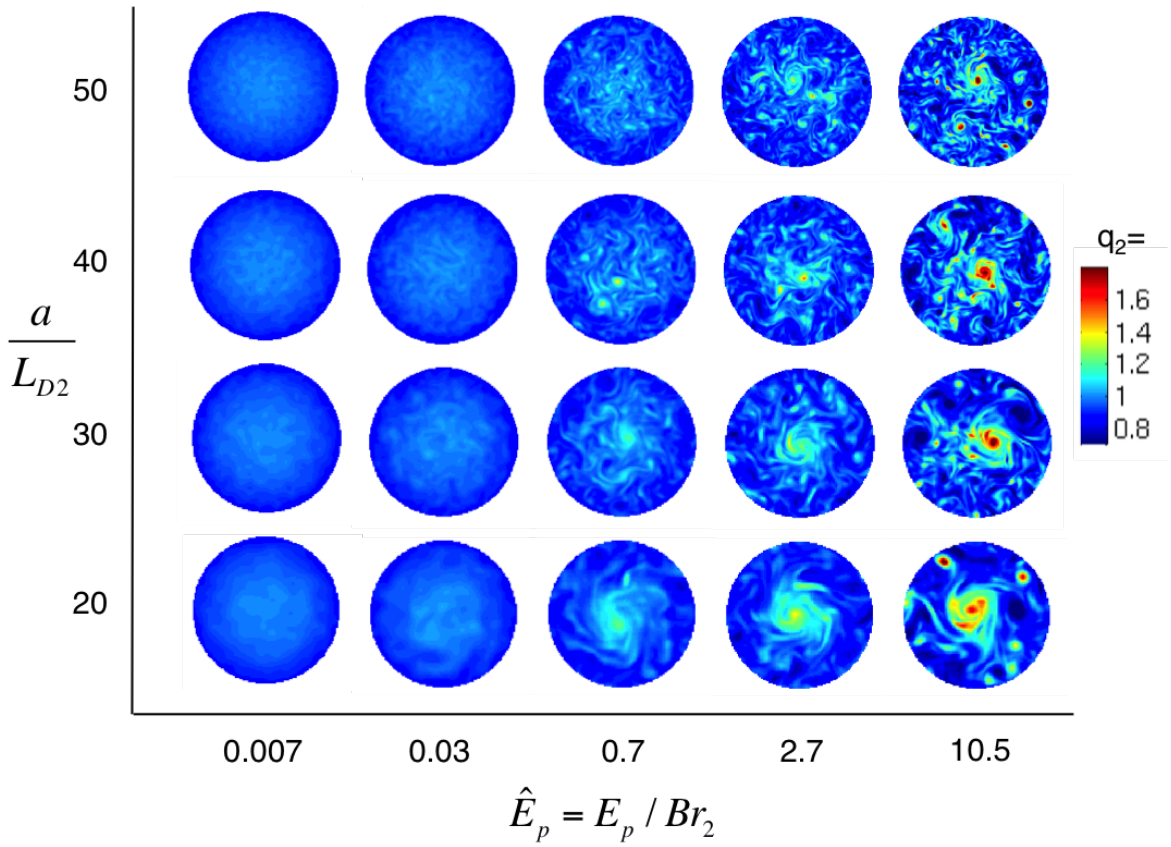

Figure 5-7: A series of simulations showing snapshots of the lower layer PV q_2, varying only a/L_{D2} and Ro_{conv} (which changes $\hat{E}_p$ exponentially). The right upper edge of the plot is continued in the next figure, with a different set of simulations and parameter space. The colorbar is allowed to saturate slightly to better show variations in the PV fields of low $\hat{E}_p$ simulations. Simulations are `id519-id541`.

A different set of simulations, shown in Figure 5-8, does not vary $\hat{E}_p$ as widely but does explore larger values of a/L_{D2}. The extent to which $\hat{E}_p$ does vary is controlled in this case by the number of storms. The top row shows the effect of high a/L_{D2}; namely, the Coriolis gradient is so low that multiple coherent vortices interact with their neighbors more strongly than with the planetary vorticity gradient.

It is difficult to visualize all of the simulations at once, and even harder to find single values or scales that can express a position in the regime space uniquely. Figure 5-9 is an attempt at conveying the results of many different simulations. The top row shows the layer-, time-, azimuthally averaged PV, and the bottom row shows the tangential velocity for the same averaging periods. The simulations have been binned by ranges of a/L_{D2}, which is inversely proportional to $\tilde{\beta}$. Multiple $\tilde{\beta}$ can share a bin, which is why some of the data appears to stop short in the domain. They are simply showing profiles from larger-$\tilde{\beta}$ planets.

The colors are a function of $\log(\hat{E}_p)$, and warm colors represent the most strongly forced simulations. Most sensitivity tests were run among single or groups of parameters, on larger-$\tilde{\beta}$ planets for computational speed. That is why the two largest-$\tilde{\beta}$ planet bins have the most output. We can visually appreciate that the most strongly forced simulations, those colored red, have weaker PV maxima and weaker jets as $\tilde{\beta}$ decreases. Across the range of $\tilde{\beta}$, the weakest models are able sustain a number of weak jets, distinct from the formation of a polar cyclone.

Long averages were taken to produce the radial profiles in Figure 5-9, which makes it difficult to assess the strength of the polar cyclones from the profiles. When snapshots are considered, they are often not monotonic. This doesn't implicate barotropic instability, because local β is vanishing and most of the zonal signal is from a large off-center coherent vortex projected on the azimuthal average. Other fields of study that examine strong vortices often place the center of the grid such that it follows the vortex (e.g. hurricanes), and that is a possibility that we could pursue in future work.

Both geostrophic turbulence and Rossby waves are permitted in our 2 $\frac{1}{2}$ layer RSW model. Depending on the parameter space, either Rossby waves or isotropic

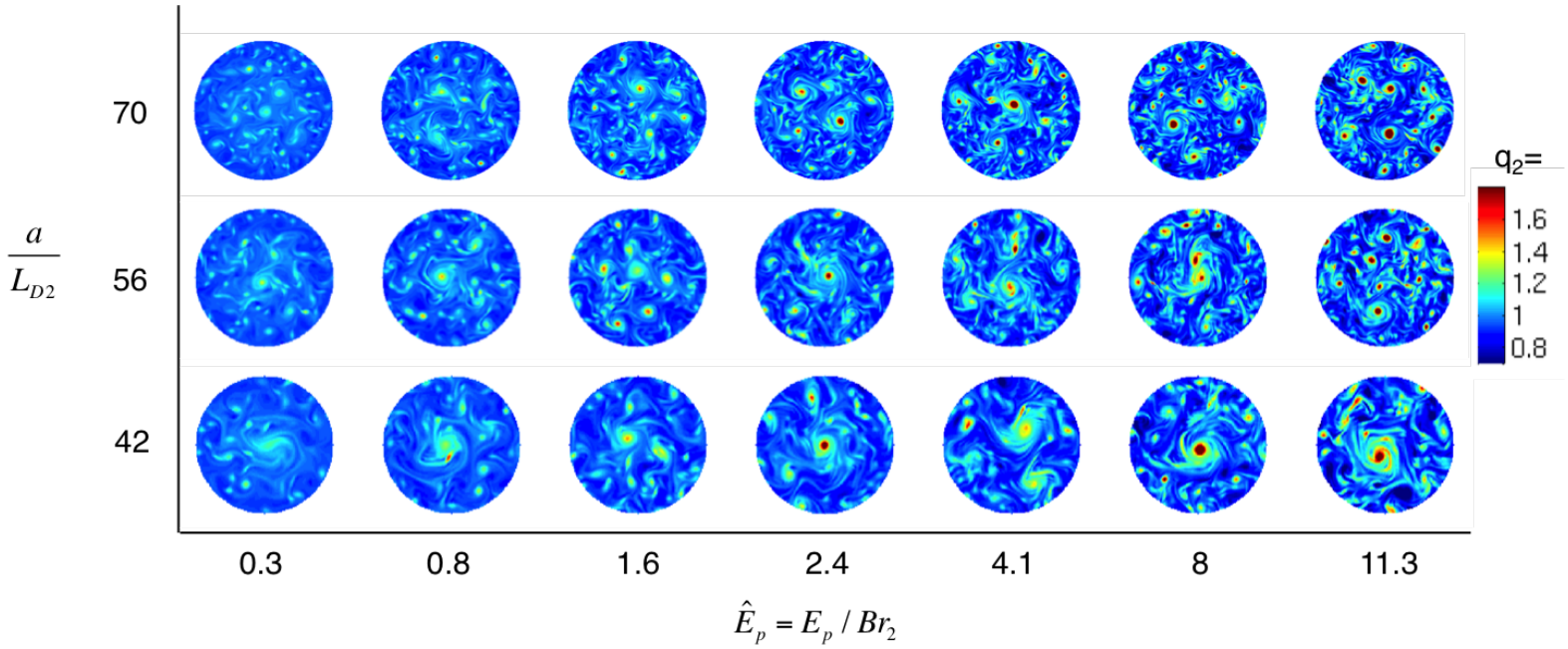

Figure 5-8: A series of simulations showing snapshots of the lower layer PV q_2, varying only a/L_{D2} and storm number # (which changes $\hat{E}_p$ proportionally). This set of simulations has a very strong stratification; $\rho_1/\rho_2 = 0.55$. This is unrealistic for a weather layer. Further work will determine whether this is the reason that a polar cyclone is observed at such high a/L_{D2} (low $\tilde{\beta}$). The colorbar is the same as in the previous figure. Simulations are `id368-id374; id404-id417`.

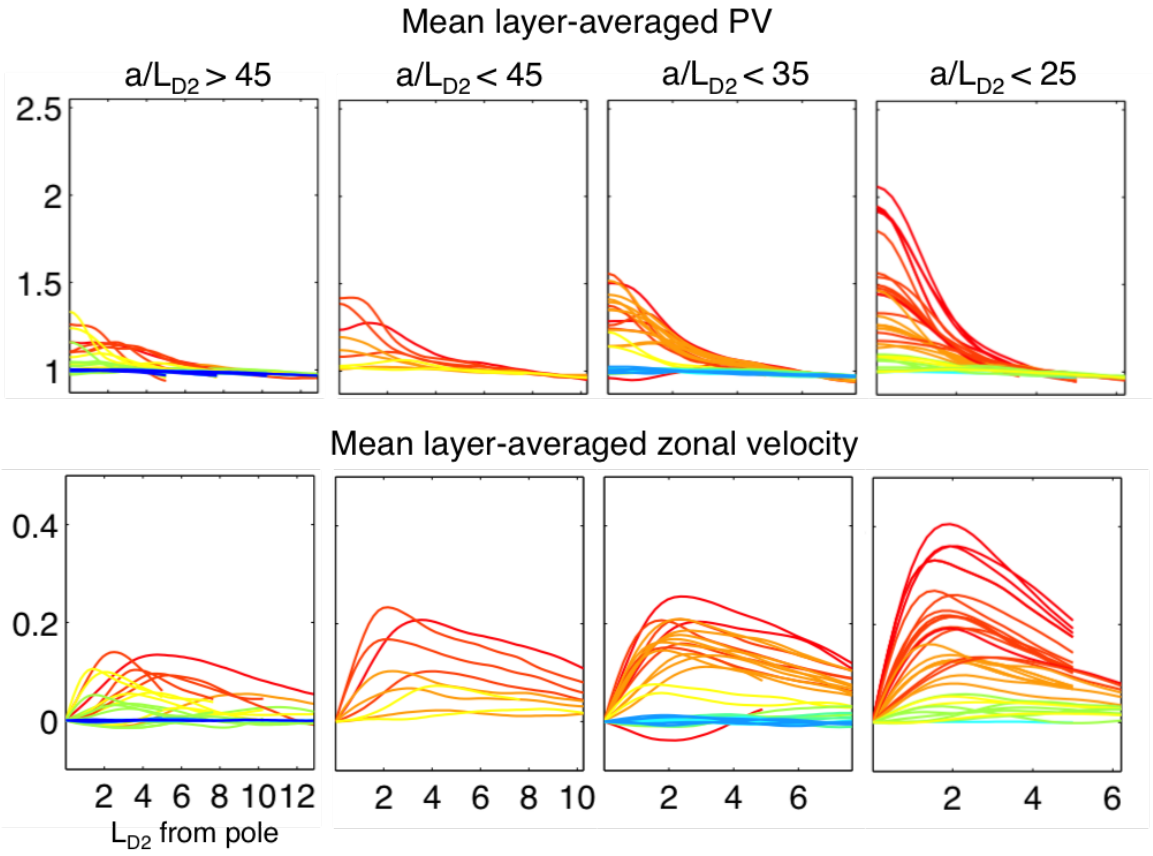

Figure 5-9: Simulations shown for all simulations where $\rho_1/\rho_2 > 0.85$ and $\mathrm{Br}_2 < 4$, due to physical relevance and high viscosity respectively. The top row is a radial PV profile, averaged azimuthally and over time and layer. The bottom row is a radial tangential wind profile, also averaged in azimuth, time and layer, at statistical equilibrium. Warm colors indicate high $\hat{E}_p$.

turbulence could dominate the flow; or, more often, a combination of the two can lead to significant wave-vortex interaction (e.g. Flierl 1977, Nycander 1994). The combination can be characterized by a nondimensional parameter α:

$$\alpha = \frac{U}{\beta L_D^2} \tag{5.2}$$

$$= \frac{L_{Rh}^2}{L_D^2} \tag{5.3}$$

The parameter α measures the separation of scales between coherent structures formed by turbulence, and long-range Rossby waves. It has many interpretations to the same effect: it is the "ratio of a characteristic turbulence velocity to the phase speed of baroclinic long Rossby waves (Okuno and Masuda, 2003)"; or, "the relative vorticity gradient, versus the planetary vorticity gradient, across a vortex (Smith, 1997)"; or, a threshold for anisotropy (Smith, 2004). Rhines (1975) recognized the impact of this balance for the barotropic case: when the Rossby wave timescale $1/\omega_{\mathrm{Ro}}$ is similar to or shorter than a turbulent or vortex timescale τ (both dependent on wavenumber), then Rossby waves can radiate energy zonally away from vortices at that scale (Smith 2004, Scott and Polvani 2007). In summary, for $\alpha \leq 1$, the flow is wave-like, and for $\alpha > 1$ it is turbulent (approaching isotropic turbulence for large α).

The primary advantage of being able to predict the polar behavior by a full $\hat{E}_p$ is that it provides a velocity scale of the correct magnitude, which varies by two orders of magnitude. Figure 5-10 shows the relationship in linear space between $\hat{E}_p$ and u_{max}, for a tangential u_{max} that is first layer averaged, and then azimuthally and temporally averaged:

A velocity scale allows characterization of the fluid flow in terms of more familiar nondimensional numbers. It is necessary for the Rossby number, if an appropriate length scale is also determined[3]. Likewise, the nonlinear threshold α needs only a

[3]It is not obviously L_{D2} because much of the energy is equivalent barotropic in equilibrium. It would be convenient though! Since our scaling sets $c_{e2} = f_0 = L_{D2}$, the Rossby number would then simply be the nondimensional velocity.

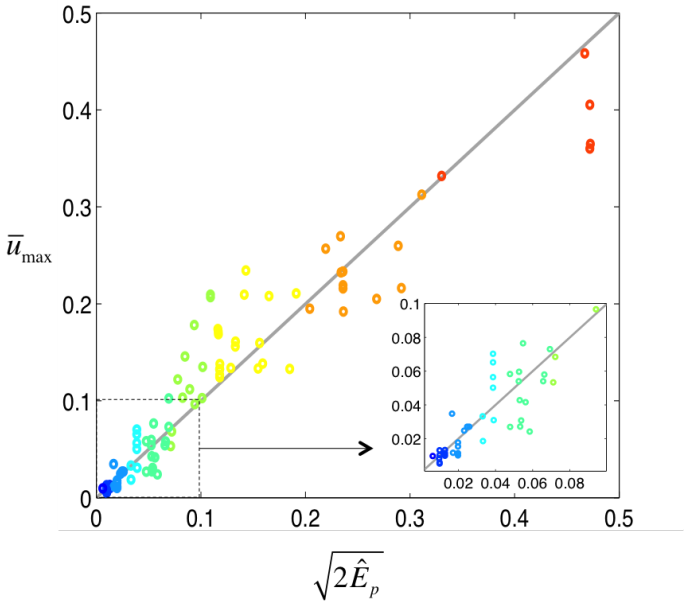

Figure 5-10: $\hat{E}_p$ v. mean tangential peak velocity. The inset plot is zoomed in near the origin to clearly show low $\hat{E}_p$ results. Grey line is 1:1.

velocity scale, since we already know $\tilde{\beta}$ and L_{D2}. Recall that when α is near or less than 1, fluid will behave more wavelike, and for large α we can expect fluid dominated by coherent structures and nonlinear turbulence. Figure 5-11 shows the correlation between α versus layer-averaged kurtosis (a 'flatness' of the fluid, as a function of layer-averaged relative vorticity). Because α is just the square root of twice $\hat{E}_p$, it is no surprise that more energetic models are able to create stronger, more coherent vortices, which can be demonstrated to an extent by the kurtosis.

The colors in Figure 5-11 indicate the number of local maxima in the layer-, time- and azimuthally-averaged tangential flow (the same quantity and interval used in Figure 5-9). The number of local maxima n is equivalent to $2n$ or $2n$-1 jets in the domain. Many of the radial velocity profiles in the lower left subplot of Figure 5-9 appear jet-like (Figure 5-12, left side). That isn't usually the case for larger-$\tilde{\beta}$ planets or more energetic fluids, which are dominated by a cyclone (Figure 5-12, right side). The parameter α works well for our simulations, and in concert with the kurtosis we can see a tendency for simulations to retain weak jets beyond $\alpha = 1$, if the fluid is

unable to organize into strong vortices. This plot also shows the relative magnitude of $\tilde{\beta}$, inversely proportional to the size of the circle. In general we can see that small-$\tilde{\beta}$ planets tend to have lower kurtosis even as the anisotropy parameter α increases. This is likely due to the fact that large-$\tilde{\beta}$ planets tend to have one cyclone, and small-$\tilde{\beta}$ planets tend to have several cyclones throughout the domain, none of which remain on the pole.

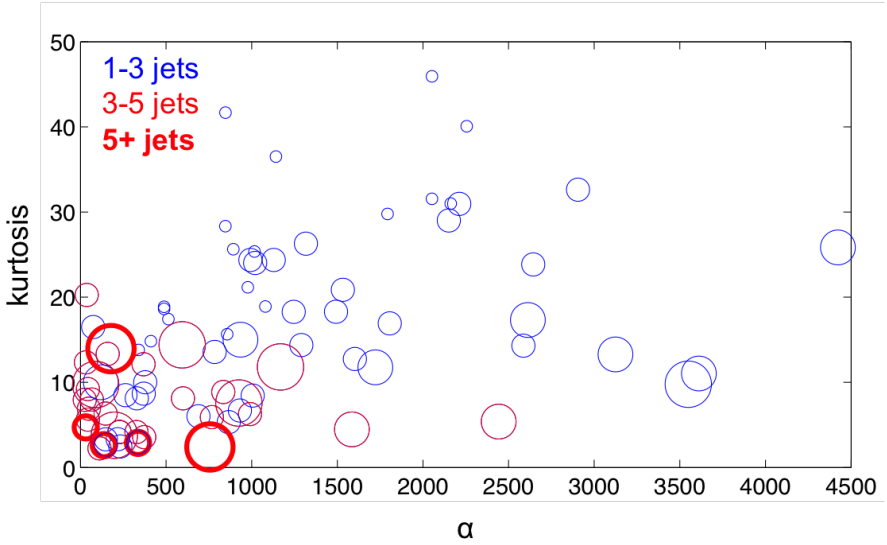

Figure 5-11: Anisotropy parameter α vs. mean kurtosis. Colors and line thicknesses indicate the number of jets in the domain in steady state. Circle size scales inversely with $\tilde{\beta}$.

A Rossby number $< u > /(f_0 L)$ can be defined either with the time-averaged jet speed or the root of $2\hat{E}_p$; they're essentially the same. A logical length scale is the averaged radius of maximum winds. The most intense simulations have Rossby numbers of 0.1-0.2 (calculated with the jet speed), which is lower than an instantaneous ratio of the cyclone's peak velocity versus its radius. Instantaneous Rossby numbers measured in that way can exceed one, implying cyclostrophic balance. This is not surprising, because many observations of jovian winds as well as jovian simulations find that the relative vorticity of the flow can exceed the value of the planetary vorticity. This can lead to a violation of the barotropic stability criterion, and has not yet been resolved.

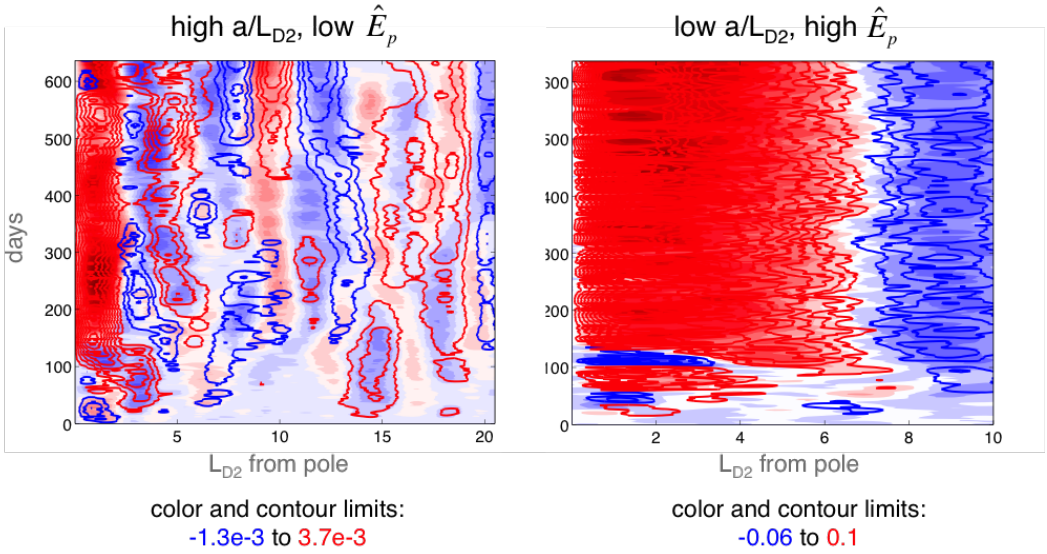

Figure 5-12: Hovmoller diagrams of jet formation for two simulations from Figure 5-7. The plot on the left side has an a/L_{D2} of 40 and an $\hat{E}_p$ of 0.007. On the right side, a/L_{D2}= 20 and $\hat{E}_p$= 2.7. The colored field shows the (nondimensional) lower layer winds and the contoured field shows the upper layer winds. Red colors are azimuthally averaged prograde winds; blue colors are azimuthally averaged retrograde winds. Note the large difference in contour values, necessary to show the structure of the very weak jets in the left side plot.

These nondimensional numbers are useful, but it is very difficult to recognize and appreciate the different regimes of the behavior without actually watching it evolve. Movies of evolution show dramatic vortex mergers, strong hetons mixing the whole domain, and occasionally unphysical events that likely would not occur in a fully 3D fluid.

5.4 A polar beta skirt

There are several quantities that various authors refer to as beta. It can be a global constant - simply a ratio of the planetary rotation rate to the planetary radius. It can also be a local gradient, as a function of latitude (for shallow fluids) or in our case, the radial distance from the pole. Yet another meaning can be borrowed from tropical cyclone literature, where the low but positive vorticity surrounding a hurricane has a gradient and can therefore provide an 'effective beta' to small vortical features in its close vicinity - in this case it is called a 'beta skirt' (Terwey and Montgomery, 2008). Any gradient in background potential vorticity can induce both Rossby waves and beta drift (Gill, 1982), and vortices can be as strongly influenced by curvature in the flow as by the Coriolis gradient (e.g. Achterberg and Ingersoll 1994). We will employ the term polar beta skirt to indicate a region around the pole with a negative radial gradient of PV.

Simulations with persistent, strong polar cyclones almost always exhibit a region of low positive q' that increases poleward. Concurrently, strong winds as well as vertical and horizontal wind shear retard the maximum q' that a storm might otherwise achieve in balance in a quiescent atmosphere (S07). The presence of a broad beta skirt may provide an additional mechanism for cyclone maintenance, by strongly promoting poleward self-advection of cyclonic anomalies even as the planetary vorticity gradient reaches approaches zero. A time average of the radial PV gradient for a set of simulations (the same simulations used in Figures 5-7 and 7-1) is shown in Figure 5-13.

Vortical anomalies need to be relatively strong (large and/or intense) in order to

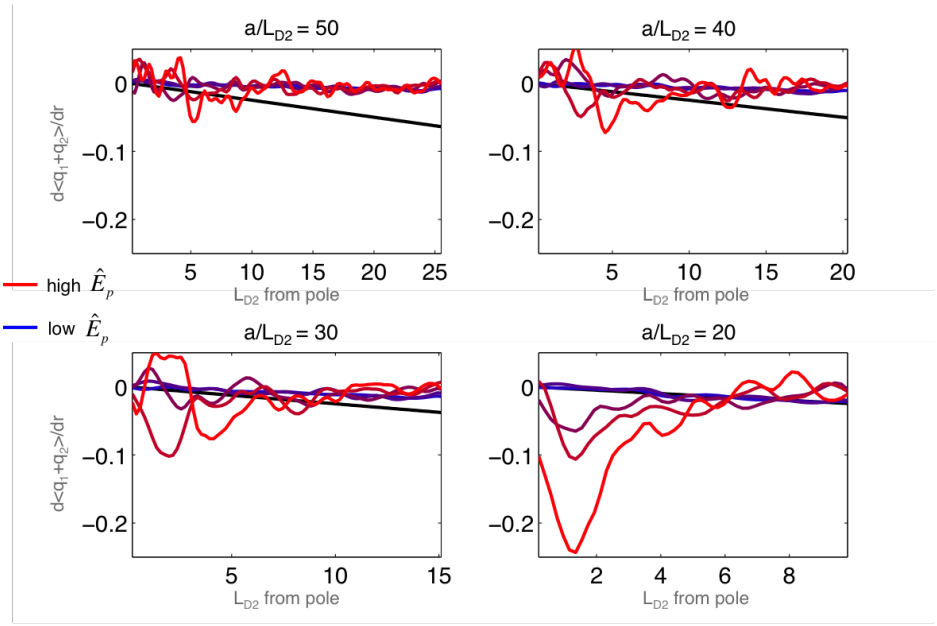

Figure 5-13: Layer- and time-averaged radial PV gradient. The black line is the Coriolis gradient, $df/dr = -2\tilde{\beta}r$, for comparison. The largest gradient conducive for beta drift is exhibited by low a/L_{D1}, high $\hat{E}_p$ simulations. The poleward-most radial value for each gradient has been omitted because it is undefined in a simple differencing scheme.

nonlinearly self-advect meridionally. This is especially important in a quiescent polar environment, where the Coriolis gradient vanishes at the pole. In a turbulent, sheared environment, it may be difficult for storm-induced anomalies to reach necessary intensity before they are sheared by the large-scale flow. The creation of a strong polar beta skirt concurrent with increasing horizontal or vertical shear near the pole may be sufficient for polar cyclone maintenance.

5.5 Diabatic effects and instability in a high $\hat{E}_p$ model

The two diabatic sources in the model, the storm forcing and radiative relaxation, redistribute mass at each time step. To examine the impact of diabatic effects on the PV budget, we construct an azimuthally averaged PV budget. The layer mass of the model is instantaneously conserved in an integral sense, including sources and sinks. PV is also conserved in an integral sense (but for small numerical error), as is depth-integrated PV. Neglecting friction and viscosity, the conservation equation is

$$\frac{\partial hq}{\partial t} = -\nabla \cdot (quh) + q\big[S_{st} + F_{rad}\big] \tag{5.4}$$

where F_{rad} is the radiative relaxation term. In a statistically steady state, the time tendency should go to zero, leaving a material balance between depth-integrated PV divergence and the forcing and removal terms. The forcing term can be calculated as a residual because the storms are seeded randomly in space and uniformly in time (also, regrettably, the random forcing field was never output). A time average over a sufficiently long interval does not remove the sink because radiative relaxation works faster for more intense features, and our polar cyclone is strong and consistently in the center of the domain. For any simulation with a polar cyclone, the layer thicknesses will be anomalously small in the region of the cyclone, due to geostrophic or cyclostrophic balance. The simple radiative scheme removes APE by adding mass

to thin regions and removing it from thick regions. For polar cyclones, this looks like a steady polar mass source, as radiative relaxation thickens the polar region[4]. This thermally-indirect vorticity forcing stretches high-PV fluid columns, which respond by increasing relative vorticity, and it is balanced by a mean radial mass flux away from the pole to the outer regions, where mass on average is removed (S07 discusses the dynamics on a beta plane).

In order to examine the flux-balance of $\partial\overline{hq}/\partial t$ in steady state, we partition the potential vorticity of each layer into azimuthal mean and eddy components:

$$q_i(r,\lambda,t) = \bar{q}_i(r,t) + q_i'(r,\lambda,t) \tag{5.5}$$

$$= \overline{\frac{f(r)}{h}} + \overline{\frac{\xi}{h}} + \frac{f(r)}{h}' + \frac{\xi}{h}' \tag{5.6}$$

$$\tag{5.7}$$

Given a mass flux $U = uh$ (with an extra factor of $\rho_1 H_1/\rho_2 H_2$ for the top layer) that is similarly partitioned, the four mass-weighted radial PV fluxes that operate in the long-time mean are:

Flux Description	Formulation
mean planetary vorticity flux MfF	$\bar{U}\overline{\frac{f(r)}{h}}$
mean relative vorticity flux MξF	$\bar{U}\overline{\frac{\xi}{h}}$
eddy planetary vorticity flux EfF	$\overline{U'\frac{f(r)}{h}'}$
eddy relative vorticity flux EξF	$\overline{U'\frac{\xi}{h}'}$

Similarly, the forcing term can be split into mean and eddy components:

[4]To be remotely relevant, the radiative timescale cannot be short enough to counteract the observed vortex instability for strong cyclones.

Forcing Description	Formulation
mean planetary vorticity source MfS	$\overline{F_{rad}}\overline{\frac{f(r)}{h}}$
mean relative vorticity source MξS	$\overline{F_{rad}}\overline{\frac{\xi}{h}}$
eddy planetary vorticity source EfS	$\overline{F'_{rad}\frac{f(r)}{h}'}$
eddy relative vorticity source EξS	$\overline{F'_{rad}\frac{\xi}{h}'}$

Ideally, one would take the divergence of these fluxes and compare them to the energy removal term. However, output in radial coordinates (linearly interpolated from Cartesian coordinates) should be treated cautiously in a model like this. The model output is originally in Cartesian coordinates, with a carefully constructed Arakawa C grid to conserve energy and PV. As soon the data is interpolated to polar coordinates, that precision is lost. The radial fluxes get close but don't quite reach zero in steady state, so simple differencing schemes cannot generally show zero divergence at the origin. The most relevant and interesting divergences are within just a few L_{D2} of the pole. Also, the polar cyclone is never perfectly stable, and chaotic vortical motions that look smooth in a plan view can look very dramatic in polar coordinates, if a vortex simply happens to pass quickly over the pole[5]. Given these considerations, we calculate just the fluxes instead, and provide a comparison to the diabatic term.

The radial PV fluxes and diabatic source/sink terms for the time periods are shown in Figure 5-15 (for the time intervals in Figure 5-14). Near the beginning of the simulation, the PV fluxes are largely equal and opposite in the layers. A Rhines scale[6] L_{Rh} where $\beta = 2\tilde{\beta}(6L_{D2})$, is $2.2L_{D2}$, which appears to be the same length as the radial flux oscillation. However the system is not in equilibrium at early times. The final state of this simulation does not produce more than one cyclone-induced jet, 10 times stronger than the weak jets implied and seen at early times.

Meanwhile, in the same early stage of the simulation, the diabatic term demonstrates the early accumulation of positive PV in the immediate polar region, as pic-

[5]This is another reason why the observed vortex instability is hard to identify- zonal averages are already rapidly changing, even before such an instability.

[6]The definition of the Rhines scale seems rather arbitrary in the polar region. In our case, with a quadratic variation in r of the Coriolis acceleration, one has to choose a location at which to define total β. Here we choose half of the radial domain length, $6L_{D2}$, as a representative location for L_{Rh}.

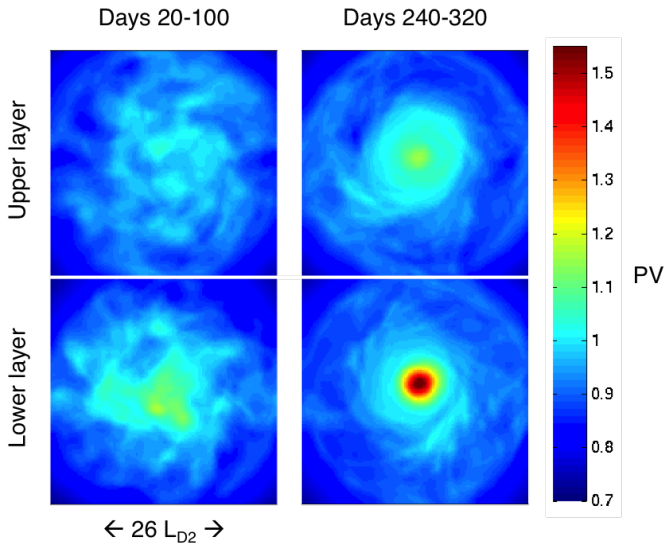

Figure 5-14: Time-averaged total PV in each layer for simulation `id471`.

tured in Figure 5-14. The fluid over the lower layer pole is greater than the background PV value (1), while there is some lower PV fluid over the upper layer pole. This is consistent with baroclinic storms preferentially self-advecting small cyclones in the lower layer poleward, and anticyclones equatorward, as we showed in the previous chapter.

When the simulation reaches statistical equilibrium, the divergence of the fluxes in the top layer should balance the source/sinks in the bottom layer, but the fluxes do not seem to be steady in the time mean. Instantaneous PV fluxes can change sign and are an order of magnitude larger than the time mean, which itself sensitively depends on the averaging interval. There is a relatively large radial mass flux of PV outward from the center of the storm. The largest fluxes, at this stage as well in the beginning of the simulation, are due to the planetary PV term MfF. The only inward PV flux near the pole is in the upper layer EξF term. Visual inspection suggests that it is a negative flux of a positive ξ/h, because across the models, the time mean and azimuthally averaged PV is never negative.

A more barotropic cyclone should have positive forcing terms in both layers, near the pole. Another issue to consider is friction's removal of vorticity and energy from the model, within the very strong vortices. Regardless, radiative relaxation is a

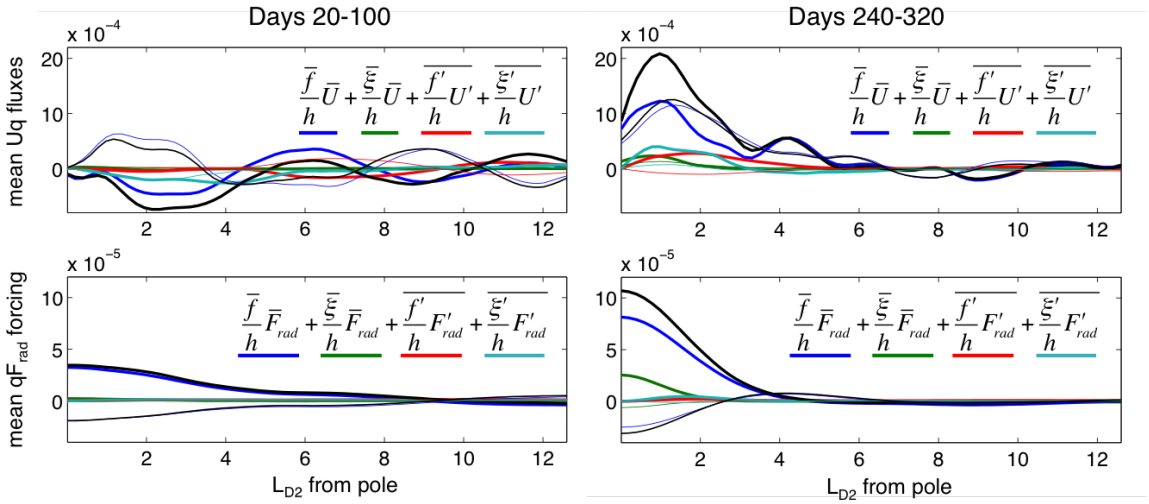

Figure 5-15: Mass-weighted PV fluxes in each layer (top row) and circulation forcing in each layer (bottom row). The left column is an average over days 20-100, and the right column is an average over days 240-320, for the simulation in Figure 5-14. The lower layer quantities have thick lines; the upper layer quantities are thin lines. The black lines are the sum of the fluxes of forcing terms, respectively, for each layer.

necessary simplification of real large scale heating and cooling in a shallow water model. Imagining our layer interfaces as isentropes, radiative relaxation removes entropy in the upper layer increases it in the lower layer. This is similar to behavior we expect in a real weather layer. The difficulty in the present model is that sometimes the location of the vortex alternates between layers, which flips the role of radiative mass/entropy transfer unphysically.

An instability in high $\hat{E}_p$ simulations

Several of the most energetic simulations exhibit very peculiar and dramatic behavior. Initially, a strong polar cyclone develops in the lower layer, and the upper layer begins to spin up as the vortex becomes barotropic. In some simulations, the lower layer vortex experiences explosive growth and then all of a sudden completely dissipates, only to be replaced by a vortex of similar intensity in the upper layer scores of days later. This can't be explained by barotropic instability, which mixes two layers equally, nor can it be explained by baroclinic instability, which would reduce the vortex slope rather than invert it.

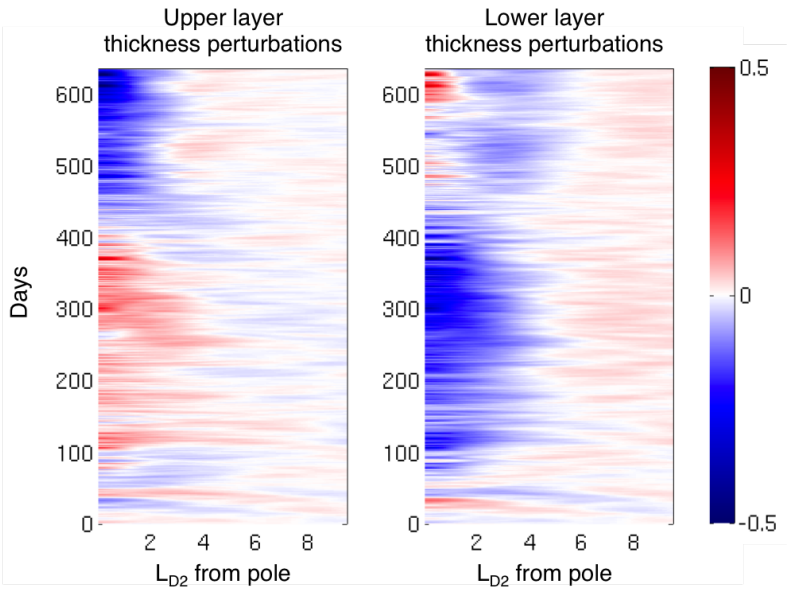

Figure 5-16: Upper and lower layer zonally averaged thickness perturbations over time. The instability can be seen in the sudden collapse of each layer's height perturbation, and subsequent reversal between the layers. Blue colors are anomalously thin regions and red colors are anomalously thick regions.

Simulation `id389` is an example of this vortex instability. Shortly after day 370, the available potential energy of the system abruptly loses over 30% of its magnitude. Concurrently, of course, the strong polar layer thickness deviations experience fast and transient adjustments to zero (Figure 5-16). Shortly after these abrupt changes, both layers briefly exhibit a negative thickness perturbation at the pole, before the upper layer suddenly becomes very thin over a broad polar area, while the lower layer also has a broad negative perturbation but a dramatic positive perturbation right on the pole. The potential vorticity responds, exhibiting a cyclone in the upper layer at the end of the simulation but a cyclonic annulus in the lower layer due to thermal wind balance.

This almost certainly involves diabatic effects due to radiative relaxation. Radiative cooling acts as a source of PV in the region of the thin cyclone, and is a stronger source for more intense vortices. At the high $\hat{E}_p$ end of the simulations, behavior is both highly forced and highly damped, and likely far from the parameter space of Jupiter and Saturn.

In polar coordinates this vortex instability difficult to detect. If H_1/H_2 is more than 50% or so from 1, the onset of this instability is faster due to the thin layer's intensified cyclone. For better or worse, the instability does not really affect the average total energy (though it can cause steep, temporary drops in APE), or the depth-integrated PV profile, or the mean winds. A statistical way to detect it is with the kurtosis of each layer. Kurtosis is able to indicate fast transitions between the presence of an intense vortex in just one layer, and then its presence abruptly only in the other layer, by exhibiting a large spike in magnitude in the vortex-containing layer before the instability sets in and moves the vortex to the other layer.

5.6 Conclusion

We demonstrate that, for constant $\tilde{\beta}$ and $\hat{E}_p$, model behavior is insensitive to individual parameter variation. $\hat{E}_p$ additionally provides a velocity scale that can be used faithfully with the anisotropy parameter α. We further show that the combination of $\hat{E}_p$ and $\tilde{\beta}$ can exhibit a broad range of fluid regimes, from low-energy jets, to multiple strong vortices, to a single dominant vortex.

An equivalent barotropic cyclone in a two layer model causes a negative deviation of the upper layer interface, and a positive deviation of the lower interface, resulting in a thin region of fluid relative to its surroundings. This is observed in the simulation behavior of polar vortices, and the upper layer depression is equivalent to a region of higher temperature. Saturn's polar vortices appear very hot immediately at the pole, and this is consistent with our results. The hot upper anomaly is accompanied by a cold anomaly at the base, where the quiescent deep fluid is upwelled under a strong lower layer cyclone. This provides a prediction, that the polar temperature is anomalously cold several scale heights below the tropopause; but this result is not unique to a two layer model or the particular character of the original storm forcing.

The question of the radiative overturning is complicated and deserves further attention. The implications of the circulation change depending on whether the cyclone is primarily in the upper or lower layer. A primitive equation model would be a good

tool to use for comparison, and storms could be parameterized by localized heating near the base of the troposphere.

In addition to the simulation results provided in this chapter, hundreds of simulations were run before the model reached its present form. Before the sponge layer was introduced, a β plane was developed that smoothly approached zero at the model bounds to avoid the discontinuity in the doubly period domain. A spherical variation was also employed briefly, before we settled on the formal polar beta plane. Simulations were run with various viscosities, time stepping schemes, storm seeding functions and resolutions. The qualitative result of energy and $\tilde{\beta}$ causing the greatest change in regimes has been consistent. The choice of a Cartesian grid is likely worth the troubles it causes during data analysis, but it would be interesting to run a lat-lon model on a pole with a filter, and see if similar results are achieved.

5.7 Appendix

ID	$\mathbf{Ro}_{conv}$	$\mathbf{Br}_2$	$\tilde{\tau}_{st}$	$\tilde{\tau}_{stp}$	A_r	a/L_{D2}	ρ_1/ρ_2	$\tilde{c}_1^2$	$\tilde{c}_2^2$	H_1/H_2	$\tilde{\tau}_{rad}$
id300	0.040	4.000	6	15	0.03	21	0.90	11	10	1.00	1000
id301	0.040	4.000	6	15	0.01	42	0.90	11	10	1.00	1000
id302	0.040	4.000	6	15	0.00	57	0.90	11	10	1.00	1000
id303	0.040	4.000	6	15	0.00	71	0.90	11	10	1.00	1000
id304	0.040	1.000	6	15	0.13	21	0.90	11	10	1.00	1000
id305	0.040	1.000	6	15	0.03	42	0.90	11	10	1.00	1000
id306	0.040	1.000	6	15	0.02	57	0.90	11	10	1.00	1000
id307	0.040	1.000	6	15	0.01	71	0.90	11	10	1.00	1000
id308	0.040	4.000	6	15	0.02	28	0.90	11	10	1.00	1000
id309	0.040	1.000	6	15	0.07	28	0.90	11	10	1.00	1000
id310	0.040	0.250	6	15	0.28	28	0.90	11	10	1.00	1000
id315	0.040	4.000	6	15	0.02	28	0.90	11	10	1.00	1000
id316	0.040	4.000	6	15	0.02	28	0.90	11	10	1.00	1000
id317	0.040	4.000	6	15	0.02	28	0.90	11	10	1.00	1000
id368	0.040	1.000	6	15	0.01	42	0.56	7	10	1.00	1000
id369	0.040	1.000	6	15	0.02	42	0.56	7	10	1.00	1000
id370	0.040	1.000	6	15	0.03	42	0.56	7	10	1.00	1000
id371	0.040	1.000	6	15	0.05	42	0.56	7	10	1.00	1000
id372	0.040	1.000	6	15	0.08	42	0.56	7	10	1.00	1000
id373	0.040	1.000	6	15	0.14	42	0.56	7	10	1.00	1000
id374	0.040	1.000	6	15	0.19	42	0.56	7	10	1.00	1000
id380	0.015	0.750	6	15	0.15	40	0.95	10	9	1.00	4000
id381	0.020	1.000	6	15	0.15	40	0.95	10	9	1.00	4000
id382	0.030	1.500	6	15	0.15	40	0.95	10	9	1.00	4000
id383	0.040	2.000	6	15	0.15	40	0.95	10	9	1.00	4000
id384	0.080	4.000	6	15	0.15	40	0.95	10	9	1.00	4000
id385	0.015	0.750	6	15	0.15	20	0.95	10	9	1.00	4000
id386	0.020	1.000	6	15	0.15	20	0.95	10	9	1.00	4000
id387	0.030	1.500	6	15	0.15	20	0.95	10	9	1.00	4000
id388	0.040	2.000	6	15	0.15	20	0.95	10	9	1.00	4000
id389	0.080	4.000	6	15	0.15	20	0.95	10	9	1.00	4000
id390	0.020	0.500	3	15	0.10	20	0.95	9	7	1.00	4000
id391	0.010	0.500	6	15	0.10	20	0.95	9	7	1.00	4000
id392	0.007	0.500	9	15	0.10	20	0.95	9	7	1.00	4000
id393	0.005	0.500	12	15	0.10	20	0.95	9	7	1.00	4000
id404	0.040	1.000	6	15	0.01	57	0.56	7	10	1.00	1000
id405	0.040	1.000	6	15	0.02	57	0.56	7	10	1.00	1000
id406	0.040	1.000	6	15	0.03	57	0.56	7	10	1.00	1000
id407	0.040	1.000	6	15	0.05	57	0.56	7	10	1.00	1000

Table 5.1: X2 experiments and their control parameters.

ID	$\mathbf{Ro}_{conv}$	$\mathbf{Br}_2$	$\tilde{\tau}_{st}$	$\tilde{\tau}_{stp}$	A_r	a/L_{D2}	ρ_1/ρ_2	$\tilde{c}_1^2$	$\tilde{c}_2^2$	H_1/H_2	$\tilde{\tau}_{rad}$
id408	0.040	1.000	6	15	0.08	57	0.56	7	10	1.00	1000
id409	0.040	1.000	6	15	0.14	57	0.56	7	10	1.00	1000
id410	0.040	1.000	6	15	0.19	57	0.56	7	10	1.00	1000
id411	0.040	1.000	6	15	0.01	71	0.56	7	10	1.00	1000
id412	0.040	1.000	6	15	0.02	71	0.56	7	10	1.00	1000
id413	0.040	1.000	6	15	0.03	71	0.56	7	10	1.00	1000
id414	0.040	1.000	6	15	0.05	71	0.56	7	10	1.00	1000
id415	0.040	1.000	6	15	0.08	71	0.56	7	10	1.00	1000
id416	0.040	1.000	6	15	0.14	71	0.56	7	10	1.00	1000
id417	0.040	1.000	6	15	0.19	71	0.56	7	10	1.00	1000
id418	0.080	0.500	3	15	0.10	20	0.95	9	7	1.00	4000
id419	0.040	0.500	6	15	0.10	20	0.95	9	7	1.00	4000
id420	0.027	0.500	9	15	0.10	20	0.95	9	7	1.00	4000
id421	0.020	0.500	12	15	0.10	20	0.95	9	7	1.00	4000
id422	0.040	0.500	3	15	0.10	20	0.95	9	7	1.00	4000
id423	0.020	0.500	6	15	0.10	20	0.95	9	7	1.00	4000
id424	0.013	0.500	9	15	0.10	20	0.95	9	7	1.00	4000
id425	0.010	0.500	12	15	0.10	20	0.95	9	7	1.00	4000
id426	0.015	0.750	6	15	0.15	30	0.95	10	9	1.00	4000
id427	0.020	1.000	6	15	0.15	30	0.95	10	9	1.00	4000
id428	0.030	1.500	6	15	0.15	30	0.95	10	9	1.00	4000
id429	0.040	2.000	6	15	0.15	30	0.95	10	9	1.00	4000
id430	0.080	4.000	6	15	0.15	30	0.95	10	9	1.00	4000
id431	0.004	0.750	6	15	0.15	30	0.95	10	9	1.00	4000
id432	0.005	1.000	6	15	0.15	30	0.95	10	9	1.00	4000
id435	0.020	1.000	6	15	0.15	30	0.95	10	9	1.00	4000
id440	0.020	1.000	6	15	0.10	30	0.95	6	4	1.00	4000
id441	0.020	1.000	6	15	0.10	30	0.95	10	8	1.00	4000
id442	0.020	1.000	6	15	0.10	30	0.95	14	12	1.00	4000
id443	0.020	1.000	6	15	0.10	30	0.95	10	4	1.00	4000
id444	0.020	1.000	6	15	0.10	30	0.95	8	4	1.00	4000
id445	0.020	1.000	6	15	0.10	30	0.95	14	4	1.00	4000
id446	0.020	1.000	6	15	0.10	30	0.95	18	4	1.00	4000
id447	0.004	0.188	6	15	0.15	40	0.95	10	9	1.00	4000
id448	0.005	0.250	6	15	0.15	40	0.95	10	9	1.00	4000
id449	0.007	0.375	6	15	0.15	40	0.95	10	9	1.00	4000
id450	0.010	0.500	6	15	0.15	40	0.95	10	9	1.00	4000
id451	0.005	1.000	6	15	0.15	30	0.95	10	9	1.00	4000
id452	0.007	1.500	6	15	0.15	30	0.95	10	9	1.00	4000

Table 5.2: X2 experiments continued.

ID	$\mathbf{Ro}_{conv}$	$\mathbf{Br}_2$	$\tilde{\tau}_{st}$	$\tilde{\tau}_{stp}$	A_r	a/L_{D2}	ρ_1/ρ_2	$\tilde{c}_1^2$	$\tilde{c}_2^2$	H_1/H_2	$\tilde{\tau}_{rad}$
id453	0.010	2.000	6	15	0.15	30	0.95	10	9	1.00	4000
id454	0.020	4.000	6	15	0.15	30	0.95	10	9	1.00	4000
id455	0.020	1.000	6	15	0.10	30	0.95	22	4	1.00	4000
id456	0.040	1.000	6	15	0.15	20	0.80	10	4	0.50	4000
id457	0.040	1.000	6	15	0.15	20	0.80	10	4	1.50	4000
id458	0.040	1.000	6	15	0.15	20	0.80	10	4	1.25	4000
id459	0.040	1.000	6	15	0.15	20	0.80	10	4	0.75	4000
id460	0.015	0.750	6	15	0.15	20	0.95	10	9	0.25	4000
id462	0.030	1.500	6	15	0.15	20	0.95	10	9	0.25	4000
id470	0.015	1.500	48	60	0.15	30	0.95	10	9	1.00	2000
id471	0.020	0.200	6	15	0.16	25	0.95	10	9	1.00	2000
id472	0.020	0.500	6	15	0.15	25	0.95	10	9	1.00	2000
id473	0.020	0.750	6	15	0.15	25	0.95	10	9	1.00	2000
id474	0.020	1.000	6	15	0.15	25	0.95	10	9	1.00	2000
id475	0.020	2.000	6	15	0.15	25	0.95	10	9	1.00	2000
id476	0.020	4.000	6	15	0.15	25	0.95	10	9	1.00	2000
id477	0.004	0.200	6	15	0.14	25	0.95	10	9	1.00	2000
id478	0.010	0.500	6	15	0.05	25	0.95	10	9	1.00	2000
id479	0.015	0.750	6	15	0.04	25	0.95	10	9	1.00	2000
id480	0.020	1.000	6	15	0.03	25	0.95	10	9	1.00	2000
id481	0.040	2.000	6	15	0.01	25	0.95	10	9	1.00	2000
id482	0.080	4.000	6	15	0.01	25	0.95	10	9	1.00	2000
id483	0.007	0.200	6	15	0.23	25	0.95	10	9	1.00	2000
id484	0.010	0.500	6	15	0.09	25	0.95	10	9	1.00	2000
id485	0.012	0.750	6	15	0.06	25	0.95	10	9	1.00	2000
id486	0.014	1.000	6	15	0.05	25	0.95	10	9	1.00	2000
id487	0.019	2.000	6	15	0.02	25	0.95	10	9	1.00	2000
id488	0.027	4.000	6	15	0.01	25	0.95	10	9	1.00	2000
id489	0.027	4.000	6	15	0.01	25	0.95	10	9	1.00	2000
id490	0.010	4.000	6	15	0.15	20	0.95	10	9	1.00	4000
id491	0.010	4.000	6	15	0.15	Inf	0.95	10	9	1.00	4000
id492	0.020	1.000	3	18	0.03	30	0.95	4	3	1.00	2000
id493	0.020	1.000	6	72	0.03	30	0.95	4	3	1.00	2000
id494	0.020	1.000	9	162	0.03	30	0.95	4	3	1.00	2000
id495	0.020	1.000	12	288	0.03	30	0.95	4	3	1.00	2000
id496	0.015	0.750	6	15	0.15	20	0.95	10	9	0.25	4000
id385	0.015	0.750	6	15	0.15	20	0.95	10	9	1.00	4000
id386	0.020	1.000	6	15	0.15	20	0.95	10	9	1.00	4000
id387	0.030	1.500	6	15	0.15	20	0.95	10	9	1.00	4000

Table 5.3: X2 experiments continued.

ID	$\mathbf{Ro}_{conv}$	$\mathbf{Br}_2$	$\tilde{\tau}_{st}$	$\tilde{\tau}_{stp}$	A_r	a/L_{D2}	ρ_1/ρ_2	$\tilde{c}_1^2$	$\tilde{c}_2^2$	H_1/H_2	$\tilde{\tau}_{rad}$
id388	0.040	2.000	6	15	0.15	20	0.95	10	9	1.00	4000
id389	0.080	4.000	6	15	0.15	20	0.95	10	9	1.00	4000
id502	0.020	1.000	6	15	0.10	30	0.95	18	4	1.00	4000
id503	0.020	1.000	6	12	0.03	30	0.95	4	3	1.00	200
id504	0.020	1.000	6	30	0.03	30	0.95	4	3	1.00	500
id505	0.020	1.000	6	60	0.03	30	0.95	4	3	1.00	1000
id506	0.020	1.000	6	240	0.03	30	0.95	4	3	1.00	4000
id393	0.005	0.500	12	15	0.10	20	0.95	9	7	1.00	4000
id392	0.007	0.500	9	15	0.10	20	0.95	9	7	1.00	4000
id391	0.010	0.500	6	15	0.10	20	0.95	9	7	1.00	4000
id390	0.020	0.500	3	15	0.10	20	0.95	9	7	1.00	4000
id511	0.040	1.000	6	12	0.03	30	0.95	4	3	1.00	200
id512	0.040	1.000	6	30	0.03	30	0.95	4	3	1.00	500
id513	0.040	1.000	6	60	0.03	30	0.95	4	3	1.00	1000
id514	0.040	1.000	6	240	0.03	30	0.95	4	3	1.00	4000
id515	0.005	1.000	6	15	0.30	50	0.95	10	9	1.00	2000
id516	0.005	1.000	6	15	0.15	50	0.95	10	9	1.00	2000
id517	0.020	1.000	6	15	0.40	50	0.95	10	9	1.00	2000
id518	0.005	1.000	20	20	0.25	50	0.95	10	9	1.00	2000
id519	0.001	1.000	6	15	0.47	50	0.95	4	3	1.00	2000
id520	0.001	1.000	6	15	0.47	50	0.95	4	3	1.00	2000
id521	0.005	1.000	6	15	0.47	50	0.95	4	3	1.00	2000
id522	0.010	1.000	6	15	0.47	50	0.95	4	3	1.00	2000
id523	0.020	1.000	6	15	0.47	50	0.95	4	3	1.00	2000
id525	0.001	1.000	6	15	0.47	40	0.95	4	3	1.00	2000
id526	0.001	1.000	6	15	0.47	40	0.95	4	3	1.00	2000
id527	0.005	1.000	6	15	0.47	40	0.95	4	3	1.00	2000
id528	0.010	1.000	6	15	0.47	40	0.95	4	3	1.00	2000
id529	0.020	1.000	6	15	0.47	40	0.95	4	3	1.00	2000
id531	0.001	1.000	6	15	0.47	30	0.95	4	3	1.00	2000
id532	0.001	1.000	6	15	0.47	30	0.95	4	3	1.00	2000
id533	0.005	1.000	6	15	0.47	30	0.95	4	3	1.00	2000
id534	0.010	1.000	6	15	0.47	30	0.95	4	3	1.00	2000
id535	0.020	1.000	6	15	0.47	30	0.95	4	3	1.00	2000
id537	0.001	1.000	6	15	0.47	20	0.95	4	3	1.00	2000
id538	0.001	1.000	6	15	0.47	20	0.95	4	3	1.00	2000
id539	0.005	1.000	6	15	0.47	20	0.95	4	3	1.00	2000
id540	0.010	1.000	6	15	0.47	20	0.95	4	3	1.00	2000
id541	0.020	1.000	6	15	0.47	20	0.95	4	3	1.00	2000

Table 5.4: X2 experiments continued.

ID	$\mathbf{Ro}_{conv}$	$\mathbf{Br}_2$	$\tilde{\tau}_{st}$	$\tilde{\tau}_{stp}$	A_r	a/L_{D2}	ρ_1/ρ_2	$\tilde{c}_1^2$	$\tilde{c}_2^2$	H_1/H_2	$\tilde{\tau}_{rad}$
id542	0.001	1.000	6	15	0.94	50	0.95	4	3	1.00	2000
id543	0.001	1.000	6	15	0.94	40	0.95	4	3	1.00	2000
id544	0.001	1.000	6	15	0.93	30	0.95	4	3	1.00	2000
id545	0.001	1.000	6	15	0.94	20	0.95	4	3	1.00	2000

Table 5.5: X2 experiments continued.

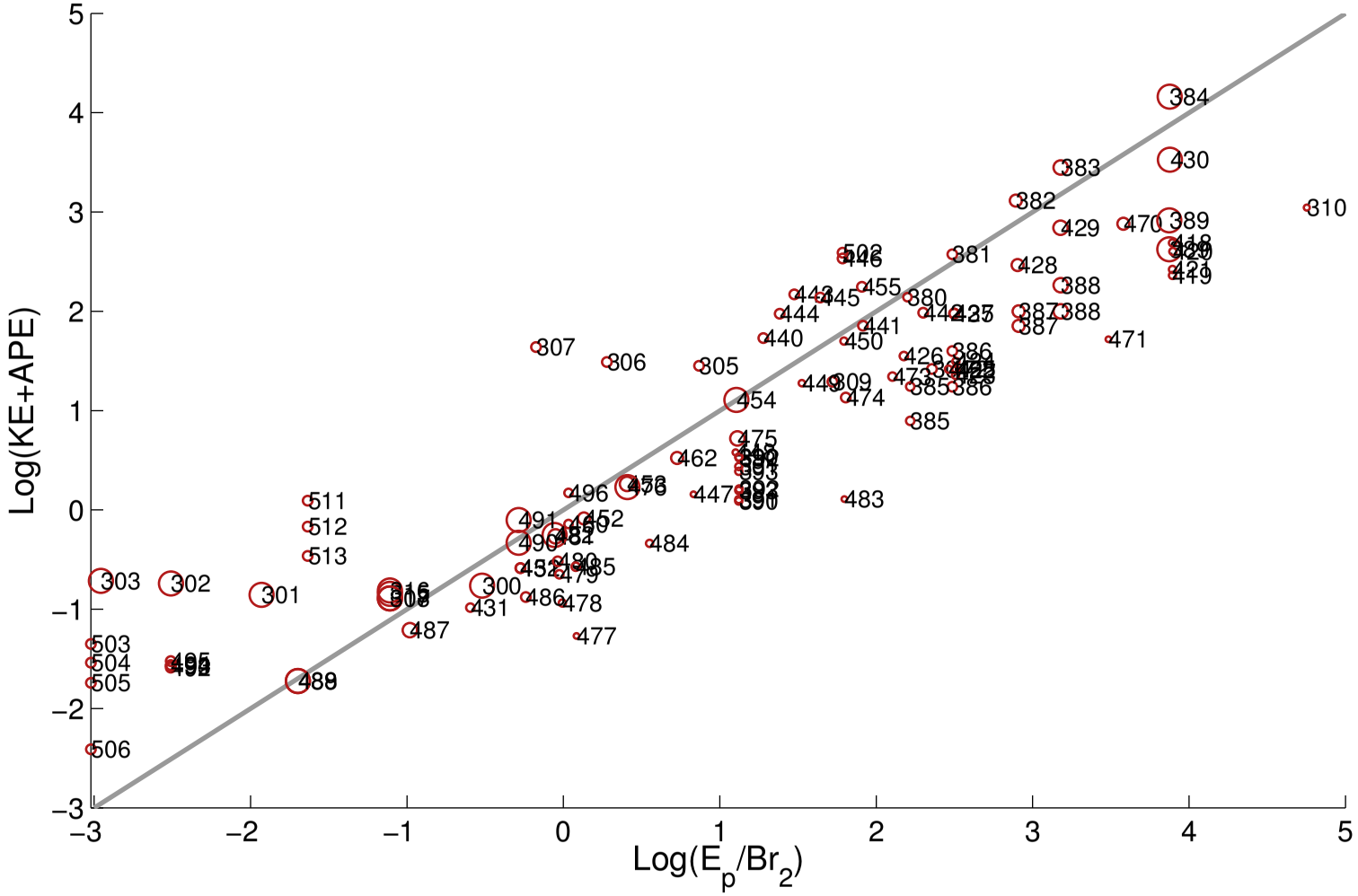

Figure 5-17: An expanded plot of $\log(\hat{E}_p)$ versus log(KE+APE), with simulation labels defined in above table for parameter comparisons. The grey line is a 1:1 ratio and the circle size denotes the Burger number.

Chapter 6

Comparison of results to the giant planets

A shallow water model is a highly idealized laboratory for real planetary atmospheres, with their complicated chemistry, infinite modal structure and strong overturning circulations. It gets a lot of use because it can be faithful to large-scale shallow flows, where most of the energy and motions of interest take place in the gravest few modes. In this chapter we redimensionalize some of the simulation output and compare the wind speeds and other scales with observations.

The largest relevant differences between Jupiter, which (likely) lacks a polar cyclone, and Saturn, are the deformation radius and water abundance. Both of these values favor a polar cyclone on Saturn within this simple framework. We will start with a summary of planetary parameters for the background state (such as gravity wave speeds), and then summarize storm-specific observations, before a thermodynamic scaling is used to redimensionalize the vertical and horizontal wind speeds.

6.1 Planetary background parameters

Deformation radii: Jupiter is larger and rotates faster than Saturn. Using the polar radii for each planet, a global $\beta = 2\Omega/a$ is approximately 5.3e-9 $s^{-1}km^{-1}$ for Jupiter and 6 $s^{-1}km^{-1}$ for Saturn, so they have very similar dimensional Coriolis

gradients. This is not very relevant to our nondimensional result: in the previous chapter a scaled Coriolis gradient, $\tilde{\beta}$, is shown to be a governing parameter, given a fixed total forcing and dissipation. It is a ratio of the squared second deformation radius to twice the squared planetary radius. The impact of the planetary rotation rate is absorbed in the deformation radius. Saturn's observed deformation radius is consistently estimated to be approximately twice that of Jupiter's, and Saturn's radius is only 80% that of Jupiter's. This makes Saturn's $\tilde{\beta}$ more than twice as large as Jupiter's.

Read et al. (2006) and Read et al. (2009) use Cassini and Voyager observations to create PV maps of Jupiter and Saturn, respectively. They estimate that Jupiter's L_D is between 1.7e3 to 2e3 km at midlatitudes, and in the polar region it decreases to 1e3 km or less. Saturn's deformation radius appears measurably larger; between 1e3 and 1.5e3 km in high latitudes.

Analytically, Achterberg and Ingersoll (1989) estimate a first baroclinic radius for Jupiter of just 750 km at the edge of the tropics, using their normal mode model constrained by Voyager data. A polar L_{D1} would be half that, for constant stratification. Gierasch and Conrath (1993) estimate a much larger L_{D1} of 4000 km for Jupiter. Allison (2000) formulates an analytical model for the shallow jovian flows, and defines a deformation radius as a function of meridionally varying static stability, itself a function of jet spacing. Allison's inferred subsequent deformation radii are 1400 km for Jupiter and 2870 km for Saturn.

Multiple authors have estimated the deformation radii of Jupiter and Saturn, and Saturn's L_D is always larger than Jupiter's, typically by a factor of two. In our nondimensional framework, this implies that Saturn has a larger $\tilde{\beta}$ than Jupiter. Without resorting to thermodynamics, our results suggest that this is sufficient to cause a polar cyclone on Saturn only. However, the thermodynamics that comprise $\hat{E}_p$ may also be different.

An important ambiguity that exists between our results and observations is the mode of the deformation radius. Our model scales the Coriolis gradient with a second baroclinic deformation radius. The model nondimensional layer gravity wave speeds

are not consistent across the simulations, and although their variation appears to make little change to the long-term behavior, this also prevents a consistent relationship between L_{D1} and L_{D2} (of course, the external one is always larger than the internal one). Whether the external $\tilde{\beta}$ provides as important a scale remains for near-future work, and below we use estimates from previous literature.

Gravity wave speeds: A gravity wave speed can be derived from observed and estimated deformation radii. Gravity waves were also observed directly during the Shoemaker-Levy 9 impact on Jupiter in 1993, and analysis suggests a gravity wave speed that is a function of the water abundance (Ingersoll et al. 1994, Ingersoll and Kanamori 1995).The observed fastest gravity wave speed post-impact is 450 m/s (Ingersoll and Kanamori, 1995). At the pole, this speed implies a first baroclinic deformation radius L_{D1} of about 1300 km, similar to the estimate of Allison (2000) and larger than the estimate of Read et al. (2006).

In this work, using jovian values for gravity and a weather layer scale height for layer thickness, the model's first baroclinic gravity wave speed is generally around 1500 m/s. The difference in speeds should not influence the dynamic behavior because storms are forced slowly enough to stay near geostrophic balance as they grow. Furthermore, we demonstrated in the previous chapter that changing the modal gravity wave ratio didn't significantly impact the total energy or behavior of simulations at equilibrium.

Water abundance: The water abundances of the giant planets are influential and loosely constrained. The water abundance sets the static stability of the lower troposphere; it provides a waveguide for gravity waves and scales the deformation radius (Achterberg and Ingersoll, 1989); and provides enough energy to towering cumulus plumes to cause dramatic lightning shows (Little et al., 1999). Moist (water) convection may also be the primary constituent that transfers energy from the top of the neutrally stable deep layer to the upper atmosphere (Stoker, 1986).

The Galileo probe found surprisingly low water mixing ratios down to 20 bars (Niemann et al., 1998), and local dynamics may be the cause (Showman and Ingersoll, 1998). Using Voyager radio occultation profiles, Allison (1990) estimates a water

abundance on Jupiter of 2-3 times solar, and Saturn likely has a water abundance of 5 times solar or more. These ratios have implications for the amount of latent heating available to the upper atmosphere via deep convection.

6.2 Storm properties

Large-area surveys of both Jupiter and Saturn provide detailed observations of vortex populations. The first comprehensive vortex study of Jupiter's vortices, with over 100 categorized 'spots', is undertaken by Low and Ingersoll (1986), using Voyager data. With higher resolution Cassini data, more than 500 'spots' on Jupiter are tracked and catalogued by Li et al. (2004), and among these likely convective storms are identified. A broad survey of Saturn's southern hemisphere by Vasavada et al. (2006), also with Cassini data, results in a catalog of scores of vortices.

On both Jupiter and Saturn, convective storms with radial extents of a few thousand km are observed to last from hours to days on both planets. Most vortices observed on Jupiter and Saturn are not obviously convective and persist much longer. The Galileo lightning measurements provide a proxy for identifying energetic *moist* convection, because water is necessary. The first Galileo survey of jovian lightning was undertaken by Little et al. (1999). They estimate that storms may be active for periods as short as an hour, but find some candidates that produced lightning for 31 days. They conclude that in shear regions, storms are likely to last no more than several days. The depths of some lightning may be as deep as 8 bars.

Li et al. (2004) find that potentially convective features on Jupiter have average lifetimes of 3.5 days, while non-convective features last an average of 16.8 days. The relationship of lifetime to number of spots is roughly an exponential decay, implying that fast convection is abundant (a major caveat is that the upper bound of lifetimes is 70 days of observations, so more long-lived vortices are not counted). All of the largest spots observed are anticyclonic, and the cyclonicity of the smaller spots is undetermined. They also find that the most transient spots (lifetimes around 4 days, likely convective) range in diameter from less than 1000 km to more than 6000 km.

The vortex survey of Vasavada et al. (2006) provides a histogram of vortex sizes (their Figure 6), showing that the number of vortices increases as their size shrinks, which suggests that the vortex population is underestimated at the smallest scales by the available resolution.

Dimensionalizing $\hat{E}_p$

We want to know the dimensional wind speeds of simulations in order to compare with observations. The shallow water energy equations, provided in Chapter 3, are nondimensionalized by $c_{e2}^2 H_i$ for the ith layer. The energy parameter $\hat{E}_p$ has a pressure term for each layer and a covariance term. If the first and third terms are multiplied by $c_{e2}^2 H_1$, and the second term is multiplied by $c_{e2}^2 H_2$, the energy parameter is dimensional. The entire set of storm forcing factors is still nondimensional and acts as an amplitude. Unfortunately, the real modal and layer wave speeds aren't known. The only estimate, discussed above from the SL9 impact, is likely of the first baroclinic mode (though without *in situ* observations this is not certain). However, thermodynamic arguments can allow comparison with some model storm parameters instead, providing us with a dimensional vertical velocity.

Rescaling to the planets

We closely follow S07 for a scaling comparison with expected values of Jupiter. An overturning time for the shallow water circulation can be solved and compared to the expected overturning time of Jupiter. The ratio of the total domain volume to total storm forcing volume averaged over some integer τ_{tsp} is:

$$\frac{(1 + H_1/H_2) a^2 \tau_{stp}}{\tau_{st} \# R_{st}^2 W_{st}/(f H_1)} \tag{6.1}$$

where the nondimensional Ro_{conv} has been expanded to show its scaling, and factors of f and L_{D2} have cancelled. Multiplying this ratio by f^{-1} redimensionalizes the expression by turning Ro_{conv} into a dimensional column stretching rate, and

provides an overturning time. For Jupiter, it should be approximately $pc_p\delta\theta/(g_{Jup}F)$, where $p = 10$ bars at the base of the troposphere, the static stability $\delta\theta$ is 10 K, the specific heat c_p is $1.3e4$ J/kg/K, and the heat flux F is 8 W/m^2. Jupiter's gravitational acceleration at the surface is 23 m/s^2. The timescale is approximately 7e8 seconds, or 54 Earth years.

The model ratio of storm period to storm lifetime has been observationally motivated from the beginning (for a small fractional storm area, here equivalent to # = 10); as is the squared ratio of the planetary radius to the storm size. The typical Burger number in our model is 1, the typical height ratio is 1, and a common number of storms in the domain at one time is 10. Letting those parameters remain simulation values for the moment, the remaining ratio is free to co-vary when set to the Jupiter timescale. Let $H_1/H_2 = 1$:

$$\tau_{Jup} = \frac{\tau_{stp}}{\tau_{st}} \frac{a^2}{\#R_{st}^2}(1 + H_1H_2)\frac{H_1}{W_{st}} \tag{6.2}$$

$$= (2)(2)\frac{(67\text{e}3)^2}{10(1\text{e}3)^2}\frac{H_1}{W_{st}} \tag{6.3}$$

$$\Rightarrow \frac{W_{st}}{H_1} = 1.7\text{e} - 6 \text{ seconds}^{-1} \tag{6.4}$$

Let the layer depth H_1 be the scale height of Jupiter, 27 km. This yields a storm vertical velocity W_{st} of about 5 cm/s. If this W_{st} is nondimensionalized again, but this time with jovian values of f and H_1, the nondimensional stretching term $\text{Ro}_{conv} = 0.02$, which is in the middle of the typical range for Ro_{conv} of [0.005 0.08]. We have neglected factors of π throughout the scalings, so this order of magnitude estimate is imprecise, but sufficient enough to demonstrate that we have been fairly modeling the Jupiter regime.

It is less straightforward to directly compare nondimensional horizontal velocities to dimensional, observed horizontal velocities, because the former are scaled by the second baroclinic gravity wave speed, which is not known. The layer thicknesses themselves are not rigorously defined or observed (here we settle for a scale height),

so the layer gravity wave speed is also unknown.

Fortunately, Achterberg and Ingersoll (1989) solved an eigenmode model for a range of second deformation radii specifically for Jupiter, 26 years ago. They find that the radii vary with the square root of the water abundance. The range of first deformation radii they offer is from 208-1550 km, which nicely bounds jovian observational estimates. The second radii range from 44-389 km. Read et al. (2006)'s estimate of Jupiter's L_{D1} suggests that the appropriate L_{D2} is either 228 or 154 km.

Multiplying $L_{D2} = 228$ km (for $L_{D1} = 985$ km) by the Coriolis acceleration yields a gravity wave speed of 80 m/s. Using the maximum model ratio of $\tilde{c}_2^2 = c_2^2/c_{e2}^2 = 9$, this yields an upper limit of the model lower layer gravity wave speed of 240 m/s. Likewise the upper layer speed's upper limit is 265 m/s. However, we can't just move over to Figure 5-9 and read off a fractional gravity wave speed, because the upper simulated bound of planet sizes is $a/L_{D2} = 70$; not 307 if scaled by the Achterberg and Ingersoll estimates. To do a direct comparison, a new suite of simulations must be run.

To redimensionalize our $\hat{E}_p$ and $\tilde{\beta}$ parameters, we need only know the second baroclinic deformation radius, the planet's rotation rate, and a layer depth. This is one more parameter than the Buckingham Pi theorem suggests because the shallow water equations uncouple the layer thicknesses from the horizontal lengths. A comprehensive redimensionalization across simulations remains to be done, taking care that planetary estimates are internally consistent.

6.3 Uranus and Neptune

Neptune and Uranus also have comparably large water abundances, perhaps as large as 20-30 solar. The Achterberg and Ingersoll (1989) finding that L_D scales with the root of the water abundance implies an L_D that is a substantial fraction of Neptune's radius. Polvani et al. (1990) use a dynamical model of Neptune's Great Dark Spot to estimate a lower bound for the deformation radius of 7000 km. Neptune's planetary radius is 24,600 km, which implies that Neptune has a very large $\tilde{\beta}$. Orton et al.

(2012) offer a much lower estimate of L_D, at 2000 km, which is still large enough to maintain Neptune's status of the highest $\tilde{\beta}$ with significant internal heating.

Given Neptune's significant energy imbalance - the highest in the solar system - and its very large deformation radius, perhaps our results suggest that Neptune should have the most intense polar vortex in the system. Recall that bright convective spots have rapidly appeared and evolved right at the pole (Luszcz-Cook et al. (2010)). However, Neptune's actual power is just a fifth that of Saturn (Pearl et al., 1990), which may be small enough to produce the transient polar accumulation we see on small planets but weakly forced planets. This is speculative because the extremely large $\tilde{\beta}$ case was not run.

6.4 Conclusion

To properly place the planets in our parameter space, we need to know the second internal deformation radius. Because of the difficulty in measuring or even defining internal deformation radii, the decision to scale the model by L_{D2} may deserve some rethinking. However if another scale is chosen, special care should be taken to consistently resolve storm-scale vorticity filaments - our original concern about resolution. The next step in redimensionalization would be to solve the Achterberg and Ingersoll (1989) normal mode model for Saturn and Neptune parameters, to yield deformation radii consistent with those employed here.

Apart from the troubles with unobserved deformation radii, we have demonstrated that the storm scalings are able to retrieve a very respectable estimate of Jupiter's vertical velocity: 4.6 cm/s. This is obviously on the very low end if one is interested in lightning, but many other storm parameters can co-vary at a fixed $\hat{E}_p$ to increase this velocity. Additionally, we are most interested in post-adjustment sizes, in part in order to reduce gravity wave radiation but also because beta drift happens more slowly than a storm lifetime. The convective updrafts themselves are not a focus of this study, nor is the shallow water system a good model for such intense vertical motion.

Chapter 7

Conclusion

Our understanding of the polar flows of gas giants, and indeed their comprehensive circulation, continues to improve as more sophisticated observations become available. It is not often one can find a simple and appealing problem for which ample theoretical basis exists, but has only newly been motivated. Planetary dynamics are so exciting because they provide laboratories we can't dream of. The discovery of the hot poles and attendant rapid jets on Saturn, as recently as 2004, demonstrates that the frontier is still close and accessible. Before these observations no one could guess that we would see such dramatic but stable behavior right on the pole.

7.1 Results

In this thesis we propose a theory for the formation and maintenance of polar cyclones on Saturn, motivated by recent Cassini observations and a host of prior theoretical and modeling works - both terrestrial and alien. Moist convection increasingly appears to play an important role in heat transfer from the planets' deep interior to space, and this should drive rapid knowledge transfer from the Earth science community to the planetary community.

This work parameterizes moist convection using appropriate horizontal and vertical scales. In Chapter 3 we build a 2 $\frac{1}{2}$ layer shallow water model designed to treat the pole agnostically, unlike many large GCMs. Still, the model geometry is very

simple and computationally cheap. We take advantage of the model's speed and vary an 11-dimensional parameter space. Immediately one is motivated to find a parameter that sums the effects of the others, and we follow Showman (2007) to derive a nondimensional energy parameter E_p.

The model behaves in a predictable way according to vortex-wave interaction theories, as explored in Chapter 4. In the unforced case, we can demonstrate that single-parameter variations behave according to existing theory. In concert, these parameters affect behavior in the same way as their variation affects E_p, which gives us confidence that E_p is a valuable scale. The other dimension that clearly affects the behavior of a single storm is the scaled Coriolis gradient, $\tilde{\beta}$, which affects both the nonlinear beta drift as well as the barotropization of the two layer fluid.

In Chapter 5, we modify E_p to account for significant kinetic energy contributions to total energy, and demonstrate that the collective behavior of our 11 control parameters can be duplicated by varying only two parameters, $\hat{E}_p$ and $\tilde{\beta}$. Our results suggest that the particular details of the forcing are not very important; rather its magnitude is the driver of flow. We show that the impact of changing storm size, intensity, duration or other parameters is roughly equivalent to changing $\hat{E}_p$. This has been observed in models for decades (e.g. Gierasch and Conrath 1993, Showman 2007, Zhang and Showman 2014). This aspect of our results is a corroboration of previous idealized studies. The unique aspect presented here is a focused look at specifically polar behavior in a baroclinic layer model. While many studies have examined the role of various nondimensional parameters on the presence, width and speed of the jets, very few works have optimized a polar environment for close examination. We find that the ratio of the planetary radius to the second baroclinic deformation radius, or equivalently the $\tilde{\beta}$ parameter, controls steady-state behavior through a background PV gradient that causes self-advection of cyclonic vorticity poleward. Large $\tilde{\beta}$ efficiently separates the vertical dipole created by the storm forcing, and provides a reservoir of enstrophy that promotes barotropization.

These forced-dissipative, steady state regimes vary tremendously (Figure 7-1). Among low $\hat{E}_p$ simulations, a small-$\tilde{\beta}$ planet will form very weak jets, while the

instantaneous flow field is dominated by weak baroclinic vortices (this is similar to the portion of Jupiter's South polar region that has been observed to date). Large-$\tilde{\beta}$ planets are still able to nonlinearly advect PV poleward, but this accumulation is weak and transient. Among medium and high $\hat{E}_p$ simulations, small-$\tilde{\beta}$ planets exhibit multiple cyclones that 'swim' around the polar region seemingly at random, as they interact more strongly with their neighboring vortices than with the weak planetary PV gradient. In contrast, a large-$\tilde{\beta}$ planet provides a strong planetary PV gradient, and early multiple cyclones merge near the pole into one dominant polar cyclone, similar to what is observed on Saturn. With increasing $\hat{E}_p$, a cyclone that remains within one or two L_{D2} from the pole starts to precess around it, with increasing distance from the pole.

While our most stable polar cyclones are similar to those of Saturn, there is one major difference. Saturn's polar cyclones have never been observed to move from their positions exactly over the poles. In the present simulations, no polar cyclone has been simulated that is as stationary, even though a time average shows a axisymmetric polar cyclone. The most stable cyclones still wobble over the pole, straying no farther than one L_{D2} radially.

Saturn and Jupiter are dynamically very similar, but their different planetary radii, gravities and water abundances may suffice to explain their different polar regimes. The difference in observed deformation radii of Saturn and Jupiter is consistent with our finding that a large-$\tilde{\beta}$ planet is more likely to maintain a polar cyclone than a small-$\tilde{\beta}$ planet.

These two dimensions, $\hat{E}_p$ and $\tilde{\beta}$, act effectively as the first two principal components of our multidimensional system. A full Principal Component Analysis cannot be done with the present set of simulations, because each control parameter was not varied enough times individually for sufficient statistics. However, no model behavior has been observed that cannot be replicated by changing $\hat{E}_p$ and/or $\tilde{\beta}$ (with the exception of H_1/H_2, which induces a comparatively more baroclinic polar cyclone due to a relatively thin layer).

We suggest that polar beta skirts maintain polar cyclones by providing additional

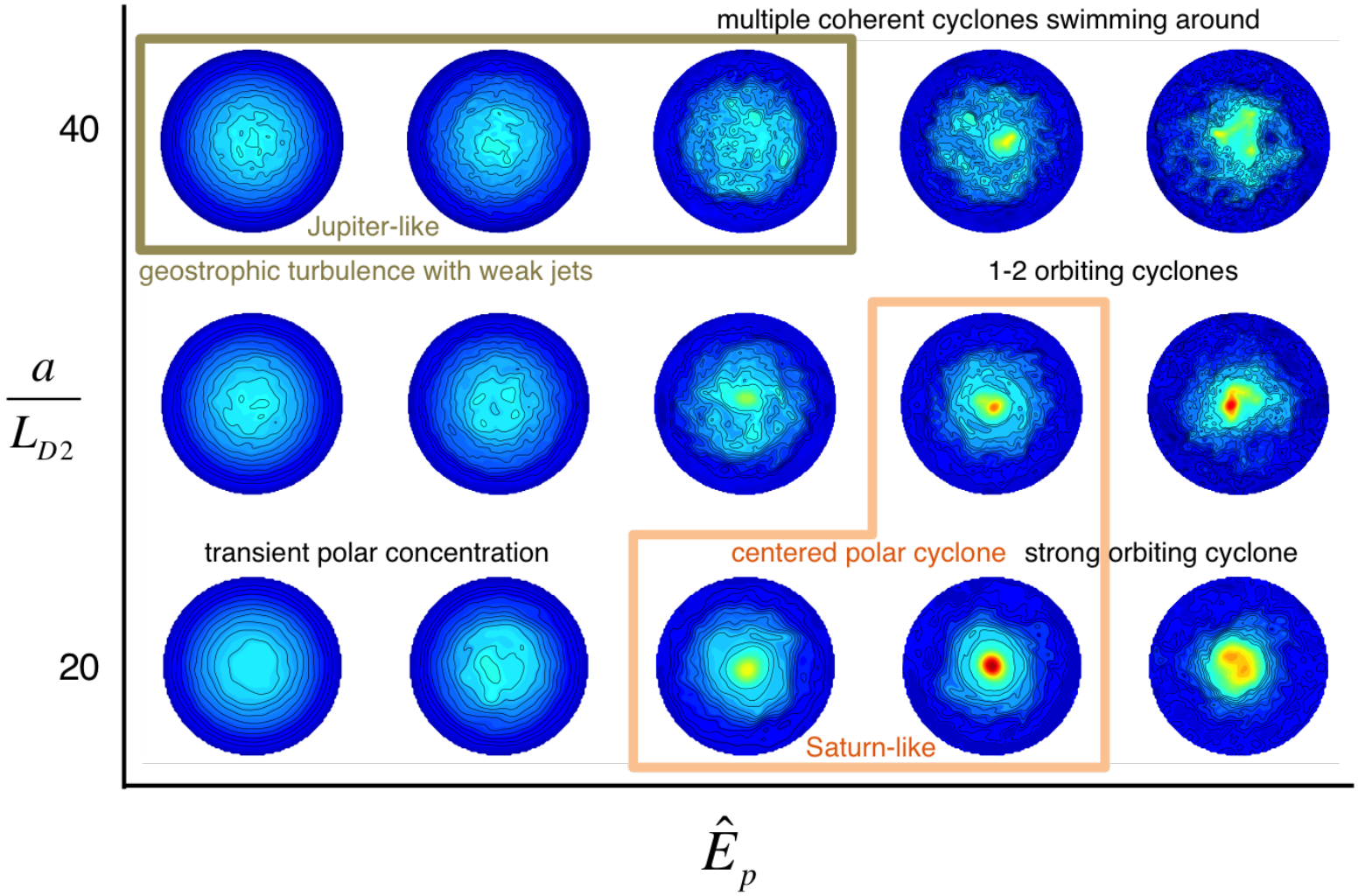

Figure 7-1: The 2D regimes for a set of simulations where only $\tilde{\beta}$ and Ro_{conv} (as a proxy for $\hat{E}_p$) are varied (see also Figures 5-7 and . Both colors and contours show the depth-integrated and time-averaged potential vorticity. The highest contour value is the the pole's background PV value, f_0/H, to illustrate regions where polar PV is higher than the background value. Regimes similar to Jupiter and Saturn are marked. The time averaging causes polar regions with a strong orbiting or randomly-moving vortex to appear smeared; the instantaneous fields would exhibit the most intense cyclones for the highest $\hat{E}_p$ simulations.

PV gradient for poleward propagation. The beta skirt is observed around the SPV and in simulations with polar vortices. However, the current model is probably too complicated for a clear understanding of this maintenance. It would be wise to use a one layer model in a similar regime space to explore sensitivity to such a beta skirt.

7.2 Discussion

Aside from scalings, the finding that a purely baroclinic 'convective' forcing can create a barotropic polar cyclone is new, though not surprising. It follows that such a cyclone would be relatively hot at upper levels and cold at depth. The modal gravity wave speed scaling presents a problem because the appropriate layer thicknesses are unknown. More importantly, the model was scaled by the second deformation radius for responsible consistency of resolution, and this makes it more difficult to compare results directly to the planets.

Another concern is that the most strongly forced models exhibit an instability in the neighborhood of a very strong cyclone. Both poles of Saturn appear to be depleted of phosphine gas, which varies as a function of both vertical mixing and photochemical destruction. This implies significant subsidence right at the poles (Fletcher et al., 2008), and so we should expect that a good model would permit this. The shallow water model is not that model, though it seemingly can parameterize an overturning circulation through radiative relaxation. However, understanding whether that proxy is physically relevant or unphysical imposed remains to be seen in this case.

The precession at large E_p, and the tendency for GCMs to only see cyclone precession and never stationary cyclones, recalls a paper by Chen and Cross (1996). They use the Euler equations in a circular domain to study inviscid vortex stability and long term behavior. Statistical mechanics has already been used to study Jupiter's Great Red Spot (e.g. Miller et al. 1992, Michel and Robert 1994, Bouchet and Dumont 2003). While statistical mechanics doesn't apply for nonconservative systems (like a planet), the upper atmospheres of the giant planets are not so damped that it has nothing to say. In fact, may statistical mechanics experiments can get realistic

jets and coherent vortices. With that in mind, we consider the results of Chen and Cross (1996). They find that as they increase the conserved angular momentum of a stable vortex in the center of the domain, it experiences a bifurcation and begins rotate around the origin, with increasing radius as the perturbation increases. Simple conservation of angular momentum might be sufficient to describe the radius of rotation - but that is certainly beyond the scope of a dissipative Cartesian model.

An exciting line of work is occurring parallel to classical understandings of planetary vertical structure. Leconte and Chabrier (2012) propose that the giant planets' interiors are doubly diffusive, which has major implications for convection. Briefly indulging in rampant speculation, this is interesting because doubly diffusive fluids are effectively layered. If Saturn's SPV is deep enough, and these layers are shallow enough, then perhaps the layers can effectively play the role of some thermal disequilibrium boundary, similar to the sea surface for terrestrial hurricanes (Emanuel, 1986). If it looks like a duck...

To close, a recognition of observational work is in order. We have been able to ask exciting, fundamental questions because we can see the dramatic results with our eyes. Questions about polar vortices and other phenomena would never be asked without the hard work of teams of thousands to imagine, build, launch and operate satellites, and then conduct painstaking data collection.

Bibliography

Achterberg, R. K. and A. P. Ingersoll, 1989: A normal-mode approach to Jovian atmospheric dynamics. *Journal of Atmospheric Sciences*, **46**, 2448–2462, doi:10.1175/1520-0469(1989)046¡2448:ANMATJ¿2.0.CO;2.

Achterberg, R. K. and A. P. Ingersoll, 1994: Numerical simulation of baroclinic jovian vortices. *Journal of Atmospheric Sciences*, **51 (4)**, 541–562.

Adem, J., 1956: A series solution for the barotropic vorticity equation and its application in the study of atmospheric vortices. *Tellus*, **8 (3)**, 364–372, doi:10.1111/j.2153-3490.1956.tb01234.x.

Allison, M., 1990: Planetary waves in jupiter's equatorial atmosphere. *Icarus*, **83 (2)**, 282–307, doi:http://dx.doi.org/10.1016/0019-1035(90)90069-L.

Allison, M., 2000: A similarity model for the windy jovian thermocline. *Planetary and Space Science*, **48 (7–8)**, 753–774, doi:http://dx.doi.org/10.1016/S0032-0633(00)00032-5.

Aurnou, J., M. Heimpel, and J. Wicht, 2007: The effects of vigorous mixing in a convective model of zonal flow on the ice giants. *Icarus*, **190 (1)**, 110–126, doi:http://dx.doi.org/10.1016/j.icarus.2007.02.024.

Bagenal, F., T. Dowling, and W. McKinnon, (Eds.) , 2005: *Jupiter: The planet, satellites and magnetosphere*, Vol. 40. Blackwell Publishing Ltd, 329–330 pp., doi:10.1111/j.1945-5100.2005.tb00384.x.

Baines, K. H., et al., 2009: Saturn's north polar cyclone and hexagon at depth revealed by cassini/vims. *Planetary and Space Science*, **57 (14–15)**, 1671–1681, doi:http://dx.doi.org/10.1016/j.pss.2009.06.026.

Banfield, D., P. J. Gierasch, M. Bell, E. Ustinov, A. P. Ingersoll, A. R. Vasavada, R. A. West, and M. J. S. Belton, 1998: Jupiter's cloud structure from galileo imaging data. *Icarus*, **135 (1)**, 230–250, doi:http://dx.doi.org/10.1006/icar.1998.5985.

Bouchet, F. and T. Dumont, 2003: Emergence of Jupiter's vortices and jets from random initial conditions. *eprint arXiv:cond-mat/0305206*, `cond-mat/0305206`.

Bridger, A. F. C. and D. E. Stevens, 1980: Long atmospheric waves and the polar-plane approximation to the earth's spherical geometry. *Journal of the Atmospheric Sciences*, **37 (3)**, 534–544.

Busse, F. H., 1976: A simple model of convection in the jovian atmosphere. *Icarus*, **29 (2)**, 255–260, doi:http://dx.doi.org/10.1016/0019-1035(76)90053-1.

Chan, J. C. L., 1982: On the Physical Processes Responsible for Tropical Cyclone Motion. Ph.D. thesis, Colorado State University.

Chan, J. C. L. and R. T. Williams, 1987: Analytical and numerical studies of the beta-effect in tropical cyclone motion. part i: Zero mean flow. *Journal of the Atmospheric Sciences*, **44 (9)**, 1257–1265, doi:10.1175/1520-0469(1987)044¡1257:AANSOT¿2.0.CO;2.

Charney, J. G., 1971: Geostrophic turbulence. *Journal of the Atmospheric Sciences*, **28 (6)**, 1087–1095, doi:10.1175/1520-0469(1971)028¡1087:GT¿2.0.CO;2.

Chen, P. and M. C. Cross, 1996: Mean field equilibria of single coherent vortices. *Phys. Rev. E*, **54**, 6356–6363, doi:10.1103/PhysRevE.54.6356.

Cho, J. Y.-K. and L. M. Polvani, 1996: The emergence of jets and vortices in freely evolving, shallow-water turbulence on a sphere. *Physics of Fluids*, **8**, 1531–1552, doi:10.1063/1.868929.

Choi, D. S. and A. P. Showman, 2011: Power spectral analysis of Jupiter's clouds and kinetic energy from Cassini. , **216**, 597–609, doi:10.1016/j.icarus.2011.10.001, 1301.6132.

Christensen, U. R., 2002: Zonal flow driven by strongly supercritical convection in rotating spherical shells. *Journal of Fluid Mechanics*, **470**, 115–133.

Conrath, B. J., P. J. Gierasch, and S. S. Leroy, 1990: Temperature and circulation in the stratosphere of the outer planets. *Icarus*, **83 (2)**, 255–281, doi:http://dx.doi.org/10.1016/0019-1035(90)90068-K.

del Genio, A. D., J. M. Barbara, J. Ferrier, A. P. Ingersoll, R. A. West, A. R. Vasavada, J. Spitale, and C. C. Porco, 2007: Saturn eddy momentum fluxes and convection: First estimates from cassini images. *Icarus*, **189 (2)**, 479 – 492, doi:http://dx.doi.org/10.1016/j.icarus.2007.02.013.

DiBattista, M. T. and A. J. Majda, 2000: An equilibrium statistical theory for large-scale features of open-ocean convection. *Journal of Physical Oceanography*, **30 (6)**, 1325–1353.

Dowling, T. E., 1993: A relationship between potential vorticity and zonal wind on jupiter. *Journal of the Atmospheric Sciences*, **50 (1)**, 14–22, doi:10.1175/1520-0469(1993)050¡0014:ARBPVA¿2.0.CO;2.

Dritschel, D. G. and M. E. Mcintyre, 2008: Multiple jets as pv staircases: The phillips effect and the resilience of eddy-transport barriers. *Journal of the Atmospheric Sciences*, **65 (3)**, 855–874.

Dyudina, U. A., et al., 2009: Saturn's south polar vortex compared to other large vortices in the solar system. *Icarus*, **202 (1)**, 240 – 248, doi: http://dx.doi.org/10.1016/j.icarus.2009.02.014.

Emanuel, K. A., 1986: An air-sea interaction theory for tropical cyclones. part i: Steady-state maintenance. *Journal of the Atmospheric Sciences*, **43 (6)**, 585–605, doi:10.1175/1520-0469(1986)043¡0585:AASITF¿2.0.CO;2.

Farrar, J., 1819: An account of the violent and destructive storm of the 23d of september, 1815. *The Quarterly Journal of Literature, Science and the Arts*, **7**, 102–106.

Fletcher, L., et al., 2008: Temperature and composition of saturn's polar hot spots and hexagon. *Science*, **319 (5859)**, 79–81.

Flierl, G., V. Larichev, J. McWilliams, and G. Reznik, 1980: The dynamics of baroclinic and barotropic solitary eddies. *Dynamics of Atmospheres and Oceans*, **5 (1)**, 1 – 41, doi:http://dx.doi.org/10.1016/0377-0265(80)90009-3.

Flierl, G. R., 1977: The application of linear quasigeostrophic dynamics to gulf stream rings. *Journal of Physical Oceanography*, **7 (3)**, 365–379, doi:10.1175/1520-0485(1977)007¡0365:TAOLQD¿2.0.CO;2.

Flierl, G. R., 1984: Rossby wave radiation from a strongly nonlinear warm eddy. *Journal of Physical Oceanography*, **14 (1)**, 47–58, doi:10.1175/1520-0485(1984)014¡0047:RWRFAS¿2.0.CO;2.

Flierl, G. R. and K. Haines, 1994: The decay of modons due to rossby wave radiation. *Physics of Fluids (1994-present)*, **6 (10)**, 3487–3497, doi: http://dx.doi.org/10.1063/1.868405.

Galperin, B., S. Sukoriansky, N. Dikovskaya, P. L. Read, Y. H. Yamazaki, and R. Wordsworth, 2006: Anisotropic turbulence and zonal jets in rotating flows with a beta-effect. *Nonlinear Processes in Geophysics*, **13 (1)**, 83–98, doi:10.5194/npg-13-83-2006.

Gierasch, P. J. and B. J. Conrath, 1993: Dynamics of the atmospheres of the outer planets: Post-voyager measurement objectives. *Journal of Geophysical Research: Planets*, **98 (E3)**, 5459–5469, doi:10.1029/92JE01897.

Gierasch, P. J., et al., 2000: Observation of moist convection in jupiter's atmosphere. *Nature*, **403 (6770)**, 628–630.

Gill, A., 1982: *Atmosphere-Ocean Dynamics*. No. v. 30 in Atmosphere-ocean Dynamics, Academic Press.

Hammel, H. and G. Lockwood, 2007: Long-term atmospheric variability on uranus and neptune. *Icarus*, **186 (1)**, 291 – 301, doi: http://dx.doi.org/10.1016/j.icarus.2006.08.027.

Hammel, H. B., M. L. Sitko, D. K. Lynch, G. S. Orton, R. W. Russell, T. R. Geballe, and I. de Pater, 2007: Distribution of Ethane and Methane Emission on Neptune. , **134**, 637–641, doi:10.1086/519382.

Hanel, R. A., B. J. Conrath, L. W. Herath, V. G. Kunde, and J. A. Pirraglia, 1981: Albedo, internal heat, and energy balance of jupiter: Preliminary results of the voyager infrared investigation. *Journal of Geophysical Research: Space Physics*, **86 (A10)**, 8705–8712, doi:10.1029/JA086iA10p08705.

Hanel, R. A., B. J. Conrath, V. G. Kunde, J. C. Pearl, and J. A. Pirraglia, 1983: Albedo, internal heat flux, and energy balance of saturn. *Icarus*, **53 (2)**, 262–285, doi:http://dx.doi.org/10.1016/0019-1035(83)90147-1.

Heimpel, M. and J. Aurnou, 2007: Turbulent convection in rapidly rotating spherical shells: A model for equatorial and high latitude jets on jupiter and saturn. *Icarus*, **187 (2)**, 540–557, doi:http://dx.doi.org/10.1016/j.icarus.2006.10.023.

Held, I. M. and A. Y. Hou, 1980: Nonlinear axially symmetric circulations in a nearly inviscid atmosphere. *Journal of the Atmospheric Sciences*, **37 (3)**, 515–533, doi: 10.1175/1520-0469(1980)037¡0515:NASCIA¿2.0.CO;2.

Hogg, N. G. and H. M. Stommel, 1985a: The heton, an elementary interaction between discrete baroclinic geostrophic vortices, and its implications concerning eddy heat-flow. *Proceedings of the Royal Society of London. A. Mathematical and Physical Sciences*, **397 (1812)**, 1–20, doi:10.1098/rspa.1985.0001, `http://rspa.royalsocietypublishing.org/content/397/1812/1.full.pdf+html`.

Hogg, N. G. and H. M. Stommel, 1985b: Hetonic explosions: The breakup and spread of warm pools as explained by baroclinic point vortices. *Journal of the Atmospheric Sciences*, **42 (14)**, 1465–1476.

Hunt, G. E., J.-P. Muller, and P. Gee, 1982: Convective growth rates of equatorial features in the jovian atmosphere. *Nature*, **295 (5849)**, 491–494.

Ingersoll, A. P., R. F. Beebe, S. A. Collins, G. E. Hunt, J. L. Mitchell, P. Muller, B. A. Smith, and R. J. Terrile, 1979: Zonal velocity and texture in the jovian atmosphere inferred from voyager images. *Nature*, **280 (5725)**, 773–775.

Ingersoll, A. P. and P. G. Cuong, 1981: Numerical model of long-lived jovian vortices. *Journal of the Atmospheric Sciences*, **38 (10)**, 2067–2076, doi:10.1175/1520-0469(1981)038¡2067:NMOLLJ¿2.0.CO;2.

Ingersoll, A. P., P. J. Gierasch, D. Banfield, A. R. Vasavada, and G. I. Team, 2000: Moist convection as an energy source for the large-scale motions in jupiter's atmosphere. *Nature*, **403 (6770)**, 630–632.

Ingersoll, A. P. and H. Kanamori, 1995: Waves from the collisions of comet shoemaker-levy 9 with jupiter. *Nature*, **374 (6524)**, 706–708.

Ingersoll, A. P., H. Kanamori, and T. E. Dowling, 1994: Atmospheric gravity waves from the impact of comet shoemaker-levy 9 with jupiter. *Geophysical Research Letters*, **21 (11)**, 1083–1086, doi:10.1029/94GL01057.

Kanamori, H., 1993: Excitation of jovian normal modes by an impact source. *Geophysical Research Letters*, **20 (24)**, 2921–2924, doi:10.1029/93GL03187.

Karkoschka, E., 2014: Uranus' Southern Circulation Revealed by Voyager-2 Images: Asymmetric, Unique, Unexpected. *AAS/Division for Planetary Sciences Meeting Abstracts*, AAS/Division for Planetary Sciences Meeting Abstracts, Vol. 46, 505.06.

Kaspi, Y. and G. R. Flierl, 2007: Formation of jets by baroclinic instability on gas planet atmospheres. *Journal of the Atmospheric Sciences*, **64 (9)**, 3177–3194, doi:10.1175/JAS4009.1.

Kaspi, Y., G. R. Flierl, and A. P. Showman, 2009: The deep wind structure of the giant planets: Results from an anelastic general circulation model. *Icarus*, **202 (2)**, 525–542, doi:http://dx.doi.org/10.1016/j.icarus.2009.03.026.

Larichev, V. and G. Reznik, 1976: 2-dimensional solitary rossby waves. *Doklady Akademii Nauk SSSR*, **231 (5)**, 1077–1079.

Leconte, J. and G. Chabrier, 2012: A new vision of giant planet interiors: Impact of double diffusive convection. , **540**, A20, doi:10.1051/0004-6361/201117595, 1201.4483.

Legg, S. and J. Marshall, 1993: A heton model of the spreading phase of open-ocean deep convection. *Journal of Physical Oceanography*, **23 (6)**, 1040–1056.

Li, L., A. P. Ingersoll, A. R. Vasavada, C. C. Porco, A. D. D. Genio, and S. P. Ewald, 2004: Life cycles of spots on jupiter from cassini images. *Icarus*, **172 (1)**, 9 – 23, doi:http://dx.doi.org/10.1016/j.icarus.2003.10.015, special Issue: Cassini-Huygens at Jupiter.

Lian, Y. and A. P. Showman, 2008: Deep jets on gas-giant planets. *Icarus*, **194 (2)**, 597 – 615, doi:http://dx.doi.org/10.1016/j.icarus.2007.10.014.

Lian, Y. and A. P. Showman, 2010: Generation of equatorial jets by large-scale latent heating on the giant planets. *Icarus*, **207 (1)**, 373–393, doi:http://dx.doi.org/10.1016/j.icarus.2009.10.006.

Lindzen, R. S., 1977: Some aspects of convection in meteorology. *Lecture Notes in Physics*.

Little, B., C. D. Anger, A. P. Ingersoll, A. R. Vasavada, D. A. Senske, H. Breneman, W. J. Borucki, and T. G. S. Team, 1999: Galileo images of lightning on jupiter. *Icarus*, **142 (2)**, 306 – 323, doi:http://dx.doi.org/10.1006/icar.1999.6195.

Liu, J. and T. Schneider, 2010: Mechanisms of jet formation on the giant planets. *Journal of the Atmospheric Sciences*, **67 (11)**, 3652–3672, doi:10.1175/2010JAS3492.1.

Liu, J. and T. Schneider, 2011: Convective generation of equatorial superrotation in planetary atmospheres. *Journal of the Atmospheric Sciences*, **68 (11)**, 2742–2756, doi:10.1175/JAS-D-10-05013.1.

Low, M.-M. M. and A. P. Ingersoll, 1986: Merging of vortices in the atmosphere of jupiter: An analysis of voyager images. *Icarus*, **65 (2Äì3)**, 353 – 369, doi:http://dx.doi.org/10.1016/0019-1035(86)90143-0.

Lunine, J. I., 1993: The atmospheres of uranus and neptune. *Annu. Rev. Astron. Astrophys.*, **31**, 217–263.

Luszcz-Cook, S. H., I. de Pater, M. Ádámkovics, and H. B. Hammel, 2010: Seeing double at neptune's south pole. *Icarus*, **208 (2)**, 938–944, doi:http://dx.doi.org/10.1016/j.icarus.2010.03.007.

Marcus, P. S., 1990: Vortex dynamics in a shearing zonal flow. *Journal of Fluid Mechanics*, **215**, 393–430, doi:10.1017/S0022112090002695.

Marston, J. B., W. Qi, and S. M. Tobias, 2014: Direct Statistical Simulation of a Jet. *ArXiv e-prints*, `1412.0381`.

McDonald, N. R., 1998: The decay of cyclonic eddies by rossby wave radiation. *Journal of Fluid Mechanics*, **361**, 237–252, doi:10.1017/S0022112098008696.

McWilliams, J. C., 1980: An application of equivalent modons to atmospheric blocking. *Dynamics of Atmospheres and Oceans*, **5 (1)**, 43 – 66, doi:http://dx.doi.org/10.1016/0377-0265(80)90010-X.

Michel, J. and R. Robert, 1994: Statistical mechanical theory of the great red spot of jupiter. *Journal of Statistical Physics*, **77 (3-4)**, 645–666, doi:10.1007/BF02179454.

Miller, J., P. B. Weichman, and M. C. Cross, 1992: Statistical mechanics, euler's equation, and jupiter's red spot. *Phys. Rev. A*, **45**, 2328–2359, doi:10.1103/PhysRevA.45.2328.

Mitchell, J. L. and G. K. Vallis, 2010: The transition to superrotation in terrestrial atmospheres. *Journal of Geophysical Research: Planets*, **115 (E12)**, n/a–n/a, doi:10.1029/2010JE003587.

Montgomery, M. T., M. E. Nicholls, T. A. Cram, and A. B. Saunders, 2006: A vortical hot tower route to tropical cyclogenesis. *Journal of the Atmospheric Sciences*, **63 (1)**, 355–386, doi:10.1175/JAS3604.1.

Mousis, O., U. Marboeuf, J. I. Lunine, Y. Alibert, L. N. Fletcher, G. S. Orton, F. Pauzat, and Y. Ellinger, 2009: Determination of the minimum masses of heavy elements in the envelopes of jupiter and saturn. *The Astrophysical Journal*, **696 (2)**, 1348.

Niemann, H. B., et al., 1998: The composition of the jovian atmosphere as determined by the galileo probe mass spectrometer. *Journal of Geophysical Research: Planets*, **103 (E10)**, 22 831–22 845, doi:10.1029/98JE01050.

Nof, D., 1990: Modons and monopoles on a gamma-plane. *Geophysical and Astrophysical Fluid Dynamics*, **52**, 71–87, doi:10.1080/03091929008219840.

Nolan, D. S. and L. D. Grasso, 2003: Nonhydrostatic, three-dimensional perturbations to balanced, hurricane-like vortices. part ii: Symmetric response and nonlinear simulations. *Journal of the Atmospheric Sciences*, **60 (22)**, 2717–2745, doi:10.1175/1520-0469(2003)060¡2717:NTPTBH¿2.0.CO;2.

Nycander, J., 1994: Steady vortices in plasmas and geophysical flows. *Chaos: An Interdisciplinary Journal of Nonlinear Science*, **4 (2)**, 253–267, doi:http://dx.doi.org/10.1063/1.166006.

Okuno, A. and A. Masuda, 2003: Effect of horizontal divergence on the geostrophic turbulence on a beta-plane: Suppression of the rhines effect. *Physics of Fluids (1994-present)*, **15 (1)**, 56–65, doi:http://dx.doi.org/10.1063/1.1524188.

Orton, G. S. and P. A. Yanamandra-Fisher, 2005: Saturn's temperature field from high-resolution middle-infrared imaging. *Science*, **307 (5710)**, 696–698, doi:10.1126/science.1105730, `http://www.sciencemag.org/content/307/5710/696.full.pdf`.

Orton, G. S., et al., 2012: Recovery and characterization of neptune's near-polar stratospheric hot spot. *Planetary and Space Science*, **61 (1)**, 161 – 167, doi:http://dx.doi.org/10.1016/j.pss.2011.06.013, surfaces, atmospheres and magnetospheres of the outer planets and their satellites and ring systems: Part {VII}.

Panetta, R. L., 1993: Zonal jets in wide baroclinically unstable regions: Persistence and scale selection. *Journal of the Atmospheric Sciences*, **50 (14)**, 2073–2106, doi:10.1175/1520-0469(1993)050¡2073:ZJIWBU¿2.0.CO;2.

Pearl, J. C. and B. J. Conrath, 1991: The albedo, effective temperature, and energy balance of neptune, as determined from voyager data. *Journal of Geophysical Research: Planets*, **96**.

Pearl, J. C., B. J. Conrath, R. A. Hanel, J. A. Pirraglia, and A. Coustenis, 1990: The albedo, effective temperature, and energy balance of uranus, as determined from voyager iris data. *Icarus*, **84 (1)**, 12–28, doi:http://dx.doi.org/10.1016/0019-1035(90)90155-3.

Penny, A. B., A. P. Showman, and D. S. Choi, 2010: Suppression of the rhines effect and the location of vortices on saturn. *Journal of Geophysical Research: Planets*, **115 (E2)**, n/a–n/a, doi:10.1029/2009JE003384.

Petigura, E. A., A. W. Howard, and G. W. Marcy, 2013: Prevalence of earth-size planets orbiting sun-like stars. *Proceedings of the National Academy of Sciences*, **110 (48)**, 19 273–19 278, doi:10.1073/pnas.1319909110, http://www.pnas.org/content/110/48/19273.full.pdf+html.

Polvani, L. M., J. C. McWilliams, M. A. Spall, and R. Ford, 1994: The coherent structures of shallow-water turbulence: Deformation radius effects, cyclone/anticyclone asymmetry and gravity-wave generation. *Chaos: An Interdisciplinary Journal of Nonlinear Science*, **4 (2)**, 177–186, doi:http://dx.doi.org/10.1063/1.166002.

Polvani, L. M., J. Wisdom, E. DeJong, and A. P. Ingersoll, 1990: Simple dynamical models of neptune's great dark spot. *Science*, **249 (4975)**, 1393–1398, doi:10.1126/science.249.4975.1393, http://www.sciencemag.org/content/249/4975/1393.full.pdf.

Porco, C. C., et al., 2003: Cassini imaging of jupiter's atmosphere, satellites, and rings. *Science*, **299 (5612)**, 1541–1547, doi:10.1126/science.1079462, http://www.sciencemag.org/content/299/5612/1541.full.pdf.

Read, P., B. Conrath, L. Fletcher, P. Gierasch, A. Simon-Miller, and L. Zuchowski, 2009: Mapping potential vorticity dynamics on saturn: Zonal mean circulation from cassini and voyager data. *Planetary and Space Science*, **57 (14Äì15)**, 1682 – 1698, doi:http://dx.doi.org/10.1016/j.pss.2009.03.004.

Read, P. L., P. J. Gierasch, B. J. Conrath, A. Simon-Miller, T. Fouchet, and Y. H. Yamazaki, 2006: Mapping potential-vorticity dynamics on jupiter. i: Zonal-mean circulation from cassini and voyager 1 data. *Quarterly Journal of the Royal Meteorological Society*, **132 (618)**, 1577–1603, doi:10.1256/qj.05.34.

Read, P. L. and R. Hide, 1983: Long-lived eddies in the laboratory and in the atmospheres of jupiter and saturn. *Nature*, **302 (5904)**, 126–129.

Rhines, P. B., 1975: Waves and turbulence on a beta-plane. *Journal of Fluid Mechanics*, **69**, 417–443, doi:10.1017/S0022112075001504.

Sánchez-Lavega, A., R. Hueso, S. Pérez-Hoyos, and J. F. Rojas, 2006: A strong vortex in saturn's south pole. *Icarus*, **184 (2)**, 524–531.

Schneider, T. and J. Liu, 2009: Formation of jets and equatorial superrotation on jupiter. *Journal of the Atmospheric Sciences*, **66 (3)**, 579–601, doi:10.1175/2008JAS2798.1.

Scott, R., 2011: Polar accumulation of cyclonic vorticity. *Geophysical amp; Astrophysical Fluid Dynamics*, **105 (4-5)**, 409–420, doi:10.1080/03091929.2010.509927, http://dx.doi.org/10.1080/03091929.2010.509927.

Scott, R. and L. M. Polvani, 2008: Equatorial superrotation in shallow atmospheres. *Geophysical Research Letters*, **35 (24)**.

Scott, R. K. and L. M. Polvani, 2007: Forced-dissipative shallow-water turbulence on the sphere and the atmospheric circulation of the giant planets. *Journal of the Atmospheric Sciences*, **64 (9)**, 3158–3176, doi:10.1175/JAS4003.1.

Showman, A. P., 2007: Numerical simulations of forced shallow-water turbulence: Effects of moist convection on the large-scale circulation of jupiter and saturn. *Journal of the Atmospheric Sciences*, **64 (9)**, 3132–3157, doi:10.1175/JAS4007.1.

Showman, A. P., P. J. Gierasch, and Y. Lian, 2006: Deep zonal winds can result from shallow driving in a giant-planet atmosphere. *Icarus*, **182 (2)**, 513–526, doi: http://dx.doi.org/10.1016/j.icarus.2006.01.019.

Showman, A. P. and A. P. Ingersoll, 1998: Interpretation of galileo probe data and implications for jupiter's dry downdrafts. *Icarus*, **132 (2)**, 205 – 220, doi: http://dx.doi.org/10.1006/icar.1998.5898.

Simonnet, E., M. Ghil, K. Ide, R. Temam, and S. Wang, 2003: Low-frequency variability in shallow-water models of the wind-driven ocean circulation. part i: Steady-state solution*. *Journal of Physical Oceanography*, **33 (4)**, 712–728, doi: 10.1175/1520-0485(2003)33¡712:LVISMO¿2.0.CO;2.

Smith, K. S., 2004: A local model for planetary atmospheres forced by small-scale convection. *Journal of the Atmospheric Sciences*, **61 (12)**, 1420–1433, doi: 10.1175/1520-0469(2004)061¡1420:ALMFPA¿2.0.CO;2.

Smith, K. S. and G. K. Vallis, 2001: The scales and equilibration of midocean eddies: Freely evolving flow. *Journal of Physical Oceanography*, **31 (2)**, 554–571, doi:10.1175/1520-0485(2001)031¡0554:TSAEOM¿2.0.CO;2.

Smith, S. G. L., 1997: The motion of a non-isolated vortex on the beta-plane. *Journal of Fluid Mechanics*, **346**, 149–179.

Sokolovskiy, M. and J. Verron, 2013: *Dynamics of Vortex Structures in a Stratified Rotating Fluid*. Atmospheric and Oceanographic Sciences Library, Springer.

Stern, M. E., 1975: Minimal properties of planetary eddies. *Journal of Marine Research*, **33**, 1–13.

Stoker, C. R., 1986: Moist convection: A mechanism for producing the vertical structure of the jovian equatorial plumes. *Icarus*, **67 (1)**, 106–125, doi: http://dx.doi.org/10.1016/0019-1035(86)90179-X.

Stone, P. H., 1972: A simplified radiative-dynamical model for the static stability of rotating atmospheres. *Journal of the Atmospheric Sciences*, **29 (3)**, 405–418, doi:10.1175/1520-0469(1972)029¡0405:ASRDMF¿2.0.CO;2.

Sugiyama, K., K. Nakajima, M. Odaka, K. Kuramoto, and Y. Y. Hayashi, 2014: Numerical simulations of jupiter's moist convection layer: Structure and dynamics in statistically steady states. *Icarus*, **229 (0)**, 71–91, doi: http://dx.doi.org/10.1016/j.icarus.2013.10.016.

Sutyrin, G. G., J. S. Hesthaven, J. P. Lynov, and J. J. Rasmussen, 1994: Dynamical properties of vortical structures on the beta-plane. *Journal of Fluid Mechanics*, **268**, 103–131, doi:10.1017/S002211209400128X.

Terwey, W. D. and M. T. Montgomery, 2008: Secondary eyewall formation in two idealized, full-physics modeled hurricanes. *Journal of Geophysical Research: Atmospheres*, **113 (D12)**, n/a–n/a, doi:10.1029/2007JD008897.

Theiss, J., 2004: Equatorward energy cascade, critical latitude, and the predominance of cyclonic vortices in geostrophic turbulence. *Journal of Physical Oceanography*, **34 (7)**, 1663–1678, doi:10.1175/1520-0485(2004)034¡1663:EECCLA¿2.0.CO;2.

Vallis, G. K., 2006: *Atmospheric and Oceanic Fluid Dynamics*. Cambridge University Press, Cambridge, U.K., 745 pp.

Vasavada, A. R., S. M. Hrst, M. R. Kennedy, A. P. Ingersoll, C. C. Porco, A. D. Del Genio, and R. A. West, 2006: Cassini imaging of saturn: Southern hemisphere winds and vortices. *Journal of Geophysical Research: Planets*, **111 (E5)**, n/a–n/a, doi:10.1029/2005JE002563.

Vasavada, A. R. and A. P. Showman, 2005: Jovian atmospheric dynamics: an update after galileo and cassini. *Reports on Progress in Physics*, **68 (8)**, 1935.

Vasavada, A. R., et al., 1998: Galileo imaging of jupiter's atmosphere: The great red spot, equatorial region, and white ovals. *Icarus*, **135 (1)**, 265–275, doi: http://dx.doi.org/10.1006/icar.1998.5984.

Venaille, A., G. K. Vallis, and S. M. Griffies, 2012: The catalytic role of the beta effect in barotropization processes. *Journal of Fluid Mechanics*, **709**, 490–515, doi: 10.1017/jfm.2012.344, 1201.0657.

Verkley, W. T. M., 1984: The construction of barotropic modons on a sphere. *Journal of the Atmospheric Sciences*, **41 (16)**, 2492–2504, doi:10.1175/1520-0469(1984)041¡2492:TCOBMO¿2.0.CO;2.

Wang, Y. and G. J. Holland, 1996: The beta drift of baroclinic vortices. part i: Adiabatic vortices. *Journal of the Atmospheric Sciences*, **53 (3)**, 411–427, doi: 10.1175/1520-0469(1996)053¡0411:TBDOBV¿2.0.CO;2.

Wang, Y. and G. J. Holland, 1996: The Beta Drift of Baroclinic Vortices. Part II: Diabatic Vortices. *Journal of Atmospheric Sciences*, **53**, 3737–3756, doi:10.1175/1520-0469(1996)053¡3737:TBDOBV¿2.0.CO;2.

Warneford, E. S. and P. J. Dellar, 2014: Thermal shallow water models of geostrophic turbulence in jovian atmospheres. *Physics of Fluids (1994-present)*, **26 (1)**, 016603, doi:http://dx.doi.org/10.1063/1.4861123.

Weidenschilling, S. J. and J. S. Lewis, 1973: Atmospheric and cloud structures of the jovian planets. *Icarus*, **20 (4)**, 465–476, doi:http://dx.doi.org/10.1016/0019-1035(73)90019-5.

Williams, G. P., 1975: Jupiter's atmospheric circulation. *Nature*, **257 (5529)**, 778–778.

Williams, G. P., 1978: Planetary circulations: 1. barotropic representation of jovian and terrestrial turbulence. *Journal of the Atmospheric Sciences*, **35 (8)**, 1399–1426, doi:10.1175/1520-0469(1978)035¡1399:PCBROJ¿2.0.CO;2.

Williams, G. P. and J. B. Robinson, 1973: Dynamics of a convectively unstable atmosphere: Jupiter? *Journal of the Atmospheric Sciences*, **30 (4)**, 684–717, doi:10.1175/1520-0469(1973)030¡0684:DOACUA¿2.0.CO;2.

Zhang, X. and A. P. Showman, 2014: Atmospheric Circulation of Brown Dwarfs: Jets, Vortices, and Time Variability. , **788**, L6, doi:10.1088/2041-8205/788/1/L6, 1403.2143.